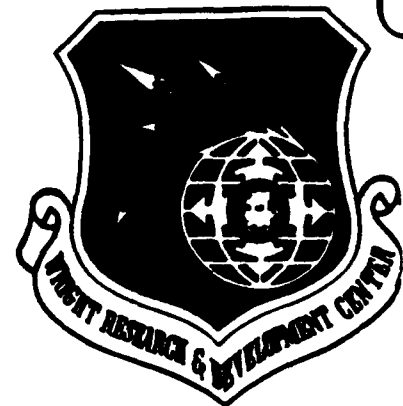


DUPLICATE COPY

2

AD-A222 390



WRDC-TR-90-3002

AN ADAPTIVE GRID ALGORITHM FOR NONEQUILIBRIUM HYPERSONIC FLOWS

Michael J. Aftosmis
Judson R. Baron

Massachusetts Institute of Technology
Department of Aeronautics and Astronautics
Cambridge, MA 02139

April 1990

Final Report for Period September 1987 - August 1989

Approved for public release; distribution is unlimited

DTIC
ELECTE
MAY 23 1990
S B D

FLIGHT DYNAMICS LABORATORY
WRIGHT RESEARCH AND DEVELOPMENT CENTER
AIR FORCE SYSTEMS COMMAND
WRIGHT-PATTERSON AIR FORCE BASE, OHIO 45433-6553


NOTICE

When Government drawings, specifications, or other data are used for any purpose other than in connection with a definitely Government-related procurement, the United States Government incurs no responsibility or any obligation whatsoever. The fact that the Government may have formulated or in any way supplied the said drawings, specifications, or other data, is not to be regarded by implication, or otherwise in any manner construed, as licensing the holder, or any other person or corporation; or as conveying any rights or permission to manufacture, use, or sell any patented invention that may in any way be related thereto.

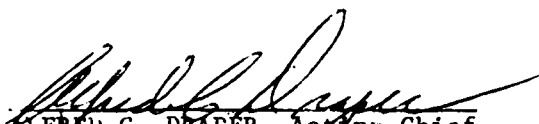
This technical report has been reviewed and is approved for publication.


KERVYN D. MACH

Aerospace Engineer
Computational Aerodynamics Group
Aerodynamics and Airframe Branch


DENNIS SEDLOCK, Chief
Aerodynamics and Airframe Branch
Aeromechanics Division

FOR THE COMMANDER


ALFRED C. DRAPER, Acting Chief
Aeromechanics Division
Flight Dynamics Laboratory

If your address has changed, if you wish to be removed from our mailing list, or if the addressee is no longer employed by your organization, please notify WRDC/FIMM, WPAFB OH 45433-6553 to help us maintain a current mailing list.

Copies of this report should not be returned unless it is required by security considerations, contractual obligations, or notice on a specific document.

UNCLASSIFIED

SECURITY CLASSIFICATION OF THIS PAGE

REPORT DOCUMENTATION PAGE				Form Approved OMB No. 0704-0188	
1a. REPORT SECURITY CLASSIFICATION Unclassified			1b. RESTRICTIVE MARKINGS		
2a. SECURITY CLASSIFICATION AUTHORITY			3. DISTRIBUTION/AVAILABILITY OF REPORT Approved for public release; distribution is unlimited		
2b. DECLASSIFICATION/DOWNGRADING SCHEDULE					
4. PERFORMING ORGANIZATION REPORT NUMBER(S) CFD-TR-89-8			5. MONITORING ORGANIZATION REPORT NUMBER(S) WRDC-TR-90-3002		
6a. NAME OF PERFORMING ORGANIZATION Dept. of Aero. and Astro. Massachusetts Institute of Tech.		6b. OFFICE SYMBOL (if applicable)	7a. NAME OF MONITORING ORGANIZATION Flight Dynamics Laboratory (WRDC/FIMM) Wright Research and Development Center		
6c. ADDRESS (City, State, and ZIP Code) Dept. of Aero. and Astro. M.I.T. Cambridge, MA 02139		7b. ADDRESS (City, State, and ZIP Code) Wright-Patterson AFB OH 45433-6553			
8a. NAME OF FUNDING/SPONSORING ORGANIZATION		8b. OFFICE SYMBOL (if applicable)	9. PROCUREMENT INSTRUMENT IDENTIFICATION NUMBER F33615-87-C-3004		
8c. ADDRESS (City, State, and ZIP Code)		10. SOURCE OF FUNDING NUMBERS			
		PROGRAM ELEMENT NO.	PROJECT NO.	TASK NO.	WORK UNIT ACCESSION NO.
		61102F	2307	N6	13
11. TITLE (Include Security Classification) AN ADAPTIVE GRID ALGORITHM FOR NONEQUILIBRIUM HYPERSONIC FLOWS					
12. PERSONAL AUTHOR(S) Michael J. Aftosmis, Judson R. Baron					
13a. TYPE OF REPORT Final		13b. TIME COVERED FROM Sept 87 TO Aug 89		14. DATE OF REPORT (Year, Month, Day) 1990, April	
				15. PAGE COUNT 156	
16. SUPPLEMENTARY NOTATION					
17. COSATI CODES			18. SUBJECT TERMS (Continue on reverse if necessary and identify by block number)		
FIELD	GROUP	SUB-GROUP			
01	01		Computational Fluid Dynamics; Nonequilibrium Flow; Hypersonic; Adaptive Grid		
01	02				
19. ABSTRACT (Continue on reverse if necessary and identify by block number)					
<p>The use of unstructured, adaptive, embedded grids has been applied to hypersonic nonequilibrium CFD problems. Grid adaptation was accomplished by sub-dividing computational cells for 2-D and axisymmetric blunt body configurations. The high temperature gas mixture was described by Lighthill's dissociating gas model which was extended to include multiple coupled reaction paths in both viscous and inviscid flows. Ni's finite volume Lax-Wendroff scheme was used to integrate the governing equations. This algorithm was extended to include shock fitting and adaptation on general, unstructured, time dependent grids.</p> <p>The explicit real-gas algorithm and shock fitting procedure were validated by comparisons with experimental and computational results for perfect gas, dissociating gas, and multiple reaction cases. These comparisons also emphasized the importance of chemical length scale effects in predicting nonequilibrium gas behavior. Such effects were linked not only to</p>					
(cont. on back)					
20. DISTRIBUTION/AVAILABILITY OF ABSTRACT <input checked="" type="checkbox"/> UNCLASSIFIED/UNLIMITED <input type="checkbox"/> SAME AS RPT <input type="checkbox"/> DTIC USERS			21. ABSTRACT SECURITY CLASSIFICATION UNCLASSIFIED		
22a. NAME OF RESPONSIBLE INDIVIDUAL K. Mach			22b. TELEPHONE (Include Area Code) (513) 255-2455		22c. OFFICE SYMBOL WRDC/FIMM

19. Abstract (continued)

species concentration profiles throughout the shock layer, but also to the excess production of Nitric Oxide frequently reported off the symmetry plane in reacting air blunt body flows.

A detailed study of basic nonequilibrium flow phenomena has been completed for freestream Mach numbers from 10 to 15 over blunted cones and wedges. These flows demonstrated degrees of nonequilibrium ranging from nearly frozen to near equilibrium. In all cases the adaptive procedure correctly located and resolved perfect gas and nonequilibrium features. Special attention was awarded to cases displaying a small departure from equilibrium. Here, adaptation was shown to be particularly useful in capturing the steep chemical gradients which appear within the shock layer. (nd)

Adaptation was shown to be a cost effective way of computing high resolution solutions to hypersonic, finite rate, real-gas problems. The computational effort required for an adaptively refined nonequilibrium solution was shown to be only 1.5 to 2 times that required for an equivalently resolved frozen flow solution over the same configuration. This compares favorably with the 40-50 times that may be required for a solution on globally refined mesh capable of resolving the chemical relaxation.

Accession For	
NTIS GRA&I	<input checked="" type="checkbox"/>
DTIC TAB	<input type="checkbox"/>
Unannounced	<input type="checkbox"/>
Justification	
By	
Distribution/	
Availability Codes	
Dist	Avail and/or Special
A-1	



Contents

<u>Introduction</u>	<u>Page</u>
Motivation and Overview	1
Organization	2
 <u>PART I Real Gas Dynamics</u>	 4
1 Some Elements of High Temperature Gas Dynamics	4
1.1 Conservation Equations for Chemically Reacting Viscous Flows	6
1.2 Chemical Effects in High Temperature Air	13
 2 Modeling High Temperature Air	 17
2.1 Thermodynamics of a Mixture of Ideal Dissociating Gases	17
2.2 Law of Mass Action	21
2.3 Finite Rate Expressions	27
2.4 Chemical Source Terms	31
2.5 Rate Constants	33
 <u>Part II An Adaptive Numerical Method</u>	 34
3 Numerical Integration of Governing Equations	34
3.1 Integration in One Dimension	35
3.2 Ni Scheme in Two Dimensions with Source Terms	37
3.3 Smoothing Formulation	42
3.4 Numerical and Physical Boundary Conditions	49

TABLE OF CONTENTS (continues)		<u>Page</u>
4	Adaptation and Unstructured Meshes	56
4.1	General Procedure	57
4.2	Detection of Flow Features	58
4.3	Unstructured Grids	68
4.4	Cell Division	70
4.5	Cell Interfaces	74
4.6	Integration Scheme on Interface Cells	79
 5	 Unstructured Shock Fitting	 82
5.1	Perfect Gas Shock Fitting	84
5.2	Equilibrium Shock Fitting	87
5.3	Moving Unstructured Meshes	90
5.4	Behavior of Shock Fit Solutions	92
 Part III	 <u>Presentation and Discussion of Results</u>	 95
 6	 Physical Phenomena in High Temperature Flows Over Simple Geometries	 95
6.1	Basic Examples and Algorithm Verification	95
6.2	Effects of Length Scale Behavior	105
6.3	Coupled Reacting Systems	114
 7	 Effectiveness of Adaptive Grid Embedding in Hypersonic Flows	 118
7.1	Enhancement of Computational Efficiency	118
7.2	Adaptive Resolution of Physical Phenomena	122
7.3	Recommendations for Improving the Adaptive Technique	124

TABLE OF CONTENTS (concluded)		<u>Page</u>
<u>Summary</u>		127
Summary and Conclusions		127
Conclusions		129
<u>References</u>		130
<u>Appendices</u>		
A	Integration Formulae	133
A.1	Non-Orthogonal Two Dimensional Coordinates	133
A.2	Non-Orthogonal Axisymmetric Coordinates	135
A.3	Viscous Formulation in Two-Dimensions	137
B	Jacobian Matrices	141
B.1	Perfect Gas	141
B.2	Nonequilibrium Mixture Gas Model	142

Figures

Figure	Page
1.1 Velocity - Altitude map with regions of modal excitation superimposed on it. (From Ref. 20.).....	5
1.2 Composition of equilibrium air as a function of temperature at 1 atm pressure (1).....	13
1.3 Equilibrium constants for neutral species of air. (From Ref. 33.).....	15
2.1 Energy level comparison of equilibrium air between half-excited model and more precise model of reference (14) (Reproduced from Ref. (31).	18
2.2 Characteristic density ρ_D , for the three major diatomic molecules in high temperature air.	26
3.1 A one-dimensional computational domain.....	35
3.2 A two-dimensional computational domain.....	37
3.3 A two-dimensional computational domain for integral formulation.	39
3.4 Schematic of changes accumulated at the i^{th} node in a two-dimensional domain.	41
3.5 Amplification factor of the Lax-Wendroff finite difference scheme. (From Ref. 2.)	42
3.6 A one-dimensional computational domain smoothing formulation.....	43
3.7 A two-dimensional computational domain smoothing formulation.....	43
3.8 A one-dimensional computational domain for examining smoothing contributions.	44
3.9 Variation of property μ showing degeneracy of smoothing operator near boundaries.....	45
3.10 Stagnation streamline temperature behavior in a frozen flow.....	47
3.11 Schematic of physical and computational space for a blunt body computation.....	49
3.12 Edge cells in a node-based finite-volume scheme.....	50
3.13 Schematic of outflow boundary in blunt body flow showing location of the sonic line.....	51
3.14 Flow tangency condition for inviscid simulations showing reorientation of the total velocity vector.....	52
3.15 No contribution to flux integral from surface face.....	54

4.1	Some flow features in hypersonic, real-gas, blunt body flows.	59
4.2	General undivided cell.....	61
4.3	An adaptation map based on two parameters.	62
4.4	Adaptation map for Mach 5 flow showing polarization.....	63
4.5	Behavior of a general adaptation map.....	64
4.6	Adaptation based on different parameters.	65
4.7	Adaptive sequence on a blunt nose.....	67
4.8	General cell in unstructured domain.....	69
4.9	Cell numbers surrounding a node.....	69
4.10	Cell A tagged for division.....	72
4.11	Cell division and pointer updating.	73
4.12	Interface in computational mesh.....	74
4.13	Comparison of interface cells with cells of a uniform grid.....	74
4.14	Distribution to mid-face node.....	78
4.15	General interface cell.....	80
5.1	Definition of <i>normal relative Mach number</i>	85
5.2	Definition of <i>absolute normal Mach number</i>	85
5.3	Reference points for moving nodes on the base (original) grid.....	90
5.4	Preservation of linear interfaces in an unstructured domain with multiple levels of adaptive embedding.....	92
5.5	A typical history of stand-off distance with iteration, converged from a uniform, freestream initial condition. (Mach 5 frozen flow over an axisymmetric nose.)	93
6.1	Comparison of shock Stand-off with Reference 22.....	96
6.2	Computed Mach contours of Mach 5 frozen flow over 2-D and axisymmetric circularly blunted bodies showing location of the sonic line.....	98
6.3	Density ratio comparison with shock tube experiment and calculation of Macrossan (25) at conditions of Table 6.1. Current method shown in lower half.....	100
6.4	Adaptive computational grid with 1640 nodes for dissociating Nitrogen flow over a circularly blunted 15° wedge at "equivalent" conditions (Table 6.1).....	101

6.5	Stagnation streamline profiles of density ratio of current method and computations of Candler (5) at conditions in Table 6.2.....	103
6.6	Stagnation streamline profiles of temperature and species mass fraction of current method and computations of Candler (5) at conditions in Table 6.2.....	104
6.7	Schematic of generalized concentration and source term behavior along the stagnation streamline in inviscid flow.....	106
6.8	Stagnation streamline profiles of atom mass fraction and local equilibrium mass fraction for the blunted wedge detailed in Table 6.1 with chemical rate retarded two orders of magnitude.....	107
6.9	Symmetry plane profile of the logarithm of the source term normalized by that just behind the frozen shock for the blunted wedge detailed in Table 6.1, with chemical rate retarded two orders of magnitude.....	108
6.10	Mass fraction profiles and local equilibrium mass fractions for reacting flows ranging from near frozen to near equilibrium.....	111
6.11	Mass fraction and local equilibrium mass fraction profiles along the symmetry plane for viscous and inviscid flows at 60 km altitude in STD atmosphere. $\Psi = 10$ (left), $\Psi = 0.01$ (right), $Re = 6500$, $Pr = 0.72$, $Sc = 0.5$	112
6.12	Symmetry plane profiles of species mass fractions for the case detailed in Table 6.2. (also see Figs. 6.5 and 6.6)	113
6.13	Symmetry plane profiles of species mass fraction for O_2 , O , NO , and N for the case detailed in Table 6.2 (also see Figs. 6.5 & 6.6).....	115
6.14	Contours of NO mass fraction, and temperature ratio for the case detailed in Table 6.2 (also see Figs. 6.5 & 6.6).....	116
7.1	Adapted grid with four levels of embedding and 1550 nodes for conditions described in text.....	119
7.2	Contours of temperature ratio for inviscid Mach 12 flow for frozen flow (left), and reacting flow (right).....	122
7.3	Cell subdivisions for directional embedding.....	125
7.4	Adapted grid for a 2-D reacting viscous calculation and total velocity vectors for same calculation.	125
A.1	A general cell in circular cylindrical coordinates.....	135
A.2	Primary and Secondary cells for viscous integration.	137

List of Tables

<u>Table</u>	<u>Page</u>
1-1 Scaling of Flow Variables and Properties used to Non-Dimensionalize the Governing Equation.....	9
2-1 Characteristic Temperatures and Densities For Dissociation of the Major Molecular Species in Equilibrium Air Below 9000 K.....	26
6-1 Conditions for Comparison to Dissociating Nitrogen Test Case (from Reference 25).....	99
6-2 Conditions for Spherical Test Case of Reference (5) for Multiple Reaction Comparison.....	102
7-1 Computing Time Comparisons for Adaptive and Globally Refined Meshes for Conditions of Figure 7.1	120

Nomenclature

Symbols

a	Speed of sound
AC	Adaptation parameter
c	Concentration
D_{im}	Binary diffusion coefficient
E	Internal energy per unit mass
e	Total internal energy per unit volume
\bar{E}	Internal energy of an inert mixture
F, G	Inviscid flux vectors
h	Enthalpy
k	Heat conduction coefficient
M	Mach number
m_n	Mass per mole of n^{th} species
N^n	Number of particles of type n
N_n	Total number of elements with n type nuclei
p	pressure
q	Heat flux vector
Q^n	Partition function of n^{th} species
R, S	Viscous flux vectors
\mathfrak{R}	Universal gas constant
R_n	Nose radius
s	Total number of species
T	Temperature
T_{adapt}	Adaptation threshold
U	State Vector
u, v	Cartesian velocity components
\hat{U}	Diffusion velocity vector
V	Total velocity vector

Greek Symbols

α	degree of dissociation
ϵ_0	Activation energy
Φ	Non-dimensional reaction rate expression
γ	Frozen ratio of specific heats
η	temperature exponent
κ	Boltzman's constant
Λ_{relax}	Chemical relaxation length
μ	First coefficient of dynamic viscosity
Θ_D	Characteristic temperature for dissociation
ρ_D	Characteristic density for dissociation
σ	Numerical smoothing coefficient
τ_{ij}	shear stress tensor
Ψ	Damköhler number

Subscripts

$()_F$	Frozen
$()_i$	Species
$()_j$	Molecular species
$()_n$	Normal direction
$()_o$	Stagnation value
$()_\infty$	Freestream condition

Superscripts

$()^*$	Non-dimensional quantity
---------	--------------------------

INTRODUCTION

Motivation and Overview

The difficulty involved in experimentally validating NASP type high altitude/high Mach number configurations has driven a large hypersonic CFD effort. The nonequilibrium real gas effects and steep gradients found in this regime are characterized by multiple time and length scales. Specifically, the relaxation lengths for such nonequilibrium processes often differ from the convective length scale by several orders of magnitude, introducing both stiffness and complexity into attempted analysis (1,31). Moreover, these nonequilibrium length scales may change radically throughout the field. In terms of numerical simulation, these factors drive up the cost of computation by grossly increasing the resolution requirements for acceptable solutions (30,32).

In response to such needs, the technique of *adaptive grid embedding* locally refines the computational mesh based on information from a developing solution (6,16,33). Triggered by both gas dynamic and nonequilibrium variables, embedding increases the resolution of flow features associated with these processes. In this way, the grid scale locally adapts to the dominant physical scale within the gas. The technique ensures grid resolution comparable with all important physical scales of the problem while still avoiding unnecessary resolution in smoother regions of the flow.

Of course, in reacting blunt body flows, the chemical and convective lengths are not the only scales in the flow. The bow shock adds a third type of length scale. However, since

this structure is on the order of the local mean free path, its scale is too disparate to attempt to resolve. In fact, with the exception of transatmospheric problems, the bow shock may be treated as a discontinuity. With this motivation, *shock fitting* removes the shock from the domain interior in the present work. The discontinuous shock assumption is consistent with a continuum description of the flow, but breaks down in the large Knudsen number regime characteristic of very high altitude flight (28).

From a computational standpoint, an adaptive embedding procedure requires unstructured data storage and a compact computational stencil. In response to these pressures, Ni's (29) node-based finite-volume scheme was chosen. Over the course of the research the initial inviscid perfect gas scheme was extended to include chemical source terms, viscous terms, and axisymmetric configurations.

Organization

This work is divided into three main parts. The first takes up high temperature gas dynamics. After briefly discussing nonequilibrium and real gas phenomena in air, it develops the governing equations and gas model used to describe chemically reacting high temperature air. The model applies to both coupled and uncoupled reacting mixtures and degenerates to a classical perfect gas when the chemistry is frozen. The final results of these discussions are the chemical source terms for use in the governing equations.

In Part II, focus shifts to the adaptive numerical algorithm and its associated numerical procedures. The integration scheme emphasizes the conservative nature of the governing equations. Discussions of the embedded mesh procedure also stress this point, especially with respect to the treatment of computational interfaces between embedded mesh levels. This

Part closes with a presentation of shock fitting algorithms for both nonequilibrium and equilibrium real gas models.

Part III contains the major results and conclusions. These discussions include analysis of both fundamental physical phenomena in blunt body flows and an overall look at the effectiveness of the adaptive procedure in a hypersonic environment. In examining the physical process found in high temperature shock layers, the analysis emphasizes the importance of length scales and their effect on the flow's behavior. Such investigations gave experience with the adaptive method as an engineering tool, and they provided a firm basis for evaluating the effectiveness of the embedded procedure.

I REAL GAS DYNAMICS

1. Some Elements of High Temperature Gas Dynamics

We briefly discuss some aspects of high temperature gas flows and present an extended form of the conservation equations to model such flows. This permits close study of the terms responsible for modeling the physics of gases at elevated temperatures. The examination reveals the strengths and weaknesses in the present modeling, and provides insight into which physical processes may be described within this framework.

Physical Processes

Nonequilibrium involves both the chemical composition and the internal energy storage modes of the gas particles. In steady, air breathing flight within the Earth's atmosphere, hypersonic vehicles experience both kinds of nonequilibrium. Figure 1.1 shows the corridor for sustained flight with regions of thermo-chemical excitation superimposed (20). Despite the somewhat approximate boundaries in the sketch, it is clear that these modes affect nearly all flight at hypersonic Mach numbers.

Nonequilibrium Rate Processes

While excitation of internal modes is important, excitation alone does not imply a relevant nonequilibrium process. In the context of flowing gases, nonequilibrium implies that the time for an energy mode to equilibrate is an appreciable fraction of some time scale within the flow. On average, chemical reactions require thousands of collisions between the reactants. These collisions occur over a finite time and distance. In general, the more efficient

energy transfer between internal modes of a particle implies less space and time to achieve equilibrium. This observation often leads to a *heavy particle temperature* approximation (21). The temperature characterizes a particle's internal energy by assuming thermal equilibrium takes place instantaneously. That is, all internal modes remain in equilibrium with each other. While valid throughout much of the flight corridor in Figure 1.1, recent work by Candler (5), Park (31), and others (4) suggests that the approximation breaks down near orbital conditions.

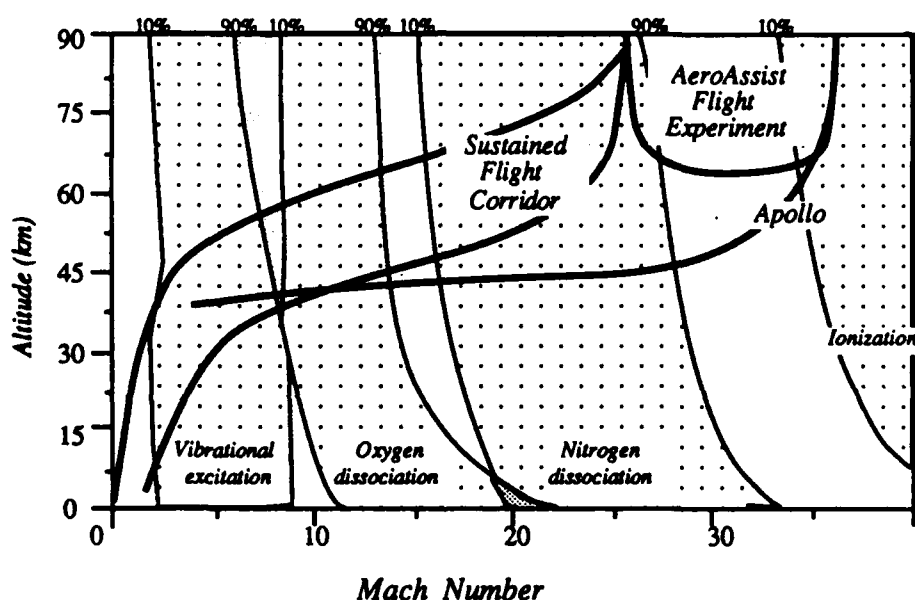


FIGURE 1.1
Velocity - Altitude map with regions of modal excitation superimposed on it. (From Ref. 20.)

At elevated Mach numbers and low densities, the vibrational temperature may take appreciable time (and distance) to equilibrate with the translational-rotational temperature. This results in thermal nonequilibrium within the different molecular species in heated regions of the shock layer. In this context, "molecular species" refers mainly to nitrogen, since oxygen molecules tend to dissociate before their vibrational and translational temperatures differ appreciably. It is worth noting, however, that the stagnation enthalpy error produced by ignoring this temperature difference is negligibly small for a wide class of problems. Thus, while multiple vibrational temperatures remain important in re-entry or transatmospheric problems, a

one-temperature model does accurately model a wide class of problems within the Earth's atmosphere.

1.1 Conservation Equations for Chemically Reacting Viscous Flow

Many texts develop the conservation equations for chemically reacting viscous flows (for example (36), (13), (1)). This section first states this set and then discusses specific modeling for terms within these relations.

Governing Equations in Conservative Form

Global conservation of mass and momentum simply account for mass and momentum flux through a fluid without concern for any internal structure of the gas particles. The description therefore remains unchanged from the classical Navier-Stokes or Euler formulation. In full conservation form:

Continuity

$$\frac{\partial \rho}{\partial t} + \nabla \cdot (\rho \mathbf{V}) = 0 \quad (1.1)$$

x Momentum

$$\frac{\partial(\rho u)}{\partial t} + \frac{\partial(\rho u^2 + p)}{\partial x} + \frac{\partial(\rho uv)}{\partial y} = \frac{\partial(\tau_{xx})}{\partial x} + \frac{\partial(\tau_{xy})}{\partial y}$$

y Momentum

$$\frac{\partial(\rho v)}{\partial t} + \frac{\partial(\rho uv)}{\partial x} + \frac{\partial(\rho v^2 + p)}{\partial y} = \frac{\partial(\tau_{yx})}{\partial x} + \frac{\partial(\tau_{yy})}{\partial y} \quad (1.2)$$

Here, the shear stresses are

$$\tau_{xy} = \tau_{yx} = \mu \left(\frac{\partial v}{\partial x} + \frac{\partial u}{\partial y} \right)$$

and the normal viscous stresses are

$$\tau_{xx} = (\lambda + 2\mu) \frac{\partial u}{\partial x} + \lambda \frac{\partial v}{\partial y}$$

$$\tau_{yy} = (\lambda + 2\mu) \frac{\partial v}{\partial y} + \lambda \frac{\partial u}{\partial x}$$

The Stokes hypothesis eliminates the second coefficient of viscosity by setting $\lambda = -\frac{2}{3}\mu$.

$$\tau_{xx} = \frac{2}{3}\mu \left(2 \frac{\partial u}{\partial x} - \frac{\partial v}{\partial y} \right)$$

$$\tau_{yy} = \frac{2}{3}\mu \left(2 \frac{\partial v}{\partial y} - \frac{\partial u}{\partial x} \right)$$

Since the energy equation imposes a detailed balance of all energy fluxes, it must include an explicit description of the diffusive energy flux arising from gradients in species concentrations. However, collecting those effects within the heat flux term, q , the equation to be couched in classical form.

$$\frac{\partial(e)}{\partial t} + \frac{\partial[u(e+p)]}{\partial x} + \frac{\partial[v(e+p)]}{\partial y} = \frac{\partial}{\partial x}(u\tau_{xx} + v\tau_{xy} - q_x) + \frac{\partial}{\partial y}(u\tau_{yx} + v\tau_{yy} - q_y) \quad (1.3)$$

Here e refers to the *total internal energy per unit mass*, and the stagnation enthalpy becomes:

$$h_o = \frac{e+p}{\rho} \quad (1.4)$$

As mentioned, q includes both the Fourier heat conduction term, and the diffusive energy flux contributions.

$$q = -k\nabla T + \sum_i \rho_i \hat{U}_i h_i \quad (1.5)$$

Here, \hat{U}_i is the diffusion velocity of the i^{th} component in the mixture. More precisely, \hat{U}_i measures the relative velocity of the i^{th} species to the bulk velocity of the gas.

The diffusion velocity also contributes to the species conservation equations. These relations trace the net production or destruction of each species in the mixture.

For the i^{th} species:

$$\frac{\partial(\rho_i)}{\partial t} + \frac{\partial(\rho_i u)}{\partial x} + \frac{\partial(\rho_i v)}{\partial y} = \dot{W}_i + \frac{\partial(\rho_i \hat{u}_i)}{\partial x} + \frac{\partial(\rho_i \hat{v}_i)}{\partial y} \quad (1.6)$$

The source term \dot{W}_i contains the net reaction rate expression, and in general is a summation over all reactions contributing to the net rate of change of any particular species.

Naturally, conservation of atomic nuclei and electrons prohibits the gross numbers of particles of any species from changing.

$$\sum_i \dot{W}_i = 0 \quad (1.7)$$

Additionally, global continuity forces the net diffusive flux of all individual species to cancel.

$$\sum_i \rho C_i \hat{U}_i = 0 \quad (1.8)$$

State Vector Form

The conservative form of the governing equations permits an arrangement more amenable to numerical computation.

$$\frac{\partial U}{\partial t} + \frac{\partial F}{\partial x} + \frac{\partial G}{\partial y} = \frac{\partial R}{\partial x} + \frac{\partial S}{\partial y} + W \quad (1.9)$$

Here

$$U = \begin{bmatrix} \rho \\ \rho u \\ \rho v \\ e \\ \rho_i \\ \vdots \\ \rho_s \end{bmatrix}, \quad F = \begin{bmatrix} \rho u \\ \rho u^2 + p \\ \rho uv \\ u(e + p) \\ \rho_i u \\ \vdots \\ \rho_s u \end{bmatrix}, \quad G = \begin{bmatrix} \rho v \\ \rho uv \\ \rho v^2 + p \\ v(e + p) \\ \rho_i v \\ \vdots \\ \rho_s v \end{bmatrix}$$

and

$$\mathbf{R} = \begin{bmatrix} 0 \\ \tau_{xx} \\ \tau_{xy} \\ (u\tau_{xx} + v\tau_{xy} - q_x) \\ \rho_i \hat{u}_i \\ \vdots \\ \rho_s \hat{u}_s \end{bmatrix}, \quad \mathbf{S} = \begin{bmatrix} 0 \\ \tau_{xy} \\ \tau_{yy} \\ (u\tau_{xy} + v\tau_{yy} - q_y) \\ \rho_i \hat{v}_i \\ \vdots \\ \rho_s \hat{v}_s \end{bmatrix}, \quad \mathbf{W} = \begin{bmatrix} 0 \\ 0 \\ 0 \\ 0 \\ W_i \\ \vdots \\ W_s \end{bmatrix}$$

\mathbf{F} and \mathbf{G} are the *inviscid flux vectors* while \mathbf{R} and \mathbf{S} contain the viscous fluxes. Setting the *viscous flux vectors* identically to zero results in the governing equations for chemically reacting inviscid gas mixtures. \mathbf{W} contains the chemical source terms for either case. Setting this vector to zero degenerates the set of equations further and results in the Euler equations for perfect gas modeling.

Normalization

Table 1.1 shows the scaling of flow variables and properties used to non-dimensionalize the governing equations. The subscript $()_F$ refers to frozen conditions.

TABLE 1.1

Scaling of flow variables and properties used to non-dimensionalize the governing equations.

<i>Dimensional variable</i>	<i>Reference quantity</i>	<i>Non-dimensional freestream value</i>
ρ u, v e	ρ_∞ a_{F_∞} $\rho_\infty a_{F_\infty}^2$	1 $M_{x_\infty}, M_{y_\infty}$ Dependent upon modeling
p T t	$\rho_\infty a_{F_\infty}^2$ T_∞ R_N/a_{F_∞}	$1/\gamma_{F_\infty}$ 1 —
μ k Dim	μ_∞ k_∞ Dim_∞	1 1 1
x y	R_N R_N	— —

Taking the frozen sound speed as a reference velocity conveniently rescales the freestream flow velocity and Mach number to numerically equal values.

Non-Dimensionalization of Diffusion Properties

Inserting this scaling into the governing equations permits a collection of all dimensionless parameters within \mathbf{R} , \mathbf{S} , and \mathbf{W} . Collecting these parameters into the non-dimensional heat flux vector \mathbf{q} and shear stress tensor $\bar{\tau}$ leaves the form of the governing equation set (1.9) unchanged.

Defining the Reynolds, Prandtl, and Schmidt number (respectively) as

$$Re \equiv \frac{\rho_\infty a_{F_\infty} R_N}{\mu_\infty}, \quad Pr \equiv \frac{c_{pF_\infty} \mu_\infty}{k_\infty}$$

$$Sc \equiv \frac{\mu_\infty}{\rho_\infty Dim_\infty}$$

permits $\bar{\tau}$ to be expressed without dimension.

$$\begin{aligned}
\tau_{xx} &= \frac{2\mu^*}{3Re} (2u_x^* - v_y^*) \\
\tau_{yy} &= \frac{2\mu^*}{3Re} (2v_y^* - u_x^*) \\
\tau_{xy} &= \frac{\mu^*}{Re} (u_y^* + v_x^*)
\end{aligned} \tag{1.10}$$

where, $\mu^* = \frac{\mu}{\mu_{ref}}$, $u^* = \frac{u}{a_{F_m}}$, and $v^* = \frac{v}{a_{F_m}}$.

Since significant ionization occurs only at temperatures too high to simulate accurately within the present single temperature framework, any charge separation predicted due to ionic species must remain small. Given this, Fick's first law of diffusion relates the diffusion velocity to species gradients.

$$\hat{U}_i = -\frac{\rho}{\rho_i} D_{im} \nabla c_i \tag{1.11}$$

Collecting dimensional parameters in the energy equation returns a non-dimensional form of this quantity. In cartesian form the diffusion velocities become:

$$\hat{u}_i = -\frac{1}{Re Sc} \left(D_{im}^* \frac{\rho^*}{\rho_i^*} \frac{\partial c_i^*}{\partial x^*} \right), \quad \hat{v}_i = -\frac{1}{Re Sc} \left(D_{im}^* \frac{\rho^*}{\rho_i^*} \frac{\partial c_i^*}{\partial y^*} \right) \tag{1.12}$$

With these quantities now known, we may write the non-dimensional heat flux vector.

$$\mathbf{q} = \left(\frac{-k}{Pr Re \gamma_{F_m}} \nabla T - \sum_i \frac{\rho h_i D_{im}}{Re Sc} \nabla c_i \right)^*$$

Breaking this vector into its cartesian components, \mathbf{q} becomes;

$$q_x = \left(\frac{-k}{Pr Re \gamma_{\infty}} \frac{\partial T}{\partial x} - \sum_i \frac{\rho h_i D_{im} \partial c_i}{Re Sc \partial x} \right)^* \quad (1.13)$$

$$q_y = \left(\frac{-k}{Pr Re \gamma_{\infty}} \frac{\partial T}{\partial y} - \sum_i \frac{\rho h_i D_{im} \partial c_i}{Re Sc \partial y} \right)^*$$

After developing a mixture gas model, the next chapter details the non-dimensionalization of chemical source terms.

Modeling of Diffusion Properties

Precise modeling of diffusion properties requires details of the collision cross-sections from kinetic theory (21, 36). However, the level of accuracy for the current modeling does not warrant such details. Moreover, μ and k should take into account mixture values in reacting calculations, but such effects are of higher order, and are not crucial for understanding the basic physics here.

Sutherland's law predicts μ to within 10% below 9000 K (10). All viscous calculations presented later use this approximation.

$$\mu^* \equiv \frac{\mu}{\mu_{\infty}} = \left[\frac{T_{\infty} + 110.4}{T + 110.4} \right] \left(\frac{T}{T_{\infty}} \right)^{\frac{3}{2}} \quad (1.14)$$

The definition of Prandtl number relates thermal conductivity to viscosity.

$$k_{\infty} = \frac{\mu_{\infty} c_{p_{\infty}}}{Pr_{\infty}}$$

A constant Prandtl number assumption provides a first approximation for the high temperature transport property behavior,

$$k^* \equiv \frac{k}{k_{\infty}} = \frac{\mu^* \frac{c_p}{c_{p_{\infty}}}}{\frac{Pr}{Pr_{\infty}}} \equiv \mu^* \frac{c_p}{c_{p_{\infty}}} \quad (1.15)$$

Unless otherwise stated, all viscous calculations assume that $c_p/c_{p_{\infty}} = 1.0$.

Similarly, the definition of Sc provides a basis for evaluating D_{im}

$$D_{im_{\infty}} = \frac{\mu_{\infty}}{\rho_{\infty} Sc} \rightarrow D_{im}^* \equiv \frac{D_{im}}{D_{im_{\infty}}} = \frac{\mu^*}{\rho^*} \quad (1.16)$$

for constant Schmidt number modeling.

The Degree of Nonequilibrium

The earlier statement that nonequilibrium is relevant when relaxation occurs over an "appreciable" distance was accurate, but not very quantitative. A clearer statement of the degree of nonequilibrium relates the fluid and chemical time scales

Consider a steady state inviscid species equation. From Equation (1.6),

$$\frac{\partial(\rho_i u)}{\partial x} = \dot{W}_i \quad (1.17)$$

This may be non-dimensionalized as before with freestream conditions.

$$\frac{\partial(\rho_i u)^*}{\partial x^*} = \frac{R_n \dot{W}_{i,ref}}{\rho_{\infty} a_{\infty}} \dot{W}_i^* \equiv \Psi \dot{W}_i^* \quad (1.18)$$

Here, Ψ is a form of the Damköhler number and relates the chemical reaction rate to the bulk fluid motion. The reference reaction rate, $\dot{W}_{i,ref}$, was evaluated at conditions downstream of a normal shock. As Ψ increases, the chemical length scale shrinks until identical equilibrium modeling describes the flow. Similarly as Ψ approaches zero the flow becomes progressively more frozen.

1.3 Chemical Effects in High Temperature Air

With the governing equations for a general nonequilibrium chemically reacting gas mixture completely outlined, we next examine how they model a known system. Moreover, the chemical composition of high temperature air will provide a datum by which to judge the results of later computations. For equilibrium air, the species equations reduce to the equivalent Law of Mass Action form.

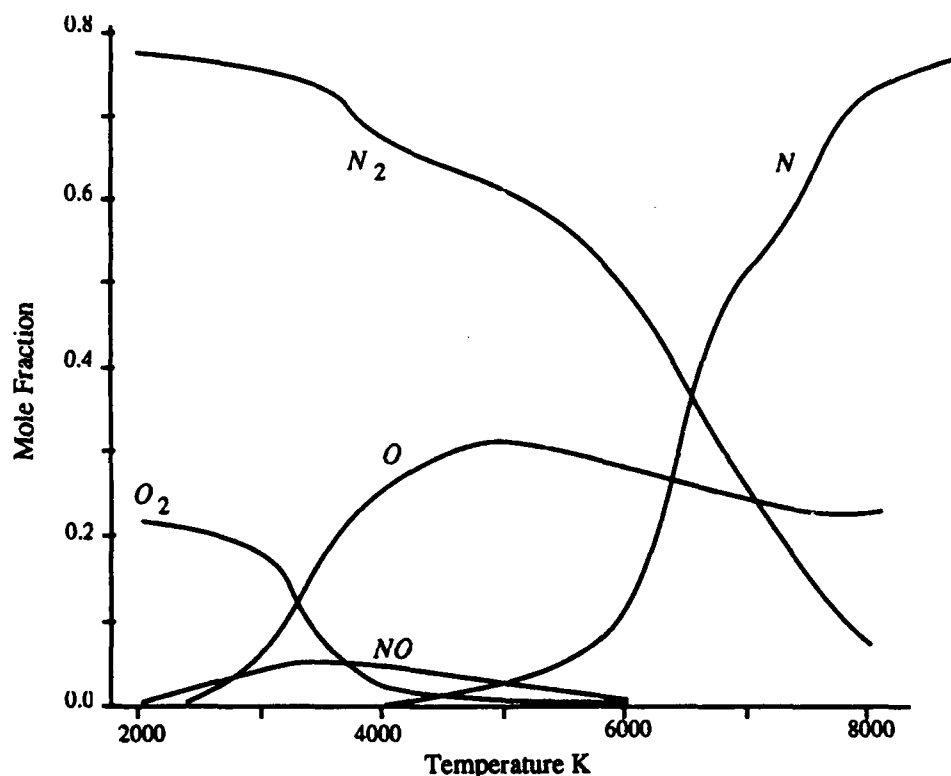


FIGURE 1.2
Composition of equilibrium air as a function of temperature at 1 atm pressure (1).

Figure 1.2 illustrates the temperature dependence of the equilibrium mole fraction X for the five major constituents of air. The mole fraction of the i^{th} species X_i is defined as the ratio of the number of moles of i , N_i , to the total number of moles in the mixture N .

At atmospheric pressure, the system remains quiescent from a few degrees above absolute zero to nearly 800 K. Over this range, rotation and translation are fully excited, and

the equipartition principle dictates that both modes participate in energy storage. At about 800 K, the vibrational mode begins to contribute to such storage, but overall energy levels are insufficient to appreciably dissociate any of the vibrating molecules. Classically speaking, this vibrational excitation alters the specific heat ratio - affecting such things as the relationship between pressure and internal energy of a static gas.

At about 2000 K, these relatively benign effects change character. Molecular vibration and collisions have now increased to the point where appreciable oxygen dissociates. Again the specific heat ratio begins to change rapidly, except that now it varies more wildly, since changes in temperature also bring about changes in composition.

By 4000 K, only trace amounts of O_2 remain, and N_2 begins to dissociate. This process continues until essentially only atomic species survive above 9000 K. At such temperatures, the equilibrium constants favor atoms, and the diatomic species which do form exist only long enough to dissociate again. Above this temperature, additional thermal energy can only be stored by breaking down the electronic bonds holding electrons to the atomic nuclei.

One interesting feature is the bubble of NO appearing between 2000 and 6000 K. As background, consider the five basic neutral species reactions in the air system (below 9000 K).

1. $N_2 + M \rightleftharpoons 2N + M$
2. $O_2 + M \rightleftharpoons 2O + M$
3. $NO + M \rightleftharpoons N + O + M$
4. $NO + O \rightleftharpoons N + O_2$
5. $O + N_2 \rightleftharpoons NO + N$

The last two *exchange reactions* (or "shuffle" reactions) are responsible for creating *NO* in the system. Atomic oxygen collides with nitrogen molecules, forming *NO* which dissociates more slowly than it is produced, shifting the equilibrium composition upward.

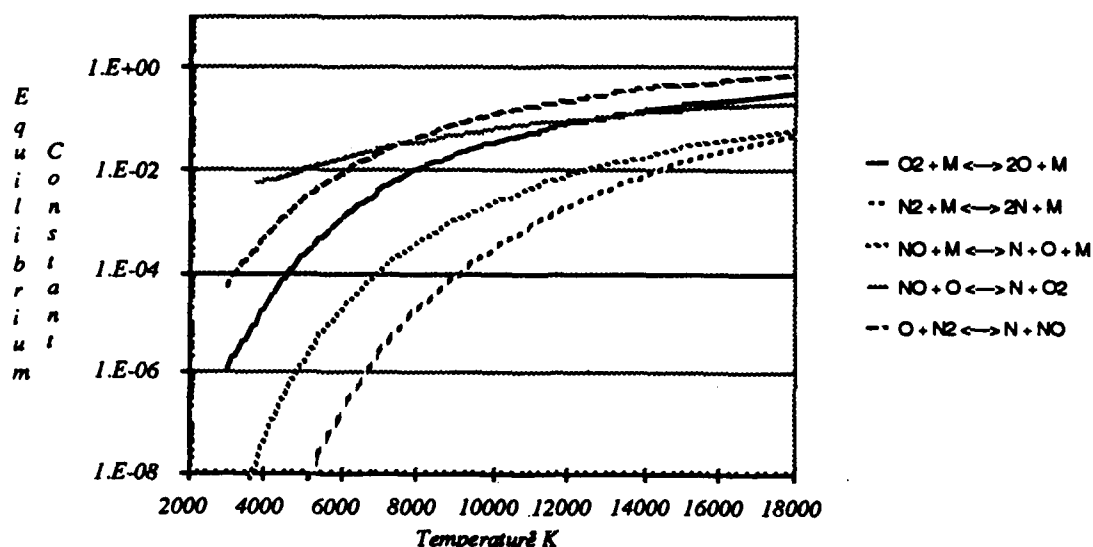


FIGURE 1.3
Equilibrium constants for neutral species of air. (From Ref. 33.)

Figure 1.3 provides greater insight into the role of the exchange reactions. This shows the equilibrium constants resulting from the ratio of the net forward to the backward rates of the five reaction system. Note that at relatively lower temperatures, the shuffle reactions proceed at rates orders of magnitude faster than the dissociation paths. At those temperatures, the reverse rates tend to dominate both (4) and (5), and the *NO* produced by (4) reacts in (5), tending to hold the overall level of *NO* nearly constant. Additionally, both reactions consume atomic nitrogen, further depleting whatever trace amounts may exist.

Although completed at standard pressure, the composition plot (Fig 1.2) holds qualitatively to quite low pressures. Lowering the pressure shifts the curves to the left, raising the degree of dissociation at any fixed temperature. Finally, this figure provides some reference state for the high temperature shock layers presented later.

2. Modeling High Temperature Air

The gas model developed to describe high temperature reacting flow extends the concept of a finite rate *ideal dissociating gas* (11, 23) to include both coupled and uncoupled systems. While capable of predicting the essential physical phenomena, this model introduces a minimum of algebraic complexity. Strictly speaking, it is reasonably accurate to 9000 K, and presently includes only electrically neutral species. Nevertheless, Chapter 6 presents evidence which demonstrates accurate modeling of flows where small portions of the shock layer include much higher temperatures.

After examining mixture thermodynamics, attention turns to the formulation of chemical source terms and details of the chemical modeling. Although the focus is on air chemistry, an extension to general mixtures is straightforward.

2.1 Thermodynamics of a Mixture of Ideal Dissociating Gases

The relationship between thermodynamic quantities in a system relies on the details of gas behavior on a molecular scale. The primary simplifications in the present modeling concern internal energy storage within molecular species. A single temperature characterizes all internal modes since the vibrational mode follows Lighthill's "half excited" assumption. In 1983, Park *et al* demonstrated that this assumption accurately predicts static enthalpy over the range of tem-

peratures where vibrational excitation is present (30). Figure 2.1 reproduces this work, comparing the static enthalpy and vibrational energy of Lighthill's model with a more accurate modeling (14). The indication is that only a small error exists over much of the shock layer.

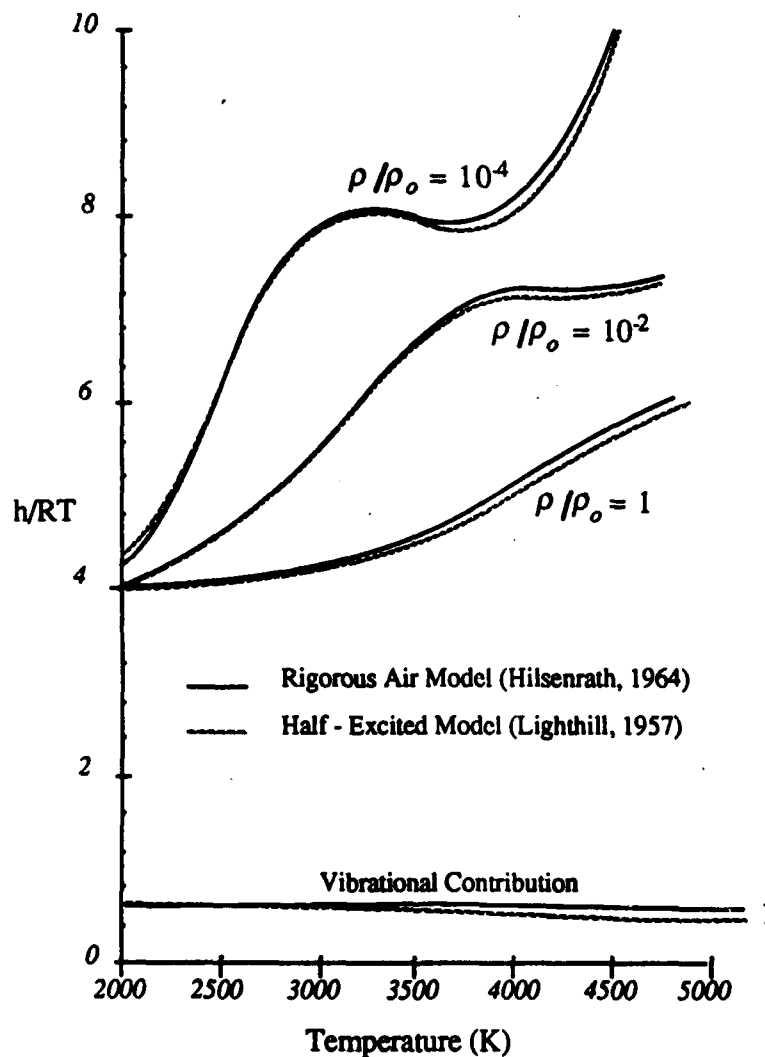


FIGURE 2.1
Energy level comparison of equilibrium air between half-excited model and more precise model of reference (14) (reproduced from ref. (31)).

Pressure

For ideal gas mixtures, Dalton's Law of Partial Pressures states that the total pressure is the sum of the contributions of each component.

$$p = \sum_i \rho_i \frac{\mathcal{R}}{m_i} T \quad (2.1)$$

Here, the density of the i^{th} species, ρ_i , is related to the total density by

$$\rho = \sum_i \rho_i \quad (2.2)$$

Since the law is purely mechanical, it remains unchanged in nonequilibrium flows.

Internal Energy and Enthalpy

The overall internal energy, E , for an inert mixture is the sum of the component internal energies.

$$\tilde{E} = \sum_i E_i$$

Here the tilde indicates that reactions are absent. The mixture enthalpy is

$$\tilde{h} = \sum_i E_i + \frac{p}{\rho}$$

making the *total internal energy per unit volume* of a mixture

$$e \equiv \left(E + \frac{V^2}{2} \right) \rho \quad (2.3)$$

With this definition, the total enthalpy becomes

$$h_o = \frac{e + p}{\rho} \quad (2.4)$$

If, however, the mixture is chemically reacting, the internal energy, E , must track the energy absorbed during dissociation. That is:

$$E = \sum_i E_i - \sum_{j=\text{dissociating}} c_j \frac{\mathcal{R}}{m_j} \Theta_{Dj} \quad (2.5)$$

In which Θ_{Dj} is the characteristic temperature for dissociation of the j^{th} molecular species.

Equation (2.5) implies that a mixture of only atoms will have zero energy at zero Kelvin. While convenient for some applications, this datum is not unique. Moreover, since at low temperatures air is virtually all molecules, we reset the datum to zero internal energy at absolute zero and 100% molecules.

$$E = \sum_s E_i + \sum_{j=\text{molecules}} \frac{\mathcal{R}}{m_j} \Theta_{Dj} (1 - c_j) \quad (2.6)$$

Energy Storage

Expressions for the internal energy of each species, E_i , stem from the kinetic theory of gases. Each species stores $\frac{1}{2} \mathcal{R} T$ for each equilibrium degree of freedom.

$$E_{Trans} = \frac{3}{2} R_{A_2} T, E_{Rot} = R_{A_2} T, \text{ and } E_{Vib} = R_{A_2} T$$

However, since the current model assumes vibration is only half excited, $E_{Vib} = \frac{1}{2} R_{A_2} T$.

In a system with atomic species, A , and molecular species, A_2

$$\text{Atomic Species: } E = E_{Trans} = \frac{3}{2} R_A T$$

$$\text{Molecular Species: } E = E_{Trans} + E_{Rot} + E_{Vib} = \frac{3}{2} R_{A_2} T + R_{A_2} T + \frac{1}{2} R_{A_2} T = 2 R_{A_2} T$$

For the specific mixture of the five major species in high temperature air N , O , NO , N_2 , and O_2 (species 1-5 respectively), the internal energy becomes

$$E = 3 \mathcal{R} T \left(\frac{1}{2} \frac{c_1}{m_1} + \frac{1}{2} \frac{c_2}{m_2} + \frac{c_3}{m_3} + \frac{c_4}{m_4} + \frac{c_5}{m_5} \right) + \mathcal{R} \left(\frac{\Theta_{D_3}}{m_3} + \frac{\Theta_{D_4}}{m_4} + \frac{\Theta_{D_5}}{m_5} \right) - \mathcal{R} \left(\frac{c_3 \Theta_{D_3}}{m_3} + \frac{c_4 \Theta_{D_4}}{m_4} + \frac{c_5 \Theta_{D_5}}{m_5} \right) \quad (2.7)$$

As a check, consider the special case of a symmetric dissociating gas, $A_2 \rightleftharpoons 2A$, with characteristic temperature Θ_D (i.e. with $c_2 = c_3 = c_5 = 0$, $c_4 = 1 - c_1$, and $m_4 = 2m_1$),

$$E = R_{A_2} (3T + c_A \Theta_D)$$

This is precisely Lighthill's result for the same case (36).

Finally, the integration scheme uses the total internal energy per unit volume, based on combining (2.3) and (2.7)

$$e = \rho \left[3\Re T \left(\frac{1}{2} \frac{c_1}{m_1} + \frac{1}{2} \frac{c_2}{m_2} + \frac{c_3}{m_3} + \frac{c_4}{m_4} + \frac{c_5}{m_5} \right) + \Re \left(\frac{\Theta_{D_3}}{m_3} + \frac{\Theta_{D_4}}{m_4} + \frac{\Theta_{D_5}}{m_5} \right) - \Re \left(\frac{c_3 \Theta_{D_3}}{m_3} + \frac{c_4 \Theta_{D_4}}{m_4} + \frac{c_5 \Theta_{D_5}}{m_5} \right) + \frac{V^2}{2} \right] \quad (2.8)$$

2.2 Law of Mass Action

The "half excited" assumption corresponds to certain behavior of the molecular partition function. This is expected, since those functions statistically describe how the energy storage modes of a particle behave. However, Lighthill's original work considered only symmetric diatomic gases, and a model of the complete air system must extend the analysis to include asymmetric particles such as *NO*.

For the general dissociation reaction, $AB \rightleftharpoons A + B$, the number densities measure

- $N_{AB} \equiv$ Total number of nuclei per unit volume (including those in both atoms and molecules)
- $N^A \equiv$ Number of *A* atoms per unit volume
- $N^B \equiv$ Number of *B* atoms per unit volume
- $N^{AB} \equiv$ Number of *AB* molecules per unit volume

Within this present framework, the total number of nuclei remains constant.

$$2N^{AB} + N^A + N^B = N_{AB} \quad (2.9)$$

From statistical mechanics, the law of mass action for this general system relates the number densities to the partition functions of each species and the change in zero point energy, $\Delta\epsilon_0$, of the reaction.

$$\frac{N^A N^B}{N^{AB}} = \frac{Q^A Q^B}{Q^{AB}} e^{-\Delta\epsilon/kT} \quad (2.10)$$

The change in zero point energy divided by Boltzman's constant, κ , is the characteristic temperature for dissociation, referred to earlier as Θ_D .

We may now define the *degree of dissociation* as the ratio of particles of a particular type to the total number of nuclei available.

$$\alpha_A \equiv \frac{N^A}{N_{AB}}, \quad \alpha_B \equiv \frac{N^B}{N_{AB}} \quad (2.11)$$

When combined with a statement of nuclei conservation,

$$N^{AB} = (1 - \alpha_A - \alpha_B) \frac{N_{AB}}{2} \quad (2.12)$$

we may define α_{AB} as

$$\alpha_{AB} \equiv (1 - \alpha_A - \alpha_B) = \frac{2N^{AB}}{N_{AB}} \quad (2.13)$$

Note that in single reaction systems with stoichiometric coefficients, little distinction is usually made between the degree of dissociation, α_i , and the mass fractions, c_i . However, if other kinds of particles are present, the degree of dissociation differs from the mass fraction, as will be detailed. For now, simply note that by definition $\alpha_A + \alpha_B + \alpha_{AB} = 1$, but $c_A + c_B + c_{AB}$ is not unity in the presence of other particles.

Repeating the law of mass action in terms of the degree of dissociation and the total number of nuclei, N_{AB} ,

$$\frac{\alpha_A \alpha_B}{\alpha_{AB}} = \frac{Q^A Q^B}{2 N_{AB} Q^{AB}} e^{-\Theta_D/T} \quad (2.14)$$

These nuclei have an average mass defined by

$$m' \equiv \frac{(m_A + m_B) N^{AB} + m_A N^A + m_B N^B}{N_{AB}} \quad (2.15)$$

m' remains constant for any reaction at any specific time provided that the reactants exist at stoichiometric ratios. Moreover, for any reaction in a multi-reaction system, we may define a density, ρ' , derived from the fraction of the mixture's density that is actually involved in any specific reaction.

$$\rho' \equiv \rho(c_A + c_B + c_{AB}) \quad (2.16)$$

From these above two definitions,

$$N_{AB} = \frac{\rho' V}{m'} \quad (2.17)$$

and the law of mass action becomes

$$\boxed{\frac{\alpha_A \alpha_B}{\alpha_{AB}} = \frac{m'}{2 \rho' V} \frac{Q^A Q^B}{Q^{AB}} e^{-\Theta_D/T}} \quad (2.18)$$

Notice again that since α_A , α_B , and α_{AB} represent the degree of dissociation, this form applies for systems containing other (possibly inert) reactions.

In the very special case of asymmetric dissociating reaction with no other species present and reactants at stoichiometric ratios, Equation (2.18) becomes

$$\frac{\alpha^2}{1 - \alpha} = \left(\frac{m}{2V} \frac{(Q^A)^2}{Q^{AA}} \right) \frac{e^{-\Theta_D/T}}{\rho} \quad (2.19)$$

The contents of the parenthesis on the right side have units of mass per volume. Moreover, for nitrogen and oxygen systems, the ratio of partition functions remains remarkably constant below 9000 K. By defining a *characteristic density*, ρ_D , we may approximate this term with a constant, thus avoiding the added complexity of evaluating partition functions. It is easy to show (36, pp. 159) that this simplification is equivalent to the "half excited" assumption stated earlier.

Characteristic Density of Asymmetric Molecules

Returning to the boxed Equation (2.18), we seek to define a characteristic density for this asymmetric reaction. However, the form of (2.18) is unfortunate since m' will vary when other reactions are present. Specifically, in a general mixture nothing insures that α_A will equal α_B , and thus there is the possibility of an excess of particles which will remain inert. Any attempt to define a ρ_D parameter will result in a quantity which varies according to m' .

In order to reexpress $\frac{m'}{\rho'}$, examine the definition of ρ' (2.16). Recall the *mass fraction* of the i^{th} species is the total mass of i divided by the total mass in the system,

$$\rho' \equiv \rho(c_A + c_B + c_{AB}), \text{ but } c_i \equiv \frac{m_i N^i}{\sum_j m_j N^j}$$

where

$$N^i = \frac{c_i}{m_i} \sum_j m_j N^j$$

Substituting for the mass fractions,

$$\rho' = \rho \left(\frac{m_A N^A + m_B N^B + m_{AB} N^{AB}}{\sum_j m_j N^j} \right) \quad (2.20)$$

in a mixture with s components. The total number of nuclei in this system stems from Equation (2.9):

$$N_{AB} = \frac{2c_{AB}}{m_{AB}} \sum_i m_i N^i + \frac{c_A}{m_A} \sum_i m_i N^i + \frac{c_B}{m_B} \sum_i m_i N^i \quad (2.21)$$

We now re-form the ratio $\frac{m'}{\rho'}$ from (2.10) and (2.16).

$$\frac{m'}{\rho'} = \frac{1}{\rho \left(\frac{c_A}{m_A} + \frac{c_B}{m_B} + \frac{2c_{AB}}{m_{AB}} \right)} \quad (2.22)$$

Defining \bar{m} as the *average mass per nucleus in AB molecules*,

$$\bar{m} \equiv \frac{m_A + m_B}{2} = \frac{m_{AB}}{2}$$

and multiplying both the numerator and denominator of (2.22) by this quantity results in

$$\frac{m'}{\rho'} = \frac{m'(\bar{m})}{\rho'(\bar{m})} = \frac{\bar{m}}{\rho \left[c_{AB} + \bar{m} \left(\frac{c_A}{m_B} + \frac{2c_B}{m_B} \right) \right]} \equiv \frac{\bar{m}}{\rho} \quad (2.23)$$

\bar{m} is constant for any reaction irrespective of any other inert or active species present. Thus, the variation has moved from m' into \bar{m} , while simultaneously re-expressing the ratio of (2.23) in terms of the (more common) mass fractions.

To demonstrate the value of this step, re-examine the law of mass action. Equation (2.18) becomes:

$$\frac{\alpha_A \alpha_B}{\alpha_{AB}} = \frac{1}{\rho} \left[\frac{\bar{m} Q^A Q^B}{2V Q^{AB}} \right] e^{-\Theta_D/T} \quad (2.24)$$

Following Lighthill, the term in the bracket may be defined as a characteristic density for dissociation of AB, ρ_{DAB} .

$$\rho_D \equiv \frac{\bar{m} Q^A Q^B}{2V Q^{AB}} \quad (2.25)$$

This form reduces identically to that presented by Lighthill in 1957 for a symmetric diatomic gas.

Values of ρ_D and Θ_D

Figure 2.2 displays plots of Equation (2.25) for the major diatomic species in equilibrium air below 9000 K. Reference 36 provided the values used in evaluation of the partition functions.

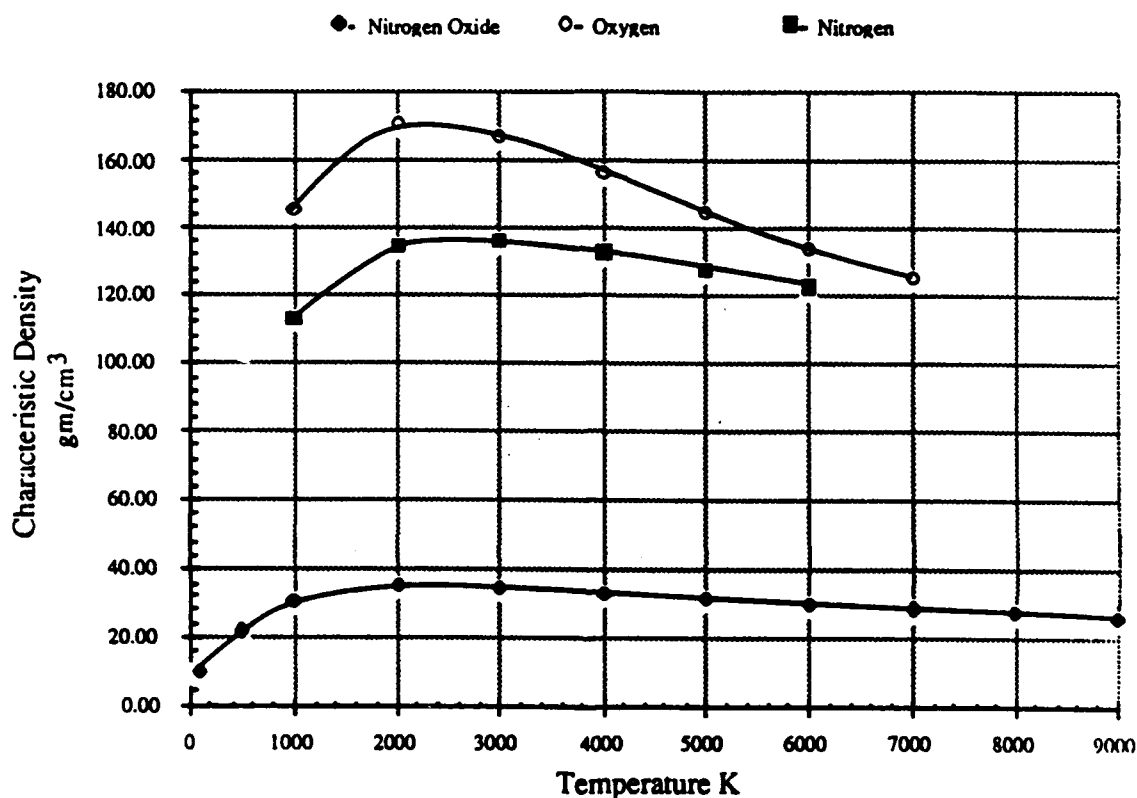


FIGURE 2.2

Characteristic density, ρ_D for the three major diatomic molecules in high temperature air.

Table 2.1 summarizes values of ρ_D , and Θ_D for N_2 , O_2 , and NO .

TABLE 2.1

Characteristic temperatures and densities for dissociation of the major molecular species in equilibrium air below 9000 K.

	N_2	O_2	NO
Characteristic Temp. (K)	113 000	59 500	75 500
Characteristic Density (kg/m³)	130 000	150 000	30 000

2.3 Finite Rate Expressions

Symmetric Diatomic Gas

Freeman (11) approximated the general chemical rate expression by separating the law of mass action into forward and backward components (37, pp. 232). For an ideal dissociating gas with law of mass action

$$\frac{\alpha^2}{1-\alpha} = \frac{\rho_D}{\rho} e^{-\Theta_D/T} \quad (2.26)$$

the rate of dissociation $d\alpha/dt$ is:

$$\frac{d\alpha}{dt} = CT^\eta \rho \left[(1-\alpha) e^{-\Theta_D/T} - \frac{\rho}{\rho_D} \alpha^2 \right] \quad (2.27)$$

which describes the production of atoms. Notice that for symmetric diatomic gases with no other species in the mixture, $\alpha = c_A$.

Mixture of Ideal Dissociating Gases

The law of mass action for asymmetric molecular dissociation with a half excited vibrational state (2.24) may be re-written in terms of the characteristic density and degree of dissociation.

$$\frac{\alpha_A \alpha_B}{\alpha_{AB}} = \frac{\rho_D}{\rho} e^{-\Theta_D/T} \quad (2.28)$$

The analog of (2.27) is simply

$$\frac{d\alpha_{AB}}{dt} = CT^\eta \rho \left[\frac{\bar{\rho}}{\rho_D} \alpha_A \alpha_B - \alpha_{AB} e^{-\Theta_D/T} \right] \quad (2.29)$$

which describes the production of AB molecules. Note that $\rho = \sum_s \rho_i$ as in (2.2).

Equation (2.29) describes AB production as a function of the degree of dissociation instead of mass fraction. Since the species equations express \dot{W} in terms of the mass fraction, (2.29) requires reformulation.

Recalling the definition of α_{AB} from (2.13) and then substituting for N^i and N_{AB} leads to

$$\frac{d\alpha_{AB}}{dt} = \frac{1}{[c_{AB} + \bar{m}(\frac{c_A}{m_A} + \frac{c_B}{m_B})]} \frac{dc_{AB}}{dt}$$

Re-arranging to express the mass fraction in terms of the degree of dissociation gives

$$\frac{dc_{AB}}{dt} = \frac{\bar{\rho}}{\rho} \frac{d\alpha_{AB}}{dt} \quad (2.30)$$

after substituting for $\bar{\rho}$ from (2.23).

For the symmetric diatomic case $\frac{\bar{\rho}}{\rho}$ reduces to unity, $c_A + c_B + c_{AB} = 1$, and $m_A = m_B$.

Equation (2.30) collapses to the rate expression (2.27).

Finally, for the general dissociative reaction, $AB \rightleftharpoons A + B$, in a mixture with many components

$$\frac{dc_{AB}}{dt} = CT^\eta \bar{\rho} \left[\frac{\bar{\rho}}{\rho_D} \alpha_A \alpha_B - \alpha_{AB} e^{-\Theta_0/T} \right] \quad (2.31)$$

This simple form appears to rely on fortuitous cancellation and careful definition of $\bar{\rho}$. However, by expressing the degree of dissociation in terms of mass fractions through the number densities N^i and total number of nuclei N_{AB} , one may show

$$\alpha_{AB} = \frac{\rho}{\rho} c_{AB}, \quad \alpha_A = \frac{\bar{m}}{m_A} \frac{\rho}{\rho} c_A, \quad \text{and} \quad \alpha_B = \frac{\bar{m}}{m_B} \frac{\rho}{\rho} c_B \quad (2.32)$$

Substituting back into (2.31) expresses the rate of change of species mass fractions as direct functions of these mass fractions of the reactants and products.

$$\boxed{\frac{dc_{AB}}{dt} = -CT\eta\rho \left[c_{AB}e^{-\Theta_0/T} - \left(\frac{\bar{m}^2}{m_A m_B} \right) \frac{\rho}{\rho_D} c_{ACB} \right]} \quad (2.33)$$

Here, again, \bar{m} is the average mass per atom in the AB molecule.

Elimination of Species Equations

With the species production terms formulated, attention returns to the governing equations. In general, as many species equations exist as species. However, for a system with only two types of nuclei, conservation permits discarding two differential equations - slightly reducing computational requirements and effort. In the present work, with the species N , O , NO , N_2 and O_2 numbered 1-5 (respectively), we elect to eliminate the last two species based on conservation of atoms.

The simplification is a convenience. Moreover, since we presently consider only the air system, the notation will refer to N and O directly, dropping the pretense of A and B .

$$\begin{aligned} \text{Nitrogen nuclei: } N_N &= 2N^{N_2} + N^N + N^{NO} \\ \text{Oxygen nuclei: } N_O &= 2N^{O_2} + N^O + N^{NO} \\ \text{Total number of nuclei: } N_{NO} &= N_N + N_O \end{aligned} \quad (2.34)$$

Differentiating and re-organizing these equations leads directly to the rate expressions for molecular nitrogen and oxygen.

$$\begin{aligned} \frac{dc_{N_2}}{dt} &= -\left(\frac{dc_N}{dt} + \frac{m_N}{m_{NO}} \frac{dc_{NO}}{dt} \right) \\ \frac{dc_{O_2}}{dt} &= -\left(\frac{dc_O}{dt} + \frac{m_O}{m_{NO}} \frac{dc_{NO}}{dt} \right) \end{aligned} \quad (2.35)$$

In addition to the rate expressions, the concentrations of N_2 and O_2 need to be expressed as functions of the other species. Taking air as 79% nitrogen and 21% oxygen by number (i.e. $N_N = 0.79N_{NO}$, $N_O = 0.21N_{NO}$) conservation of atomic nuclei yields

$$c_{N_2} = \left[\frac{0.79}{0.79m_N + 0.21m_O} - \frac{c_{NO}}{m_{NO}} \right] m_N - c_N \quad (2.36)$$

$$c_{O_2} = \left[\frac{0.21}{0.79m_N + 0.21m_O} - \frac{c_{NO}}{m_{NO}} \right] m_O - c_O$$

Non-Dimensionalization of Rate Expressions

Non-dimensionalization of the source expressions follows directly from the assumed scaling (Table 1.1). In a mixture with only one reaction, the inviscid species conservation equation in one dimension has the form

$$\frac{\partial c_i}{\partial t} + u \frac{\partial c_i}{\partial x} = \frac{C_f T^\eta}{m_i} \rho ([F] - [B]) = \frac{\dot{W}_i}{\rho} \quad (2.37)$$

in which [F] and [B] are forward and backward (i.e.: dissociation and recombination), dimensionless expression terms, as in Eq. (2.33), and $C = C_f/m_i$ as shown in Ref. (36).

After rescaling this equation with the parameters in Table 1.1, the source term becomes:

$$\dot{W}_i^* = \frac{\Phi [T^\eta \rho^2 ([F] - [B])]^*}{\psi} \quad (2.38)$$

Here, the star denotes non-dimensional quantities and Φ is a non-dimensional rate parameter defined by :

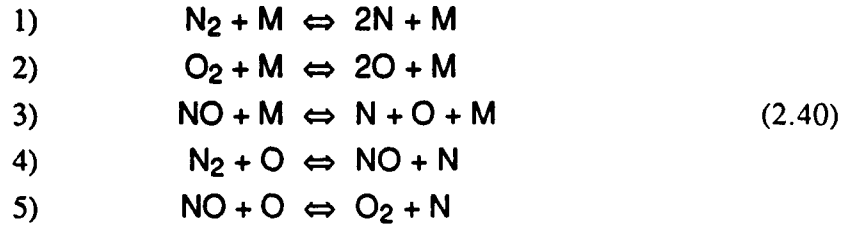
$$\Phi_i \equiv \frac{C_{fi} T_{ref}^{\eta_i} \rho_{ref} L_{ref}}{\bar{m}_i u_{ref}} \quad (2.39)$$

The appearance of \bar{m} in this expression is consistent with the reference mass appearing in the forward and reverse terms. The generalization extends the classical definition of Φ to include systems with multiple, coupled reactions.

2.4 Chemical Source Terms

Reactions Considered

The chemical source terms for any particular species results from the summation of all rate expressions contributing to that species. The primary neutral reactions occurring in air below 9,000 K are:



This system neglects ions of *NO* which may appear at such temperatures in small quantities. These ions, and their associated free electrons, however, contribute primarily to charge separation and electron densities within the shock layer, and are assumed to be of secondary importance in the present study, which therefore includes only the neutral reactions listed above.

Complete Rate Expressions

The rate expression for each reaction makes use of the species production terms of the previous section (e.g. Eq. 2.35). The numerical subscripts on the properties in each of the expressions below refer to the reactions numbered as in (2.40), and the subscript *i* refers to the individual species in the mixture.

$$\begin{aligned}
 R1 &= \frac{\sum_i \Phi_{1i} T^{\eta_{1i}} \rho_i}{2m_1} \left[c_4 e^{-\Theta_{v1}/T} - \frac{\rho}{\rho_{D1}} c_1^2 \right] \rho \\
 R2 &= \frac{\sum_i \Phi_{2i} T^{\eta_{2i}} \rho_i}{2m_2} \left[c_5 e^{-\Theta_{v2}/T} - \frac{\rho}{\rho_{D2}} c_2^2 \right] \rho \\
 R3 &= \frac{\sum_i \Phi_{3i} T^{\eta_{3i}} \rho_i}{m_3} \left[\frac{\rho}{\rho_{D3}} \left(\frac{\bar{m}_3^2}{m_1 m_2} \right) c_1 c_2 - c_3 e^{-\Theta_{v3}/T} \right] \rho
 \end{aligned} \tag{2.41}$$

$$R4 = \frac{\Phi_4 T^{\eta_4} \rho^2 e^{-\Theta_{D4}/T}}{\bar{m}_4} \left[-c_4 c_2 \left(\frac{\bar{m}_4^2}{m_4 m_2} \right) + \frac{1}{K_{c_4}} \left(\frac{\bar{m}_4^2}{m_3 m_1} \right) c_3 c_1 \right]$$

$$R5 = \frac{\Phi_5 T^{\eta_5} \rho^2 e^{-\Theta_{D5}/T}}{\bar{m}_5} \left[-c_5 c_1 \left(\frac{\bar{m}_5^2}{m_5 m_1} \right) + \frac{1}{K_{c_5}} \left(\frac{\bar{m}_5^2}{m_3 m_2} \right) c_3 c_2 \right]$$

These expressions for the non-dimensional rates of each reaction have been written without the starred notation for clarity. Notice that the subscripts on Θ_D and ρ_D refer to properties associated with each reaction and its Arrhenius rate expression. Both of the exchange reactions contain the equilibrium constant K_c . Finally, \bar{m} for each reaction retains its previous definition as the average mass per nucleus of the reactants normalized by the atomic mass of atomic hydrogen.

Source Terms

The source term, \dot{W}_i , for any species follows upon summing the contributions from all reaction rate expressions affecting that species.

$$\begin{aligned} \dot{W}_1 &= \frac{d\rho_1}{dt} = m_1(-2R1 - R3 - R4 - R5) \\ \dot{W}_2 &= \frac{d\rho_2}{dt} = m_2(-2R2 - R3 + R4 + R5) \\ \dot{W}_3 &= \frac{d\rho_3}{dt} = m_3(R3 - R4 + R5) \\ \dot{W}_4 &= \frac{d\rho_4}{dt} = m_4(R1 + R4) \\ \dot{W}_5 &= \frac{d\rho_5}{dt} = m_5(R2 - R5) \end{aligned} \tag{2.42}$$

As mentioned previously, Equation (2.35) eliminates the need for the last two source expressions.

2.5 Rate Constants

Unless specifically noted, all calculations completed for Part III use rate constants and temperature exponents as presented in Reference 30.

II AN ADAPTIVE NUMERICAL METHOD

3. Numerical Integration of Governing Equations

Several levels of embedding removes all structure from a uniform initial mesh. Such unstructured grids do not fit neatly into rectangular matrices and demand unstructured data storage. A numerical integrator for such an environment should operate on a *cell by cell* basis, dependent only upon information contained within a single cell. This effectively rules out most implicit schemes and focuses attention on explicit integration schemes.

This need for a compact computational stencil resulted in the selection of Ni's (29) finite volume formulation of the classic Lax-Wendroff, explicit, time marching scheme. Pervaiz (33) extended this scheme to include chemical source terms in 1987 and Kallinderis and Baron (16) recently formulated a consistent viscous integration extension. The algorithm stores the state vector at cell vertices and integrates each cell independently, requiring only cell-based information, and preserving second-order accuracy at computational nodes.

This chapter briefly describes inviscid integration on 2-D cartesian meshes and includes notes concerning chemical source terms, smoothing, and boundary conditions. For completeness and convenience, Appendix A contains the additional equations for 2-D non-orthogonal curvilinear coordinates (Appendix A-1), axisymmetric non-orthogonal curvilinear coordinates (Appendix A-2), and viscous integration in non-orthogonal 2-D curvilinear coordinates (Appendix A-3).

3.1 Integration in One Dimension

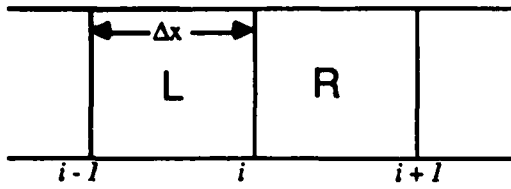


FIGURE 3.1

A one-dimensional computational domain.

Consider the one-dimensional domain of Figure 3.1. The 1-D governing equation system in strong conservation form is

$$U_t = -F_x + W \quad (3.1)$$

and the change at node i occurring after Δt is

$$\delta U_i \equiv U^{n+1} - U^n = \left[U_t \Delta t + U_{tt} \frac{\Delta t^2}{2} + O(\Delta t^3) \right]^n \quad (3.2)$$

Dropping terms of third order and higher and substituting from Equation (3.1) for U_t provides the second-order total change at node i based on contributions at the n^{th} time level.

$$\delta U_i = \Delta t (W - F_x)^n + \frac{\Delta t^2}{2} \{ W_{U(W - F_x)} - [F_U(W - F_x)]_x \}^n \quad (3.3)$$

Equation (3.3) contains the Lax-Wendroff step and evaluates the second derivatives of the state vector using the flux Jacobians W_U and F_U .

$$U_{tt} = W_U U_t - (F_U U_t)_x$$

The first and second terms in (3.3) contain the first- and second-order changes to node i . Ni's primary contribution involved reinterpreting these terms based on cell-centered values of the state, flux and source vectors. To see this, recognize that the source vector at i is

$$W_i \equiv \frac{W_L + W_R}{2} \quad (3.4)$$

Here W_L and W_R represent cell centered values of W . Using central differencing

$$F_x = \frac{F_{i+1} - F_{i-1}}{2\Delta x} = \frac{(F_{i+1} - F_i)}{2\Delta x} + \frac{(F_i - F_{i-1})}{2\Delta x}$$

allows reexpressing the first parenthesis of (3.3) in terms of cell-centered values.

$$\Delta t(W - F_x) = \frac{1}{2}(\Delta U_L + \Delta U_R) \quad (3.5)$$

Here ΔU_L and ΔU_R are the *cell changes* defined by:

$$\begin{aligned} \Delta U_L &\equiv W_L \Delta t - (F_{i-1} - F_i) \frac{\Delta t}{\Delta x} \\ \Delta U_R &\equiv W_R \Delta t - (F_i - F_{i+1}) \frac{\Delta t}{\Delta x} \end{aligned}$$

Similarly, we may recast the second-order term of (3.3) using these cell changes.

$$\frac{\Delta t^2}{2} \{ W_U(W - F_x) - [F_U(W - F_x)]_x \} = \frac{\Delta t}{2} \left\{ \frac{W_U}{2} (\Delta U_L + \Delta U_R) - [F_U(\Delta U_L + \Delta U_R)]_x \right\}$$

Defining the *flux change* and *source change* vectors

$$\begin{aligned} \Delta F_L &\equiv F_U \Delta U_L \\ \Delta W_L &\equiv W_U \Delta U_L \end{aligned}$$

allows the second-order term of (3.3) to be expressed simply as

$$\frac{\Delta t}{2} \left[\frac{\Delta W_L + \Delta W_R}{2} + \frac{\Delta F_L - \Delta F_R}{\Delta x} \right] \quad (3.6)$$

Combining Equations (3.5) and (3.6) to form the total change at i then results in:

$$\delta U_i = \frac{1}{2} \left(\Delta U + \frac{\Delta t}{\Delta x} \Delta F + \frac{\Delta t}{2} \Delta W \right)_L + \frac{1}{2} \left(\Delta U - \frac{\Delta t}{\Delta x} \Delta F + \frac{\Delta t}{2} \Delta W \right)_R \quad (3.7)$$

This form clearly shows the origin of contributions to node i from both adjacent cells. This property makes Ni's scheme very attractive for use with unstructured meshes. Changes to each node may be computed separately for each cell. Then all contributions to any node simply may be summed according to Equation (3.7).

More precisely, with Equation (3.7) written as

$$\delta U_i = \frac{1}{2} (\delta U_{L_i} + \delta U_{R_i}) \quad (3.8)$$

the contributions to i from each cell

$$\begin{aligned}\delta U_{L_i} &= \left(\Delta U + \frac{\Delta t}{\Delta x} \Delta F + \frac{\Delta t}{2} \Delta W \right)_L \\ \delta U_{R_i} &= \left(\Delta U - \frac{\Delta t}{\Delta x} \Delta F + \frac{\Delta t}{2} \Delta W \right)_R\end{aligned}\quad (3.9)$$

may be computed on a cell-by-cell basis. These *distribution formulae* make use of cell center and nodal information only, fulfilling the stated requirement for only cell-based information.

3.2 Ni Scheme in Two Dimensions with Source Terms

In two spatial dimensions, the integration scheme closely resembles the one-dimensional formulation. The governing equations now contain a second flux vector as shown here.

$$U_{tt} = -(F_x + G_y) + W \quad (3.10)$$

An analysis comparable to that of the last section leads to corresponding nodal change formulae and auxiliary equations. On uniform cartesian meshes, like that in Figure 3.2, the change at node i is

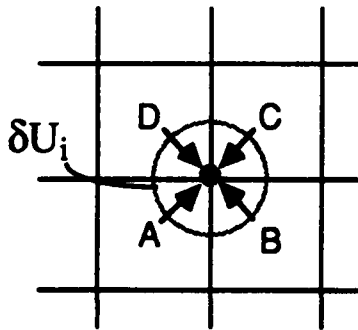


FIGURE 3.2
A two-dimensional computational domain.

$$\delta U_i = \frac{1}{4} \left\{ \begin{aligned} & \left(\Delta U_A + \frac{\Delta t}{\Delta x} \Delta F_A + \frac{\Delta t}{\Delta y} \Delta G_A + \frac{\Delta t}{2} \Delta W_A \right) \\ & + \left(\Delta U_B - \frac{\Delta t}{\Delta x} \Delta F_B + \frac{\Delta t}{\Delta y} \Delta G_B + \frac{\Delta t}{2} \Delta W_B \right) \\ & + \left(\Delta U_C - \frac{\Delta t}{\Delta x} \Delta F_C - \frac{\Delta t}{\Delta y} \Delta G_C + \frac{\Delta t}{2} \Delta W_C \right) \\ & + \left(\Delta U_D + \frac{\Delta t}{\Delta x} \Delta F_D - \frac{\Delta t}{\Delta y} \Delta G_D + \frac{\Delta t}{2} \Delta W_D \right) \end{aligned} \right\} \quad (3.11)$$

where

$$\begin{aligned}\Delta F_c &= F_U \Delta U_c \\ \Delta G_c &= G_U \Delta U_c \\ \Delta W_c &= W_U \Delta U_c\end{aligned}\quad (3.12)$$

Rather than repeat the previous analysis to derive (3.11), we consider an equivalent finite volume approach. This alternate derivation provides greater physical insight into the behavior of the scheme. Here, we intend to examine the 2-D equations, and also show how the distribution formulae assemble the governing equations. The Lax-Wendroff scheme is second order accurate in time and space. Ni's formulation (without dissipation) retains this order of accuracy at the nodes, despite the fact that each cell is computed separately. The advantage of this property cannot be overstressed in the context of the present unstructured solver.

In Equation (3.9) the contribution to each node consists of primary changes from neighboring cells plus or minus secondary corrections for the fluxes through cell boundaries. In terms of a difference stencil at any node, it is clear that each cell on either side of a node performs half of the standard central difference across that node and, when added together at each node, these changes complete the stencil. As a result, in the steady state, ΔU for any particular cell may be non-zero, provided it cancels exactly with the ΔU contribution from its neighbor at the nodes.

In keeping with a cell-based approach, the differential governing equation (3.10) should be replaced by its integral form.

$$\int U_i dA + \int (F_x + G_y) dA = \int W dA$$

The divergence theorem changes the integral of flux vectors into a loop integral over the cell's perimeter.

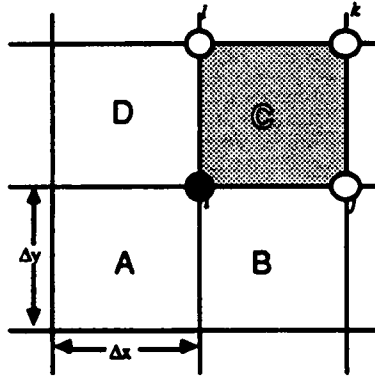
$$\frac{\partial}{\partial t} \int U dA_C + \oint_c (F dy - G dx) = \int W dA_C$$

Letting U and W take on cell-averaged values rids the far left and right terms of their integral signs. For some cell C on the mesh shown in Figure 3.3,

$$U_i + \frac{1}{A_C} \oint (F dy - G dx) = W \quad (3.13)$$

Over a short period of time Δt Equation (3.13) predicts the first order change in C .

$$\Delta U_C = \Delta t W_C - \frac{\Delta t}{A_C} \oint (F dy - G dx)$$



This form displays the nature of the original conservation equations. The first-order change in any cell results from the average contributions of sources within the cell and the flux through its boundaries. Expanding the surface integral using the midpoint rule gives

FIGURE 3.3
A two-dimensional computational domain.

$$\Delta U_C = \Delta t W_C - \frac{\Delta t}{A_C} \left[\begin{aligned} &\left(\frac{F_i + F_l}{2} \right) (y_i - y_l) - \left(\frac{G_j + G_i}{2} \right) (x_j - x_i) \\ &+ \left(\frac{F_k + F_j}{2} \right) (y_k - y_j) - \left(\frac{G_l + G_k}{2} \right) (x_l - x_k) \end{aligned} \right] \quad (3.14)$$

Close examination reveals that this equation reduces exactly to the "cell changes" defined after Equation (3.5). However, the physics exposed by the conservation law of (3.13) offers strong motivation for defining ΔU_C in such a way.

With this in mind, return to the differential Equation (3.10). Substituting the Lax-Wendroff step from (3.2) into (3.10) results in

$$\delta U_i = \Delta U_i^n + \frac{\Delta t}{2} \{ \Delta W_i - [\Delta F_i]_x - [\Delta G_i]_y \}^n \quad (3.15)$$

Here ΔU_i and ΔW_i are cell average quantities for cells A - D (Fig. 3.3)

$$\begin{aligned}\Delta U_i &= \frac{1}{4}(\Delta U_A + \Delta U_B + \Delta U_C + \Delta U_D) \\ \Delta W_i &= \frac{1}{4}(\Delta W_A + \Delta W_B + \Delta W_C + \Delta W_D)\end{aligned}\tag{3.16}$$

and the derivatives of the flux Jacobians are

$$\begin{aligned}[\Delta F]_{ix} &= \frac{1}{2}\left(\frac{\Delta F_B - \Delta F_A}{\Delta x} + \frac{\Delta F_C - \Delta F_D}{\Delta x}\right) \\ [\Delta G]_{ix} &= \frac{1}{2}\left(\frac{\Delta G_B - \Delta G_A}{\Delta x} + \frac{\Delta G_C - \Delta G_D}{\Delta x}\right)\end{aligned}\tag{3.17}$$

Back substituting Equations (3.16) and (3.17) into (3.15) results in

$$\delta U_i = \frac{1}{4} \left\{ \begin{aligned} &\left(\Delta U_A + \frac{\Delta x}{\Delta x} \Delta F_A + \frac{\Delta x}{\Delta y} \Delta G_A + \frac{\Delta x}{2} \Delta W_A \right) \\ &+ \left(\Delta U_B - \frac{\Delta x}{\Delta x} \Delta F_B + \frac{\Delta x}{\Delta y} \Delta G_B + \frac{\Delta x}{2} \Delta W_B \right) \\ &+ \left(\Delta U_C - \frac{\Delta x}{\Delta x} \Delta F_C - \frac{\Delta x}{\Delta y} \Delta G_C + \frac{\Delta x}{2} \Delta W_C \right) \\ &+ \left(\Delta U_D + \frac{\Delta x}{\Delta x} \Delta F_D - \frac{\Delta x}{\Delta y} \Delta G_D + \frac{\Delta x}{2} \Delta W_D \right) \end{aligned} \right\}\tag{3.18}$$

which is exactly Equation (3.11).

Again, we see that each node receives a contribution from surrounding cells to complete the differencing and preserve second-order accuracy at the nodes.

The sketch on the left of Figure 3.4 shows a schematic of the changes accumulated at some node as described by (3.18).

The right side of this same figure presents the same information from a cell-based point of view. Each cell distributes to its nodes and we may rewrite Equation (3.18) from this cell-based perspective, giving the distribution formulae for the 2-D scheme.

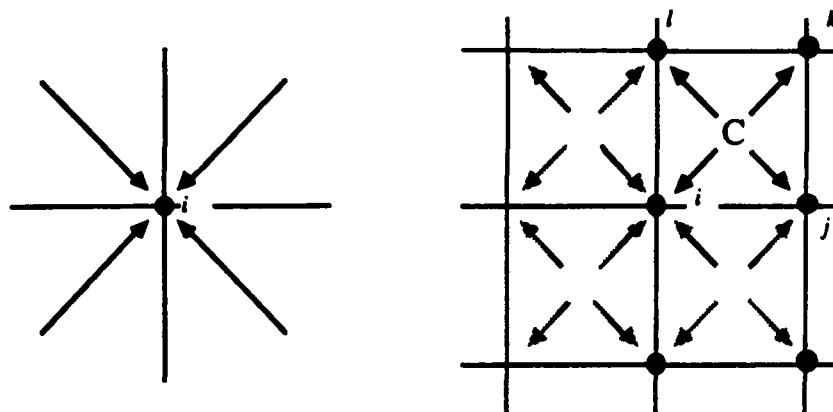


FIGURE 3.4
Schematic of changes accumulated at the i^{th} node in a two-dimensional domain.

$$\begin{aligned}
 \delta U_C)_i &= \frac{1}{4} \left[\Delta U_C - \frac{\Delta t}{\Delta x} \Delta F_C - \frac{\Delta t}{\Delta y} \Delta G_C + \frac{\Delta t}{2} \Delta W_C \right] \\
 \delta U_C)_j &= \frac{1}{4} \left[\Delta U_C + \frac{\Delta t}{\Delta x} \Delta F_C - \frac{\Delta t}{\Delta y} \Delta G_C + \frac{\Delta t}{2} \Delta W_C \right] \\
 \delta U_C)_k &= \frac{1}{4} \left[\Delta U_C + \frac{\Delta t}{\Delta x} \Delta F_C + \frac{\Delta t}{\Delta y} \Delta G_C + \frac{\Delta t}{2} \Delta W_C \right] \\
 \delta U_C)_l &= \frac{1}{4} \left[\Delta U_C - \frac{\Delta t}{\Delta x} \Delta F_C + \frac{\Delta t}{\Delta y} \Delta G_C + \frac{\Delta t}{2} \Delta W_C \right]
 \end{aligned} \tag{3.19}$$

Equation (3.19) implicitly assumes identical time steps for each of the cells. However, for cells of similar size, local time stepping does not present a problem in steady state calculations. The time-accurate work of Pervaiz (33) discusses these points in some detail.

In the preceding discussion ΔF , ΔG , and ΔW involve the product of the Jacobian matrices and changes to the state vector. For finite rate reacting systems, these terms differ from the original perfect gas modeling presented by Ni (29). Appendix B contains these matrices for a calorically perfect gas (B-1), and the multiply-reacting, nonequilibrium gas detailed in the previous section (B-2). For gas models with more elaborate modeling of internal energy modes and energy transfer processes, these matrices may not always exist in analytic form.

3.3 Smoothing Formulation

Although the Euler equations do not include any dissipation, the Lax-Wendroff discrete approximation does. The scheme's truncation error introduces fourth-order terms into the modified PDEs capable of dissipating weak waves. Figure 3.5 displays this property through a plot of the amplification factor of the finite difference Equations (2). While this behavior may provide enough damping to attenuate weak waves, it can be insufficient for the steeper gradients typically found in hypersonic calculations. Additionally, the central differenced algorithm permits odd-even (sawtooth) waves to remain undetected and these waves must be damped.

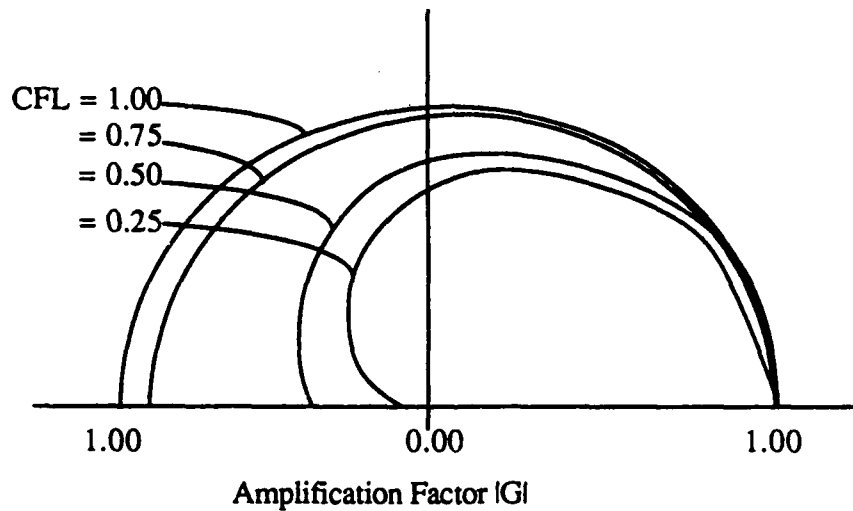


FIGURE 3.5
Amplification factor of the Lax-Wendroff finite difference scheme. (From Ref. 2.)

Smoothing Formulation in One or Two Spatial Dimensions

Referring to the cells in Figure 3.6 and taking σ as the *artificial dissipation coefficient*, the artificial dissipation at node i is

$$D_i = \frac{\sigma}{2} (\delta_{\xi}^2 u) = \frac{\sigma}{2} \left(\frac{u_{i-1} - 2u_i + u_{i+1}}{\Delta \xi} \right)$$

Or, in terms of the average value of the property u in each cell

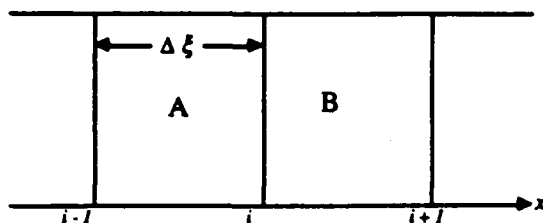


FIGURE 3.6
A one-dimensional computational domain smoothing formulation.

$$D_i = \frac{\sigma}{\Delta\xi} (\bar{u}_A - u_n) + \frac{\sigma}{\Delta\xi} (\bar{u}_B - u_n)$$

This formulation extends easily into two dimensions. Referring to Figure 3.7, the *dissipation vector* at i,j becomes

$$D_{i,j} = \sigma \left(\frac{1}{\Delta\xi} + \frac{1}{\Delta\eta} \right) \left\{ (\bar{U}_A - U_{i,j}) + (\bar{U}_B - U_{i,j}) + (\bar{U}_C - U_{i,j}) + (\bar{U}_D - U_{i,j}) \right\} \quad (3.20)$$

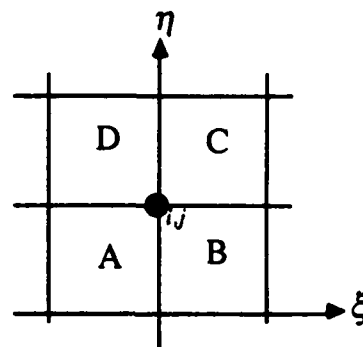


FIGURE 3.7
A two-dimensional computational domain smoothing formulation.

Defining

$$\mu \equiv \sigma \left(\frac{\Delta x}{\Delta\xi} + \frac{\Delta y}{\Delta\eta} \right)$$

and the smoothing contribution to the i th node of any cell C as

$$D_C \equiv \mu (\bar{U}_C - U_i)$$

alters the two-dimensional net change to i (Eq. 3.11) as follows.

$$\delta U_i = \frac{1}{4} \left\{ \begin{aligned} & \left(\Delta U_A + \frac{\Delta x}{\Delta\xi} \Delta F_A + \frac{\Delta y}{\Delta\eta} \Delta G_A + \frac{\Delta x}{2} \Delta W_A + D_A \right) \\ & + \left(\Delta U_B + \frac{\Delta x}{\Delta\xi} \Delta F_B + \frac{\Delta y}{\Delta\eta} \Delta G_B + \frac{\Delta x}{2} \Delta W_B + D_B \right) \\ & + \left(\Delta U_C + \frac{\Delta x}{\Delta\xi} \Delta F_C + \frac{\Delta y}{\Delta\eta} \Delta G_C + \frac{\Delta x}{2} \Delta W_C + D_C \right) \\ & + \left(\Delta U_D + \frac{\Delta x}{\Delta\xi} \Delta F_D + \frac{\Delta y}{\Delta\eta} \Delta G_D + \frac{\Delta x}{2} \Delta W_D + D_D \right) \end{aligned} \right\} \quad (3.21)$$

The shock fit approach removes the bow shock from the domain "interior," and virtually the entire flowfield is smooth by comparison. Nevertheless, the "smooth" region is still strongly nonlinear and requires stabilization throughout. Placing the discontinuity at the boundary of the computational domain effectively removes the need for alternate smoothing levels near and away from discontinuities.

Behavior of Dissipation in Governing Equations

Criticism of smoothing operators stems from the fact that they modify the original set of equations. To assess how the second difference smoothing operator alters the actual system, examine the change at any node i in a one-dimensional domain.

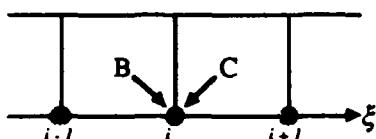


FIGURE 3.8

A one-dimensional computational domain for examining smoothing contributions.

$$\begin{aligned} \delta U_i = & \frac{1}{2} \left\{ \Delta U_B + \frac{\Delta t}{\Delta x} \Delta F_B + \frac{\Delta t}{2} \Delta W_B + \sigma \frac{\Delta t}{2} \left(\frac{u_{i-1} - u_i}{2} \right) \right\} \\ & + \frac{1}{2} \left\{ \Delta U_C - \frac{\Delta t}{\Delta x} \Delta F_C + \frac{\Delta t}{2} \Delta W_C + \sigma \frac{\Delta t}{2} \left(\frac{u_{i+1} - u_i}{2} \right) \right\} \end{aligned} \quad (3.22)$$

This is Equation (3.21) for a single dimension. The first bracket contains the change to i from B and the second contributes the change from C . Decomposing this equation further results in a modified form of the Lax-Wendroff step (Equation 3.3).

$$\delta U_i = \Delta t (W - F_x) + \frac{\Delta t^2}{\Delta x} \{ W_U (W - F_x) - [F_U (W - F_x)]_x \} + \sigma \Delta t (U)_{xx} \quad (3.23)$$

Equations (3.3) and (3.23) differ only by the smoothing term on the extreme right of the latter expression, forcing us to examine the magnitude of the error introduced by this term.

$$\delta U_i = \left[U_i \Delta t + U_{ii} \frac{\Delta t^2}{2} \right]^n + (\sigma \delta^2 U) \Delta t \quad (3.24)$$

Here operator notation has been used to highlight the second difference smoothing. Since the smoothing adds a first-order error to the change at i , σ must be kept small enough to avoid changing the value of the state vector appreciably. Fortunately, in smooth regions, the second

difference of U tends to vanish and the scheme retains its accuracy even for moderate values of σ . Equation (3.24) also predicts the algorithm will contain the largest errors where flow gradients change most rapidly. In practice σ varies from 0.1 to 1.0 for hypersonic calculations and from about 0.02 to 0.1 for transonic and subsonic problems.

Behavior of Smoothing Near Boundaries

The form of Equation (3.22) demonstrates that the overall smoothing contribution to any node results from taking the difference of two first differences. That is

$$(u_{i+1} - u_i) - (u_i - u_{i-1}) = \Delta u_{i+1/2} - \Delta u_{i-1/2} = u_{i-1} - 2u_i + u_{i+1}$$

Each cell contributes one first difference, forming the second difference when the changes from both cells combine at any node.

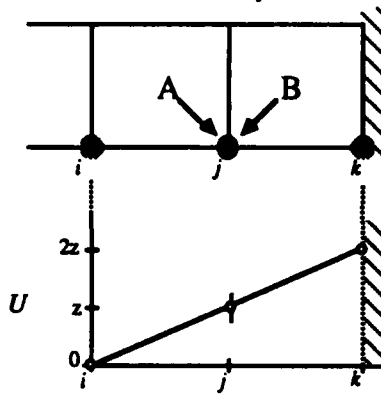


FIGURE 3.9
Variation of property u showing degeneracy of smoothing operator near boundaries.

Consider the special case of a *linearly* varying property u across nodes i, j , to k at the boundary. Since the second difference measures curvature, it should return a zero at any of these nodes. In particular, the smoothing contributions from cells A and B to nodes j and k are:

$$\text{at the interior node } j; \quad D_j = D_A|_j + D_B|_j = \left(\frac{-z}{2} + \frac{z}{2}\right) \frac{\sigma \Delta x}{\Delta x} = 0 \quad (3.25)$$

$$\text{at the boundary node } k; \quad D_k = D_B|_k + 0 = \left(\frac{-z}{2} + 0\right) \frac{\sigma \Delta x}{\Delta x} \neq 0$$

Since the operator detects curvature and the line is straight, zero contributions are expected at both nodes. However, only cell B contributes to the smoothing stencil at k , and a first difference operator results. While the operator behaves correctly on interior points, it degenerates along boundaries. Notice that the first difference operator appears as a direct result of the boundary and is not related to the property variation.

Generalizing, the modified governing equations take the following forms:

$$\begin{aligned}
 &\text{On interior nodes} & U_{ii} + F_{\xi} + G_{\eta} &= W + \sigma(\delta_{\xi}^2 U + \delta_{\eta}^2 U) \\
 &\text{Along } \xi = \text{const. boundary} & U_{ii} + F_{\xi} + G_{\eta} &= W + \sigma(\delta_{\xi}^2 U + \Delta_{\eta} U) \\
 &\text{Along } \eta = \text{const. boundary} & U_{ii} + F_{\xi} + G_{\eta} &= W + \sigma(\Delta_{\xi} U + \delta_{\eta}^2 U)
 \end{aligned} \tag{3.26}$$

Obviously, the first differences along the boundaries will create severe errors in flows with large spatial gradients. However, since the second difference operator measures curvature, it will remain small in such fields - provided the gradients themselves do not change rapidly. Additionally, while the second difference operator is purely dissipative, the first difference behaves convectively, significantly changing the nature of the smoothing terms.

Not smoothing in a direction normal to the boundaries avoids this error. Dropping the first difference terms on the right side of Equation (3.26) results in:

$$\begin{aligned}
 &\text{On interior nodes} & U_{ii} + F_{\xi} + G_{\eta} &= W + \sigma(\delta_{\xi}^2 U + \delta_{\eta}^2 U) \\
 &\text{Along } \xi = \text{Const. boundary} & U_{ii} + F_{\xi} + G_{\eta} &= W + \sigma(\delta_{\xi}^2 U) \\
 &\text{Along } \eta = \text{Const. boundary} & U_{ii} + F_{\xi} + G_{\eta} &= W + \sigma(\delta_{\eta}^2 U)
 \end{aligned} \tag{3.27}$$

Stagnation Enthalpy Smoothing

Writing the equations as in (3.27) shows that the smoothing terms behave like source terms in the governing equations. To minimize changing the physics of the problem, we choose σ to keep such "sources" small.

Without smoothing, the steady-state, inviscid energy equation holds stagnation enthalpy constant. In one dimension

$$\frac{\partial e}{\partial t} + \rho u \frac{\partial (h_o)}{\partial \xi} = 0 \tag{3.28}$$

In the steady state this becomes

$$\rho u \frac{\partial(h_o)}{\partial \xi} = 0 \quad (3.29)$$

Any additional terms violates this adiabatic statement. For a nonequilibrium system, enthalpy is representative of many modes and an altered stagnation enthalpy may lead to unrealistic solutions. For example, if a nonequilibrium mode absorbs only 1% of the total enthalpy, and the error in stagnation enthalpy is 1%, that mode's behavior may be totally incorrect. Although the net effect will be small (only $0.01 h_o$), the outcome may mask the true physics of the problem. Since hypersonic flows are characteristically high enthalpy flows, these observations can have serious implications.

Errors in stagnation enthalpy have other, more subtle, effects. Consider the schematic in Figure 3.10. For a stagnated, frozen, perfect gas, all enthalpy must reside in random particle motion, and constant stagnation enthalpy implies constant stagnation temperature. When the flow enters the shock layer at point b , it very nearly stagnates behind the normal shock. The post-shock temperature at b' jumps to within a few percent of T_o . In slowing isentropically to the stagnation point c , T increases very little. However, this small variation is of primary interest within the shock layer and even a small error in total enthalpy can appear large by comparison.

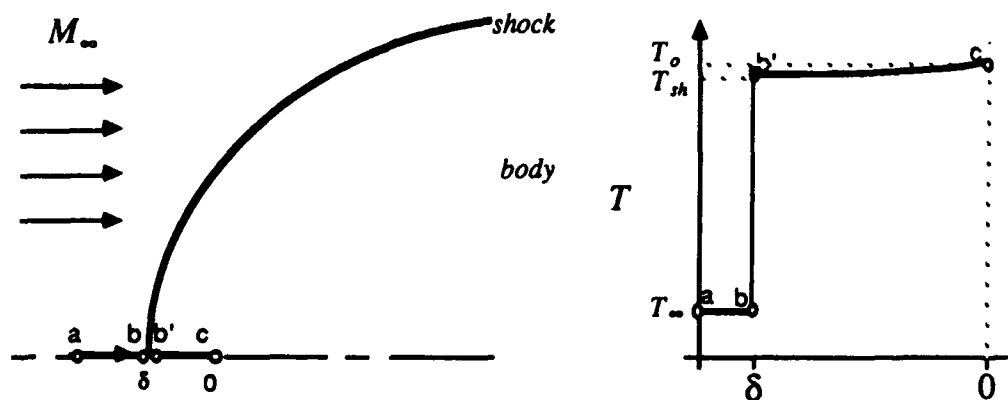


FIGURE 3.10
Stagnation streamline temperature behavior in a frozen flow.

The one-dimensional energy equation with artificial smoothing terms

$$\frac{\partial e}{\partial t} + \frac{\partial(\rho u h_o)}{\partial \xi} = \sigma(\delta^2 e) \quad (3.30)$$

no longer implies constant h_o . Instead, the balance forces total enthalpy to vary in space in accord with the non-linearity of the total internal energy. The term is small but the preceding discussion indicates the possible consequences. In practice, a σ level of 0.1 has a noticeable effect on h_o in the domain downstream of the shock.

To prevent this, a second smoothing term $D_{h_o}_i$ adds a correction to the internal energy at i to counteract the error produced in (3.30). This correction forces h_{oi} toward $h_{o\infty}$, tending to hold h_o constant throughout the domain. Specifically,

$$D_{h_o}_i = \frac{\mu_{h_o}(h_{o\infty} - h_{oi})e_i}{h_{o\infty}} \quad (3.31)$$

Here the subscript i denotes local quantities, μ_{h_o} is a *stagnation enthalpy smoothing coefficient* and the ratio $e_i/h_{o\infty}$ rescales the term for use in the energy equation. If $h_o = \text{const} = h_{o\infty}$ this correction vanishes. In other words, the term contributes only if the standard second difference smoothing violates the physics expressed by the energy equation. Adding this term to the energy equation (only) results in the following change in total internal energy at any node i .

$$\delta U_i = \frac{1}{4} \left\{ \begin{aligned} &\left(\Delta U_A + \frac{\Delta x}{\Delta x} \Delta F_A + \frac{\Delta x}{\Delta y} \Delta G_A + \frac{\Delta x}{2} \Delta W_A + D_A + D_{h_o}_i \right) \\ &+ \left(\Delta U_B - \frac{\Delta x}{\Delta x} \Delta F_B + \frac{\Delta x}{\Delta y} \Delta G_B + \frac{\Delta x}{2} \Delta W_B + D_B + D_{h_o}_i \right) \\ &+ \left(\Delta U_C - \frac{\Delta x}{\Delta x} \Delta F_C - \frac{\Delta x}{\Delta y} \Delta G_C + \frac{\Delta x}{2} \Delta W_C + D_C + D_{h_o}_i \right) \\ &+ \left(\Delta U_D + \frac{\Delta x}{\Delta x} \Delta F_D - \frac{\Delta x}{\Delta y} \Delta G_D + \frac{\Delta x}{2} \Delta W_D + D_D + D_{h_o}_i \right) \end{aligned} \right\} \quad (3.32)$$

In practice a value of μ_{h_o} two to three times larger than the overall smoothing coefficient μ suppresses total enthalpy variations to 0.1% or less. Use of such a large coefficient seems reasonable since the term tends to restore the physics of the original governing equations.

As a final comment on stagnation enthalpy smoothing, note that smoothing terms affect all of the conservation equations. At any point in the field they effectively create mass sources, momentum sources, etc.. Reference 7 shows that the second difference operator is globally conservative for constant smoothing coefficients. Since the other conservation statements (mass, momentum, species) are integral properties, the local sources and sinks globally cancel due to the conservative nature of this smoothing formulation. On the other hand, stagnation enthalpy is a point property, and while overall energy may be conserved, any source term will be incorrect at a particular point.

3.4 Numerical and Physical Boundary Conditions

A typical hypersonic shock layer maps from physical to computational space as shown below (Figure 3.11). All flow in the domain passes through the shock (\overline{ad}) and, in the steady state, must be balanced by the out flow across the shock layer (\overline{cd}). When the gas is assumed inviscid, it slips tangentially over the body's surface.

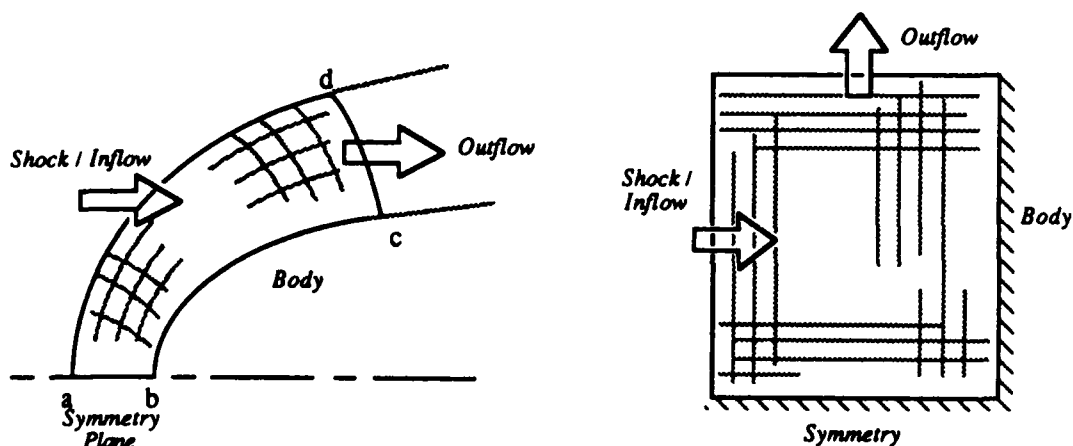


FIGURE 3.11
Schematic of physical and computational space for blunt body computations.

For symmetric two-dimensional problems, the natural symmetry plane allows calculation of only half the domain. In the axisymmetric case, the stagnation streamline becomes the axis of symmetry, again permitting this simplification.

Edge Cells in Finite Volume Schemes

Figure 3.11 contains four types of boundaries surrounding the computational mesh, and all boundary nodes have physical cells on only one side. For cell vertex based schemes this results in incomplete differencing across such nodes.

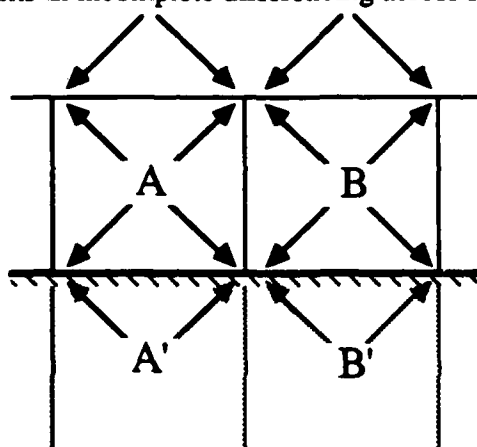


FIGURE 3.12
Edge cells in a node-based finite-volume scheme.

Consider the boundary cells A and B in the sketch shown to the left (Figure 3.12). The nodes i , j , and k receive corrections δA and δB from one side only. In other words, boundary nodes, such as these, receive only two corrections, while interior nodes receive four.

From a finite difference standpoint, the spatial derivatives make use of a central difference operator at all computational nodes. Normal to boundaries, this operator becomes one-sided and requires special treatment.

To prevent this degeneracy, imagine a second set of cells A' and B' outside the physical boundary. These fictitious cells complete the central difference taken normal to the boundary and permit upgrading of these nodes. In this figure, cells A' and B' contribute a change $\delta A'$ and $\delta B'$ to j providing it with a total of four changes - just like an interior node. In the event no better estimate exists, setting $\delta A'$ and $\delta B'$ equal to δA and δB results in first order accuracy (since this is equivalent to a forward or backward difference).

Implementing this general treatment requires simply doubling the changes to each boundary node. Each of the boundaries shown in Figure 3.11 presents a physical situation which permits modification of this procedure to improve the accuracy of this procedure based on knowledge of the physical boundary.

Inflow / Shock Boundary

The bow shock forms the inflow boundary of the domain. This confines the domain to points within the shock layer and avoids introducing undisturbed cells. Chapter 5 describes the shock fitting procedure in some detail.

Symmetry Plane Boundary

The symmetry plane presents precisely the situation shown in 3.13. The imaginary cells A' and B' are simply mirror images of A and B . The boundary conditions for such nodes is clear. Using the notation of Figure 3.12, the change at node j is:

$$\delta U_j = 2\delta U_A)_j + 2\delta U_B)_j \quad (3.34)$$

Since it is also a streamline of the flow, the normal velocity vanishes identically. This recognizes no flow across the boundary and prevents the growth of spurious error and sawtooth oscillations.

Outflow Boundary

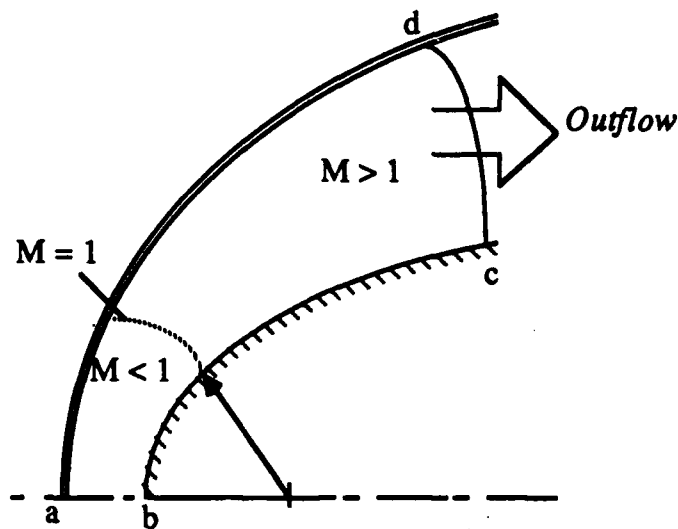


FIGURE 3.13
Schematic of outflow boundary in blunt body flow showing location of the sonic line.

Doubling the changes for the exit plane results in only first order accuracy across the downstream boundary. However, for most configurations, the supersonic flow across this plane does not permit the error to propagate upstream and corrupt the rest of the domain.

Solid Wall Boundary

Inviscid flow slips tangentially along the wall following the local surface inclination and the body surface streamline. For low enthalpy flows, this boundary condition is easily implemented. At each time step, one computes the total velocity at a body node, discarding the normal components. Alternatively, when integrating the cells along the solid wall boundary, one may enforce a *no-flux* condition along the body surface. This prevents the face from contributing to the flux integral. These simple treatments usually perform adequately. However, the high-enthalpy flows presently under consideration require greater care.

In these flows - especially near the stagnation region - these treatments may lead to strong transients during convergence, or extreme sensitivity to initial conditions. In reacting flows, or gas models with multiple internal energy modes, any error in stagnation enthalpy may lead to

non-physical solutions. Clearly, discarding the normal velocity component throws away energy. To avoid such enthalpy errors, it is better to reorient the velocity vector at each node.

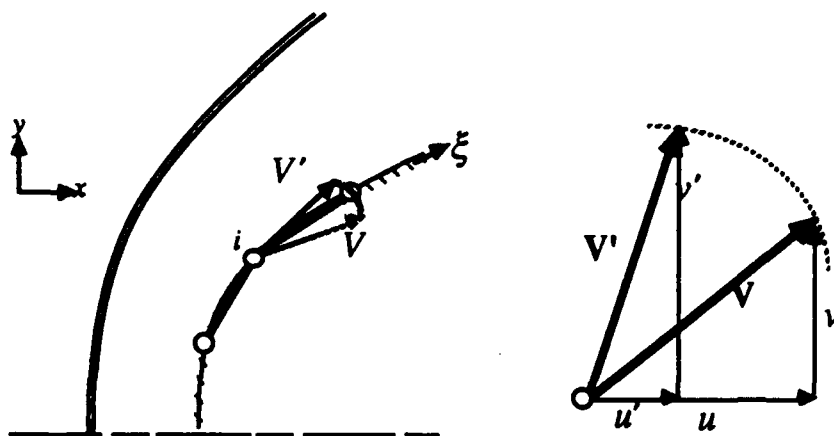


FIGURE 3.14
Flow tangency condition for inviscid simulations showing reorientation of the total velocity vector.

The velocity vector \mathbf{V} consists of the current (time n) values of velocity plus changes to this vector $\delta\mathbf{V}$. After first computing this quantity at some surface node i ,

$$|\mathbf{V}_i| = \sqrt{\tilde{u}_i^2 + \tilde{v}_i^2} \quad (3.35)$$

with x and y components

$$\tilde{u}_i^2 = u_i^n + 2\delta u_i$$

$$\tilde{v}_i^2 = v_i^n + 2\delta v_i$$

rotate this vector to the local surface slope inclination angle to preserve translational energy.

$$\begin{aligned} u_i' &= \tilde{u}_i \frac{\partial x}{\partial \xi} \frac{\partial x}{\partial \xi} + \tilde{v}_i \frac{\partial y}{\partial \xi} \frac{\partial x}{\partial \xi} \\ v_i' &= \tilde{u}_i \frac{\partial y}{\partial \xi} \frac{\partial x}{\partial \xi} + \tilde{v}_i \frac{\partial y}{\partial \xi} \frac{\partial y}{\partial \xi} \end{aligned} \quad (3.36)$$

Finally, rescale the resulting vector to the same overall magnitude of the original velocity vector.

$$\begin{aligned} u_i &= u_i' \frac{|\mathbf{V}_i|}{\sqrt{\tilde{u}_i^2 + \tilde{v}_i^2}} \\ v_i &= v_i' \frac{|\mathbf{V}_i|}{\sqrt{\tilde{u}_i^2 + \tilde{v}_i^2}} \end{aligned} \quad (3.37)$$

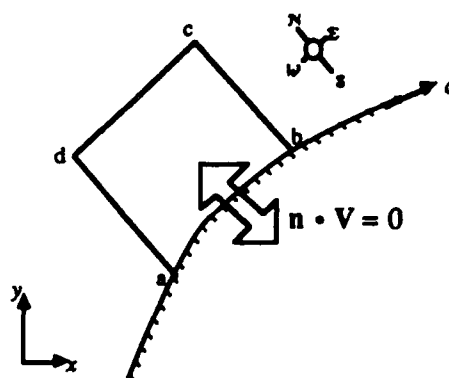
At first glance, forcing the velocity vectors tangential at each body node may appear equivalent to enforcing the no-flux condition on the surface. The nodal velocity will convect members of the state vector parallel to the surface preventing these fluxes from contributing to the integral performed upon each cell.

Certainly this is the case for both linear and parabolic bodies, but, upon more generally shaped bodies, flow tangency at surface nodes may not entirely prevent contributions to the flux integral. The cell's wall may not necessarily be at the same (algebraic mean) slope of the corner nodes. While this is a higher order error, experience suggests that not enforcing a no-flux boundary may degrade the initial convergence properties of the scheme.

Examine the integral expression for the changes to cell C .

$$\Delta U)_C = \Delta t W_C - \frac{\Delta t}{A_C} \oint F dy - G dx \quad (3.38)$$

The contribution to the loop integral over the south face is:



$$F \Delta y_s - G \Delta x_s = \begin{bmatrix} \rho u \\ \rho u^2 + p \\ \rho uv \\ u(\rho e + p) \\ \rho u \end{bmatrix} \Delta y_s - \begin{bmatrix} \rho v \\ \rho uv \\ \rho v^2 + p \\ v(\rho e + p) \\ \rho v \end{bmatrix} \Delta x_s \quad (3.39)$$

FIGURE 3.15
No contribution to flux integral from surface face.

Re-arranging yields

$$F\Delta y_s - G\Delta x_s = \begin{bmatrix} \rho \\ \rho u \\ \rho v \\ \rho h_s \\ \rho \end{bmatrix} (u\Delta y_s - v\Delta x_s) + \begin{bmatrix} 0 \\ p\Delta y_s \\ -p\Delta x_s \\ 0 \\ 0 \end{bmatrix} \quad (3.40)$$

But, no-flux implies $\mathbf{n} \cdot \mathbf{V} = 0$ through the southern face.

$$\mathbf{n} \cdot \mathbf{V} = -\frac{(u\Delta y_s - v\Delta x_s)}{\Delta \xi} = 0$$

So, $u\Delta y_s - v\Delta x_s = 0 \quad (3.41)$

Equation (3.41) forces the entire first term on the right of (3.40) to zero leaving only the pressure forces in the second and third elements of the flux integral to contribute to the integral.

$$F\Delta y_s - G\Delta x_s = \begin{bmatrix} 0 \\ p\Delta y_s \\ -p\Delta x_s \\ 0 \\ 0 \end{bmatrix} \quad (3.42)$$

Applying Equation (3.42) during the integration step, reorienting the velocity vector by (3.37), and doubling the changes to the other members of the state vector by (3.37) insures correct boundary treatments and avoids most problems with initial transients.

4. Adaptation and Unstructured Meshes

The discrete equations only approximate the governing equations of inviscid, reacting, supersonic flow. The Lax-Wendroff integration scheme neglects terms of third order and above in both space and time. As a result, it may become necessary to increase the quality of any given solution by increasing the grid's spatial resolution. However, since smooth and slowly varying regions of the flow field contain little third order activity, refinement in those areas adds little to the global accuracy of the solution. In more steeply varying regions, however, the linear and second order terms in the FDE's do not permit adequate flexibility to resolve the physics of compressible flows. As discussed previously, this situation results in the largest numerical errors where the flow gradients vary the fastest. Unfortunately, it is precisely such physical structures which often dominate a flow's behavior.

Grid adaptation attempts to resolve this disparity by either re-distributing or embedding nodes to improve resolution of flow features. References 9, 35, and 7 contain discussions comparing the relative merits of both approaches.

Originally developed by Dannenhoffer and Baron (6), the technique described here refines a solution by embedding finer grids in response to flow features detected on coarser grids. While this method reliably detects these features, its real strength is the ability to embed several grid levels in arbitrarily shaped regions during evolution of a solution.

In a hypersonic shock layer, one expects large species gradients after a chemically excited flow passes through a strong bow shock. In order to resolve these gradients, the chemical relaxation length cannot be much smaller than about one percent of a local cell dimension. This effect also was documented by Park (30) who described it in terms of the mesh Damköhler number. Such *near equilibrium* flows present significant computational difficulties due to the small length scales. Although it is tempting to consider identical equilibrium modeling, the rapidly varying chemical relaxation length demands a nonequilibrium calculation as the flow continues through the shock layer. Dissociation, for example, absorbs much of the flow's energy and may change the chemical length scale by several orders of magnitude. In addition to providing greater resolution of the relaxation zone, grid adaptation helps to resolve behavior near internal shocks, expansion fans, sliplines etc..

Note that the bow shock forms the inflow boundary and the domain contains no freestream cells. All computational cells lie in "disturbed" regions and contribute to the solution. Thus, shock fitting performs a somewhat similar function as adaptation. Moreover, since the blunt body domain is narrowest near the stagnation point, the shock layer shape automatically clusters nodes near the nose during the initial grid generation phase. As a result we expect a reasonably applicable coarse mesh, and the adaptation serves to tailor the grid by further refining structures within the shock layer.

4.1 General Procedure

Adaptation greatly increases the quality of a given solution with modest additional computational effort. The results published by Baron, Dannenhoffer, Kallinderis, Pervaiz and Shapiro (6, 17, 33, and 34) demonstrate this quite clearly. Often, equally resolved solutions

without embedding must use globally fine grids and are too expensive to compute, even to benchmark a particular solution.

This added efficiency comes at the expense of coding effort. To some degree, the perceived complexity of coding an unstructured, adaptive domain prevents the widespread use of adaptive techniques. Here we describe a simple (but effective) adaptive algorithm. Additionally, the final Section (4.5) stresses the ease of implementing adaptation routines in a reasonably efficient manner.

The basic algorithm contains three steps:

- i. Detection:* Examination of the flowfield in search of flow features.
- ii. Division:* Dividing large cells into smaller cells to create new cells and nodes.
- iii. Pointer Updating:* Absorption of new cells and nodes into the existing data structure

While the procedure described here is similar to that presented by Dannenhoffer (6) and the spatial adaptation by Pervaiz (33), the implementation is believed to be less complex than either. As a result it lacks some of the subtler features of these previous works. Nevertheless, it works well in practice.

4.2 Detection of Flow Features

Detecting features in a flowfield typically requires consideration of threshold values, differences in computational space, and independent detection parameters. The suggested scheme examines one or more independent properties throughout the domain and evaluates either first or second differences. Then, after normalizing by a convenient rule, the algorithm tags cells containing differences above a certain threshold for refinement.

Feature detection is not a unique procedure, and while it is relatively simple to design a system capable of trapping some given feature, designing a detector to trap all interesting or important features is a much more difficult task. It is difficult to precisely define "interesting or important." More importantly, most flow features do not have clearly defined "edges," making threshold selection somewhat arbitrary.

Figure 4.1 indicates some of the expected flowfield structures. These features result from both fluid dynamic and thermo-chemical phenomena and all exist to varying degrees in most hypersonic flows. The inviscid Euler equations predict the entropy layer and expansion fan in supersonic blunt body flows for gases with and without internal degrees of freedom. The nonequilibrium features arise as a direct result of a real gas incorporating into the governing equations.

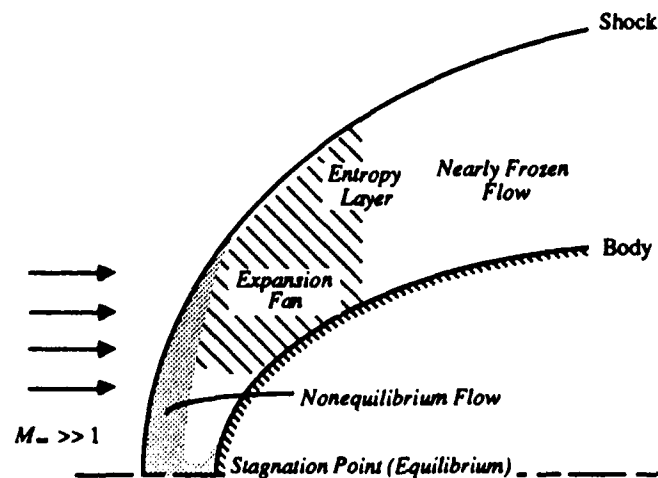


FIGURE 4.1
Some flow features in hypersonic, real-gas, blunt body flows.

Selection of Flowfield Indicators

In order to separate the gas dynamic and chemical features, we search for flow variables which respond independently to fluid and nonequilibrium chemical structures. As an element of gas flows through an expansion fan e.g., p , T and ρ all decrease monotonically. The smooth behavior implies small second differences, indicating the benefits of first differences for detection. First differences furnish a *slope per cell*. Over a typical blunt wedge, p , T and ρ tend to be constant in both the stagnation region and along the flat body surface downstream of the expansion fan, and differences for any one of the variables will correctly identify the feature. T and ρ respond much the same to an entropy layer and either of those properties would identify this feature. Reference 7 lists several gas dynamic features and evaluates criteria for locating specific structures.

For the features in Figure 4.1 the choice of a best parameter to identify the fluid dynamic structures is not crucial. Density was chosen since it is a state variable and mass must be conserved. Moreover, since it is a primitive variable, integration yields a direct value without auxiliary equations. As a result it is less prone to spurious errors than are calculated quantities like pressure or temperature.

The choice of nonequilibrium parameters depends largely upon the internal modes included in the gas model. In general, these modes act independently and on different physical scales, and each requires its own independent parameter. For dissociating and vibrating gas models, both species concentrations and vibrational temperature should be considered as independent parameters. For cases where all nonequilibrium modes are chemical, the reaction rates associated with production of different species vary greatly and result in different reactions occurring in various parts of the domain. For such flows, differences in all independent species indicate chemical behavior along the various reaction paths.

Of course, the most important criteria that a flowfield indicator must satisfy is independence. Since pressure, temperature, and density all respond to an expansion fan, any one of them would identify the feature. Interrogating more than one is unnecessarily expensive. However, through that same expansion fan, the chemistry will often tend to freeze out and display little variation. Since it responds to an entirely different class of flow feature, species concentration behaves as an *independent parameter*.

Since cells spanned by large differences (in computational space) divide as the adaptive process continues, the procedure drives the solution toward uniform differences in computational space. Embedding *smooths out variations in computational space*. The first and second order terms preserved by the Lax-Wendroff differencing permit tracking of the governing equations up to the second derivatives. This smoother domain, with its smaller higher order derivatives lends itself to more accurate computation of the state vector.

The Mechanics of Detection

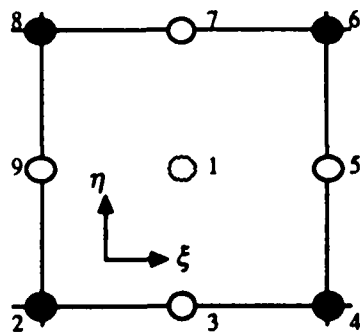


FIGURE 4.2
General undivided cell.

For a general cell considered by a feature detector, corner nodes 2, 4, 6 and 8 always exist. The midface nodes 3, 5, 7, and 9 may exist if any adjacent cells are already divided.

The difference in the ξ direction is

$$\begin{bmatrix} \delta_{\xi} \rho \\ \delta_{\xi} c_i \end{bmatrix} = \begin{bmatrix} \rho \\ c_i \end{bmatrix}_5 - \begin{bmatrix} \rho \\ c_i \end{bmatrix}_9$$

where ρ is density and c_i is a nonequilibrium parameter (i.e. mass fraction of the i^{th} species).

Similarly the difference in η is

$$\begin{bmatrix} \delta_{\eta} \rho \\ \delta_{\eta} c_i \end{bmatrix} = \begin{bmatrix} \rho \\ c_i \end{bmatrix}_7 - \begin{bmatrix} \rho \\ c_i \end{bmatrix}_3$$

A rational definition gives the overall change in any cell; e.g.

$$\begin{aligned}\Delta\rho &\equiv \sqrt{(\delta_\xi\rho)^2 + (\delta_\eta\rho)^2} \\ \Delta c_i &\equiv \sqrt{(\delta_\xi c_i)^2 + (\delta_\eta c_i)^2}\end{aligned}\tag{4.1}$$

These definitions could easily be biased toward ξ or η by altering the exponents under the radicals.

The magnitudes of the differences are important primarily for comparison with other differences, and should be normalized. Popular choices for reference levels include the statistical mean, mode, or maximum value. Choosing the maximum value, $\Delta\rho_{\max}$ and $\Delta c_{i\max}$, conveniently bounds the variation of flowfield indices between zero and one. Obviously, the reference choice is not unique and most parameters work equally well.

Adaptation Maps and Thresholds

After computing the refinement parameters for each cell, it is helpful to prepare a map as shown (Fig. 4.3). (The magnitudes implied by the positive branch of the radical in Equation (4.1) actually collapse the map to the 1st quadrant.) This example shows a map for two parameters. In general, such maps contain as many dimensions as there are adaptation parameters.

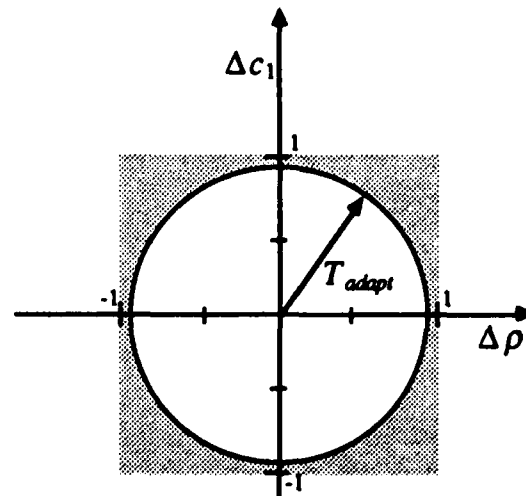


FIGURE 4.3
An adaptation map based on two parameters.

Cells containing little or no variation will cluster near the origin, while cells within or near features plot further from the origin. Since the two parameters should be independent, we anticipate little activity along the 45° diagonal $\Delta c_i = \Delta\rho$. Clustering along such a line would indicate a feature being tracked by both parameters, and thus parameters which do not respond independently.

The *adaptation parameter* measures the distance from the origin to any point on the map,

$$AC = \sqrt{(\Delta\rho)^2 + (\Delta c_i)^2} \quad (4.2)$$

and the scheme marks a cell for division whenever AC is greater than some threshold, T_{adapt} .

For n adaptation parameters, AC becomes a radius in n dimensional space, and Eq.(4.2) generalizes to

$$AC = \sqrt{(\Delta\rho)^2 + \sum_i (\Delta c_i)^2} \quad (4.3)$$

Again, adjusting the exponents under the radical weights any parameter accordingly.

Figure 4.4 presents an example of an actual adaptation map computed for a relatively low enthalpy Mach 5 flow with a simple dissociation reaction ($A_2 + M \rightleftharpoons 2A + M$) and illustrates many of the features discussed above.

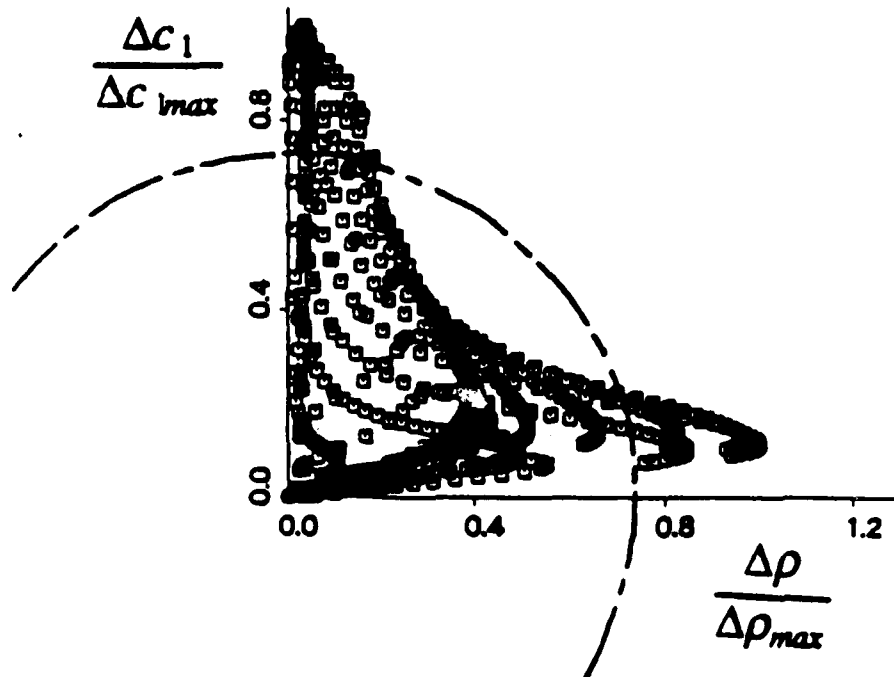


FIGURE 4.4
Adaptation map for Mach 5 flow showing polarization.

Since the plot exhibits considerable scatter, it is fair to say that differences in various regions remained relatively benign with respect to one another. More precisely, the chemical

and density gradients are distributed relatively evenly throughout the field and not confined to a few isolated regions. Since nearly all cells have some species and density variation, it is clear that the reactions in the domain did not occur over scales very disparate from the physical scale of the body. For example, the dissociative activity did not occur solely adjacent to the shock.

The *polarization* of these data demonstrate that atom mass fraction and density are responding independently as intended. This polarization cannot be overstressed and demonstrates that each of the adaptive indices responds (independently) to its own type of flow features.

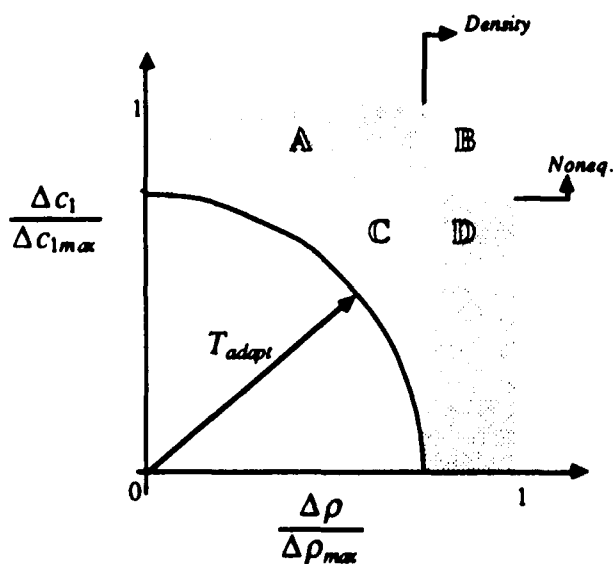


FIGURE 4.5
Behavior of a general adaptation map.

chemical activity. As the flow expands out of a stagnation region and around a body, the density drops rapidly, making it difficult for various reactants to locate collision partners and effectively turning off the chemistry. Indicative of rapid variation in both parameters, region *B* contains few cells in practice. However, if the fluid dynamical parameters depend strongly on the degree of nonequilibrium, cells may appear here. This often occurs in gases such as nitrogen where the dissociation energy may comprise a significant portion of the flow's total enthalpy. Chapter 7 details these effects more thoroughly. Finally, region *C* contains cells which

Figure 4.5 examines this behavior in more detail. Here a mock adaptation map shows all cells having $AC \geq 0.75$ tagged for division. Cells in region *A* demonstrate such extreme nonequilibrium that they will be adapted regardless of their density behavior. Typically, cells in this area lie in rapidly relaxing flow regions. Conversely, cells in *D* show large density differences, but little

adapt due to contributions from all indices. Note that an actual map (e.g. Fig. 4.4) contains no cells in either region *B* or *C*.

To address the question of which cells adapt due to which parameters, consider the Fig 4.6 sequence below.

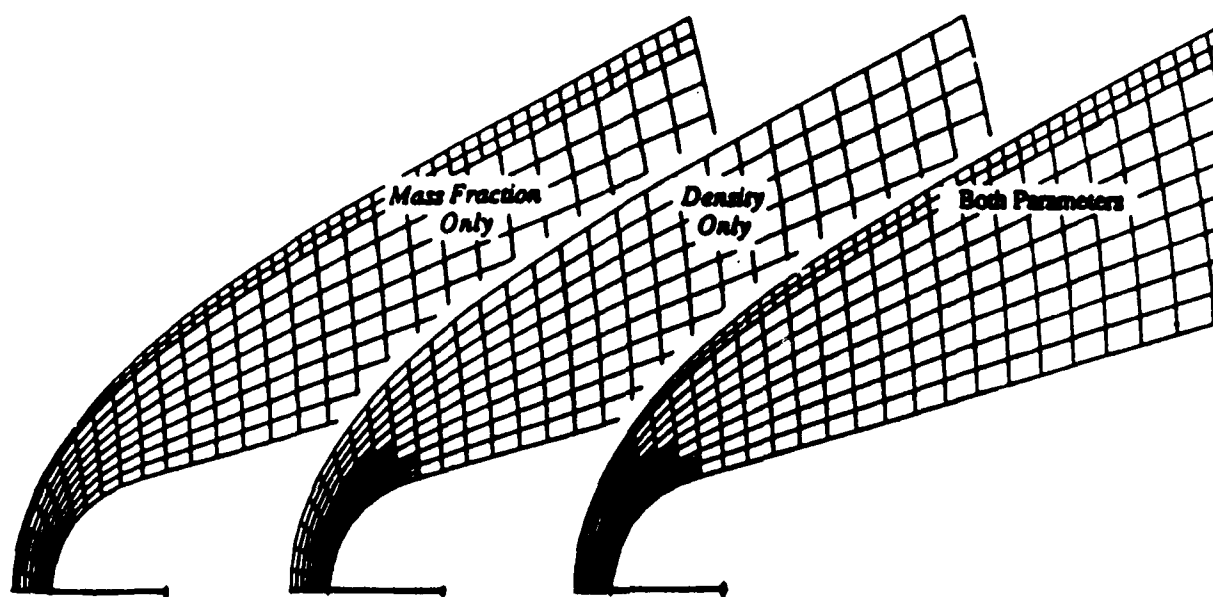


FIGURE 4.6
Adaptation based on different parameters

These figures contain grids for hot nitrogen flowing at Mach 5.66 over a blunt wedge. Since the freestream is 2390 K, considerable chemical activity occurs. Using ρ as an adaptive index captures the expansion fan and developing entropy layer, while concentration differences identify the chemical relaxation. Due to the strong coupling as the flow tends toward equilibrium at the stagnation point, both indices define this region.

Threshold Selection

Often great debate surrounds the topic of what constitutes a "feature." This may result in elaborate schemes for threshold selection (see for example (7) and (33)). In practice, however,

the question is not critical and a relatively broad range will adequately capture flow physics. Different thresholds adapt different numbers of cells, but both can capture the feature reasonably well and small changes in "good" threshold value should not radically alter the adaptation pattern.

As an example, increasing or decreasing T_{adapt} by 10% from the 0.75 level in Figure 4.4 would have little effect on the ultimate number of cells divided. However, if located within the "crotch" in the map, slight changes in value would produce large changes in the size of adapted regions. In fact, were T_{adapt} reduced to below about 0.4, the arc would cut arbitrarily through the data based on meaninglessly small differences in adaptive indices. The resulting embedded grid would suffer not only from ragged interface patterns but also from problems with islands and voids. Threshold values for shock fit problems typically range from 0.6 - 0.7 since the shock fitting has eliminated freestream cells, while those for approaches that include freestream cells are smaller by approximately a factor of two.

Figure 4.7 traces an adaptive sequence on a Mach 12 flow over a blunt wedge in air at an altitude of 45 km. Oxygen dissociates noticeably but the stagnation enthalpy is insufficient to dissociate appreciable amounts of nitrogen. These maps plot normalized differences in oxygen mass fraction against normalized density differences. For this 2-D example, the body size is such that the reaction completely relaxes in about 1% of the nose radius, producing very stiff, near equilibrium, behavior near the shock.

The first part of the sequence (4.7a) shows the adaptation map for the original grid on the left and the adaptation resulting from $T_{\text{adapt}} = 0.65$ on the right. Since the chemical behavior is severe, only 1 row of cells extends along the vertical axis, these cells corresponding to the string of data extending vertically on the map. Additionally, the scheme adapts cells containing large density differences. By removing the extremum, this process effectively spreads out the remaining pile of cells. After re-converging the solution two orders of magnitude, the adapta-

tion map of 4.7b is essentially a close-up of the original map and reexamines the field after one level of embedding. Notice that the shock cells still span the largest chemical gradients – i.e.

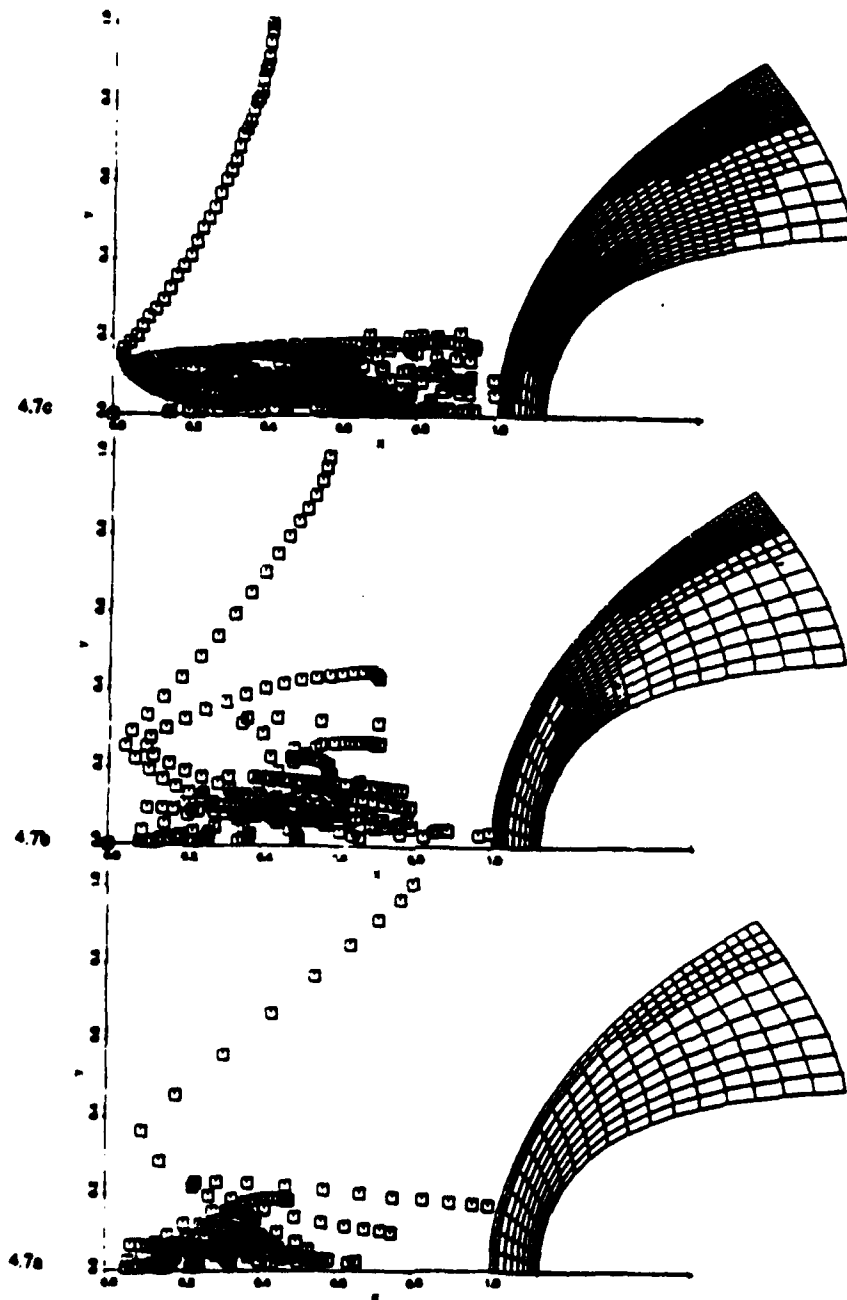


Figure 4.7
Adaptive sequence on a blunt nose.

the reaction is still buried within this first set of cells. The differences in density, however, exhibit more scatter, are more evenly distributed across the abscissa, and a few cells still

contain large differences. Subdividing this map with the same 0.65 threshold value results in the grid to the right. Here we see two levels of embedding indicating the relaxation zone, entropy layer and expansion fan.

Figure 4.7c depicts the map after converging on the doubly embedded grid. The cells are now evenly distributed across the abscissa and none still contain extreme density differences, demonstrating that the density varies smoothly in computational space. Only one line of cells still contains severe chemical behavior, indicating that the majority of the relaxation still spans only one cell. Notice, however, that this string of cells demonstrates little variation in density. The adaptive process has separated the adaptive indices.

The last two plots (Figure 4.7c) show the adaptive map after a third adaptation. Here the abscissa is completely diffuse and only shock cells contain large chemical gradients. Examining the actual chemical behavior, we see that despite these large differences across the first cell, the grid completely captures the chemical relaxation. Moreover, the initial linear decay contains little if any third order truncation error making further adaption pointless (and expensive).

4.3 Unstructured Grids

The mechanics of adaptation revolve around the use of *unstructured grids*. The addition of adaptation to any unstructured solver is usually straightforward. An unstructured grid should not be considered a 2-D net of cells, or even as nodes with typical i, j addresses. Instead the grid is simply a collection of cells with some explicitly defined "connectivity" relating the cells to the physical domain.

An unstructured solver operates on each cell independently. This fact alone rules out most implicit integration algorithms. Ni's (29) scheme works well because the calculation proceeds on a cell by cell basis and still provides second order spatial accuracy at the *nodes*. Moreover, the line integration is quite tolerant of misshapen cells and retains its accuracy for reasonably large degrees of skewing and stretching (7).

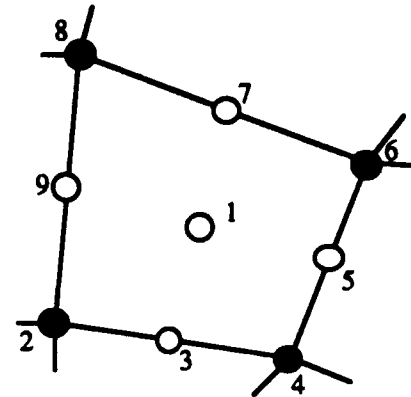


FIGURE 4.8
General cell in unstructured domain.

Applying the integration scheme of the last chapter to the cell in Figure 4.8 requires:

- i. Geometrical information describing size, shape, etc..
- ii. The ability to locate neighboring cells for any node
- iii. Knowledge of nodes which define the cell's boundaries.

Each node receives a unique *node number* in lieu of a more typical i, j address permitting a two element *geometrical pointer* to locate each node in physical space.

GEOM(1, node number) = 1st coordinate in physical space

GEOM(2, node number) = 2nd coordinate in physical space

Since the calculation proceeds cell-by-cell, we need to determine which cells surround any node. The *neighbor pointer* contains four elements for each node

NEIB(1, node number) = SW cell number

NEIB(2, node number) = SE cell number

NEIB(3, node number) = NE cell number

NEIB(4, node number) = NW cell number

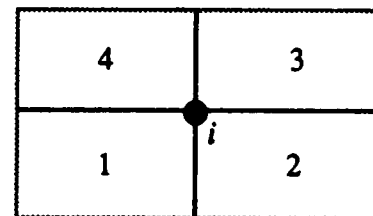


FIGURE 4.9
Cell numbers surrounding a node.

If the node is along a boundary, certain cells may not exist and this pointer receives a zero value.

Once inside any cell, the *cell pointer* locates the nine nodes defining its boundaries (Fig. 4.8).

ICELL(1, node number)	=	Central	node number
ICELL(2, node number)	=	SW	node number
ICELL(3, node number)	=	S	node number
ICELL(4, node number)	=	SE	node number
ICELL(5, node number)	=	E	node number
ICELL(6, node number)	=	NE	node number
ICELL(7, node number)	=	N	node number
ICELL(8, node number)	=	NW	node number
ICELL(9, node number)	=	W	node number

Again, if a node does not exist, its location in the cell pointer receives a zero.

These computational structures make clear the advantages of the integration scheme as presented in the previous chapter. By formulating "cell changes" and "distribution formulae," we may apply this node-based scheme in a completely unstructured manner on general moving or stationary grids.

In addition, other pointers can be defined for convenience. The overall system was developed by Dannenhoffer and Baron (6) and has been used with minor modifications by (17), (33) and (34) among others.

4.4 Cell Division

Several authors discuss the process of cell division (7, 33, and 34) in some detail. In general, these algorithms are tailored to a specific data structure and pointer system. After first

describing the steps which all such algorithms must include, this section discusses the present approach.

Cell division not only adds new cells and nodes to the data structure, but also changes the global grid connectivity. Obviously the pointer system must account for these changes. The matrices must absorb the new cells and nodes seamlessly, insuring that new cells require no special treatment by the integrator.

The steps which all cell division algorithms must include are (Fig. 4.10):

- a. Find cell number of the tagged cell
- b. Find cell numbers of the 12 surrounding cells (zero if no cell exists)
- c. Find node numbers of nodes 2-9 if they exist
- d. Create new node at center (Fig. 4.10, node 1)
- e. Create new nodes at the center of each face if they do not exist already
- f. Update pointers of cell being divided to reflect new corner nodes and new size
- g. Create four new cells by appending Cell pointer
- h. Update neighbor pointers of nodes 1-9
- i. Inform surrounding cell pointers of any new nodes
- j. Find boundary location for new boundary nodes
- k. For moving grids, specify position of new nodes relative to existing nodes
(see Chap. 5)

Since the state vector and auxiliary properties (p , T , h_o , etc.) reside at nodal locations, new nodes must be accompanied by initial guesses for these variables. Properties at new face nodes take values equal to the average of the corner nodes, while properties at central nodes take the simple average of all four corner nodes.

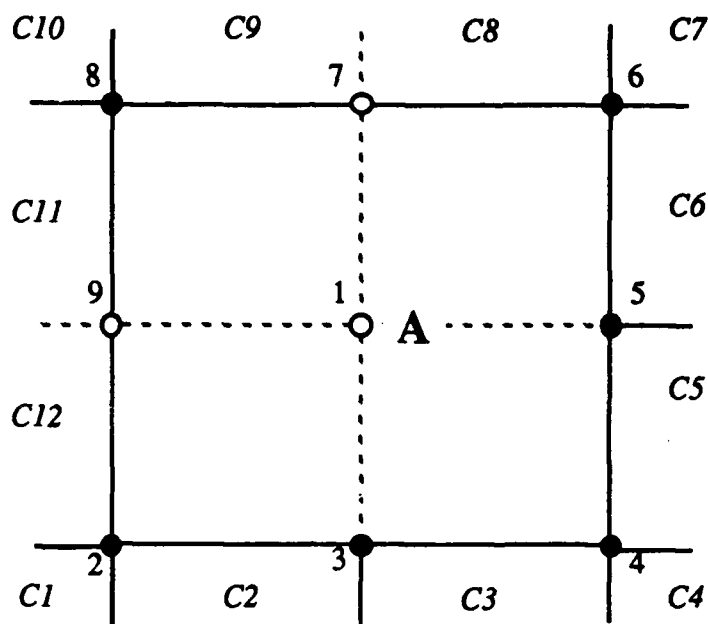


FIGURE 4.10
Cell A tagged for division.

Naturally, new nodes which lie on boundaries require special attention. In addition to finding the correct position of the new node (either from interrogation of the surface splines, or from metrics of surrounding nodes) the boundary pointer must receive this new information. By looping through the new nodes after division, it is relatively simple to update the pointer to account for new boundary nodes.

Implementation

Implementing these steps requires specific decisions about data structure, appending pointers, preserving parent cell information, etc.. As a result, implementation differs with each investigator.

By avoiding "holes" in the data structure where a cell "existed" before division and placing new cells and nodes at the end of their respective pointers, the procedure described here results in an adapted data structure indistinguishable from the original grid. Thus, the solver never need know when it operates on an adapted cell. This permits sequential integration of each cell without ever asking if a cell has been divided and without skipping over any vacancies

in the pointer. While very attractive from the viewpoint of simplicity and elegance, this system does not retain parent information and does exclude the possibility of applying a multigrid accelerator.

For an arbitrary tagged cell n in a grid of M cells Figure 4.11 details the cell division process. Cell n shrinks in size requiring new connectivity (ICELL, and NEIB pointers). The scheme numbers the three new cells counterclockwise $M + 1$ through $M + 3$. These new cells are "connected" to the appropriate nodes ($1 \rightarrow 9$) by appending the ICELL pointer. All nodes then reconnect to their surrounding cells by updating the NEIB pointer, completing the process.

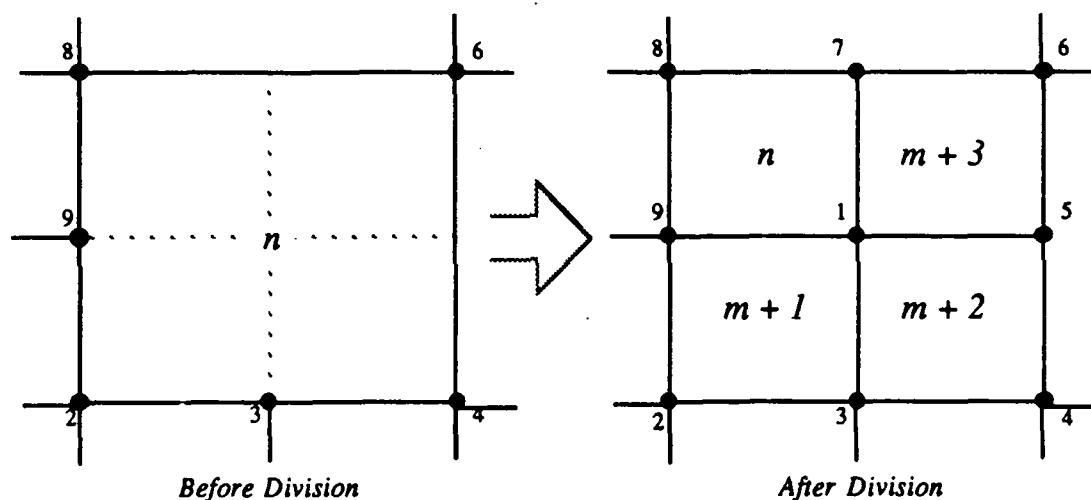


FIGURE 4.11
Cell division and pointer updating.

Note the simplicity of this scheme. The updated ICELL pointer has three additional entries and no vacancies. The NEIB and GEOM pointers extend by the number of new nodes with a minimum of complexity.

References 7, 33 and 34 offer more elaborate treatments of the cell division process.

4.5 Cell Interfaces

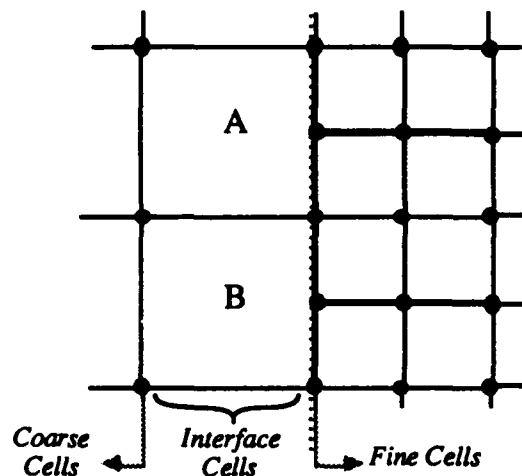


FIGURE 4.12
Interface in computational mesh.

Grid refinement and adaptation introduce internal boundaries between cells of different size. Figure 4.12 depicts such an *interface*. Here, only one column of cells actually differs from those considered in the previous chapter. The integration scheme holds equally well on the fine cells at the right and the coarse cells to the left of *A* and *B*. Each of these has exactly four nodes. However, cells bordering on the embedded region (*A* and *B*) always contain at least one hanging node and require special treatment. To gain insight into the scheme's behavior near such boundaries, examine the two situations depicted below.

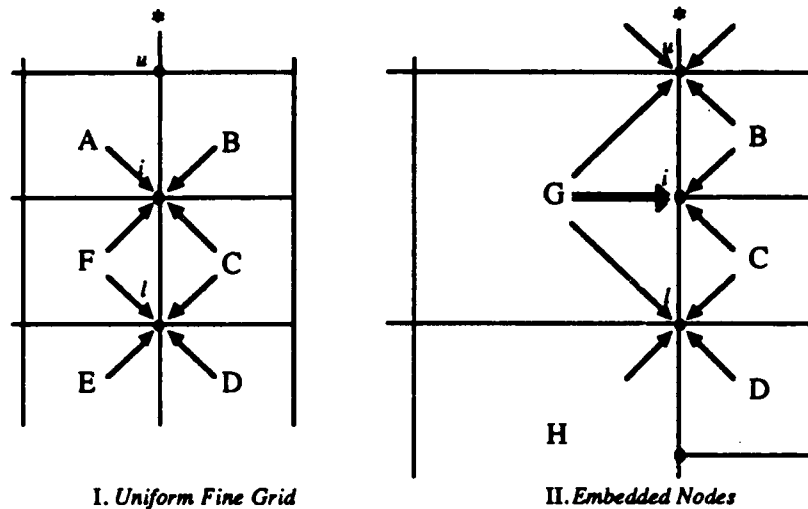


FIGURE 4.13
Comparison of interface cells with cells of a uniform grid.

Consider the model convective equation

$$U_t + F_x = 0. \quad (4.4)$$

with the cell and flux changes for any cell defined by

$$\Delta U = (F_w - F_e) \frac{\Delta t}{\Delta x}$$

and

$$\Delta F = F_U \Delta U.$$

Here the subscripts *w* and *e* represent average quantities on the west and east faces of any cell.

Since this is essentially a 1-D equation discretized on a 2-D grid, properties remain constant along vertical lines. Now examine the difference between nodes *l* in Parts I and II of Figure 4.13.

Although node *l* receives four changes from its surrounding cells in both cases, the two pictures are not equivalent. Since Ni's scheme is simply central differencing (on cartesian grids), we expect a stretching error in the mesh of Case II. To demonstrate this, examine the changes to node *l* for Case I and Case II, $\delta U_l)_I$ and $\delta U_l)_II$.

Case I:

By Equation (3.9):

$$\begin{aligned}\delta U_{I_C} &= \frac{1}{4} \left[\Delta U_C - \frac{\Delta t}{\Delta x_C} \Delta F_C \right] = \frac{\Delta U_C}{4} \left[1 - \frac{\Delta t}{\Delta x_C} F_{U_C} \right] \\ \delta U_{I_D} &= \frac{\Delta U_D}{4} \left[1 - \frac{\Delta t}{\Delta x_D} F_{U_D} \right] \\ \delta U_{I_E} &= \frac{\Delta U_E}{4} \left[1 + \frac{\Delta t}{\Delta x_E} F_{U_E} \right] \\ \delta U_{I_F} &= \frac{\Delta U_F}{4} \left[1 + \frac{\Delta t}{\Delta x_F} F_{U_F} \right]\end{aligned}\quad (4.5)$$

Recalling the governing Equation (4.4), and considering 1-D convection only, notice that since all cells are identical, $\delta U_{I_E} = \delta U_{I_F} = \delta U_{I_A} = \delta U_{I_B}$. Also, the lack of variation in the vertical direction makes the changes at node i from B and C equivalent to those from C and D at I .

For the first case, the total change to node I is the sum of the contributions from the four surrounding cells. Assuming a constant CFL number defined by

$$CFL \equiv \frac{\Delta t \partial F}{\Delta x \partial U}$$

gives Equation (4.6).

$$\delta U_{I_I} = \delta U_{I_{C+D+E+F}} = \frac{1}{4} [(\Delta U_C + \Delta U_D)(1 - CFL) + (\Delta U_F + \Delta U_E)(1 + CFL)] \quad (4.6)$$

Case II:

Again, using Equation (3.9) gives:

$$\begin{aligned}\delta U_{I_C} &= \frac{\Delta U_C}{4} \left[1 - \frac{\Delta t}{\Delta x_C} F_{U_C} \right] \\ \delta U_{I_D} &= \frac{\Delta U_D}{4} \left[1 - \frac{\Delta t}{\Delta x_D} F_{U_D} \right] \\ \delta U_{I_G} &= \frac{\Delta U_G}{4} \left[1 + \frac{\Delta t}{\Delta x_G} F_{U_G} \right] \\ \delta U_{I_H} &= \frac{\Delta U_H}{4} \left[1 + \frac{\Delta t}{\Delta x_H} F_{U_H} \right]\end{aligned}\quad (4.7)$$

where $\delta U_{I_G} = \delta U_{I_H}$ and $\delta U_{I_C} = \delta U_{I_D}$.

Summing gives the total change at node l across the interface.

$$\delta U_l)_{II} = \delta U_l)_{C+D+G+H} = \frac{1}{4}[(\Delta U_C + \Delta U_D)(1 - CFL) + (\Delta U_G + \Delta U_H)(1 + CFL)] \quad (4.8)$$

We may now compare the changes at node l between the two cases. Since Cells C and D are identical in both cases, Equations (4.6) and (4.8) combine into

$$\delta U_l)_{II} = \delta U_l)_{II} + \frac{(1+CFL)}{4}[-(\Delta U_F + \Delta U_E) + (\Delta U_G + \Delta U_H)] \quad (4.9)$$

The term in brackets represents the error resulting from the stretched difference stencil in the second case. Notice that this first order error disappears when $\Delta U_F = \Delta U_G$ and $\Delta U_E = \Delta U_H$; i.e. when the difference stencil is not stretched.

Having examined the expected error due to grid stretching across interfaces, we may now take up the issue of hanging nodes on these boundaries. Referring again to Figure (4.13), notice that cell G contains a hanging node i on its eastern face. As an interface node, i must suffer from the same stretching error as l . However, we hope to avoid any additional error caused by distributing incorrectly from cell G to node i . The scheme should treat nodes i and l identically.

With these thoughts in mind, the net change to node i in Case II becomes:

$$\begin{aligned} \delta U_i)_{II} &= \delta U_i)_{B+C+G} = \delta U_i)_{B} + \delta U_i)_{C} + (k_u \delta U_u + k_l \delta U_l)_{G} \\ &= \frac{1}{4}(\Delta U_B + \Delta U_G)(1 - CFL) + \frac{\Delta U_G}{4}(k_u + k_l)(1 + CFL) \end{aligned} \quad (4.10)$$

k_u and k_l weight the contributions to the upper and lower nodes on the eastern face in order to apply them directly to i . For example if $k_u = k_l = 1/2$ Equation (4.10) would distribute the average of δU_{uG} and δU_{lG} to i .

In the first case

$$\begin{aligned}\delta U_{iH} &= \delta U_{iB} + \delta U_{iC} + \delta U_{iA} + \delta U_{iF} \\ &= \frac{1}{4}[(\Delta U_B + \Delta U_C)(1 - \text{CFL}) + (\Delta U_A + \Delta U_F)(1 + \text{CFL})]\end{aligned}\quad (4.11)$$

and substituting this expression into (4.10) for δU_{iI} gives (4.12).

$$\delta U_{iII} = \delta U_{iH} + \frac{(1 + \text{CFL})}{4}[\Delta U_G(k_u + k_l) - (\Delta U_A + \Delta U_F)] \quad (4.12)$$

However, since properties vary in x only, $\Delta U_A = \Delta U_F = \Delta U_E$ and $\Delta U_G = \Delta U_H$, giving:

$$\delta U_{iII} = \delta U_{iH} + \frac{(1 + \text{CFL})}{4}[-(\Delta U_F + \Delta U_E) + \Delta U_G(k_u + k_l)] \quad (4.13)$$

Treating nodes i and l identically requires that the change at i equal the change at l . Comparing (4.13) with that for node l_{II} and recalling that $\delta U_{iI} = \delta U_{lI}$ leads to:

$$\Delta U_G(k_u + k_l) = (\Delta U_G + \Delta U_H)$$

But, since $\Delta U_G = \Delta U_H$,

$$\begin{aligned}\Delta U_G(k_u + k_l) &= 2\Delta U_G \\ \text{or} \quad k_u + k_l &= 2\end{aligned}\quad (4.14)$$

Since no reason exists favoring either node u or l

$$k_u = k_l = 1 \quad (4.15)$$

This result implies that the mid-face node i should receive the sum of the changes distributed to the vertices of the face. Figure 4.14 displays this interface treatment pictorially.

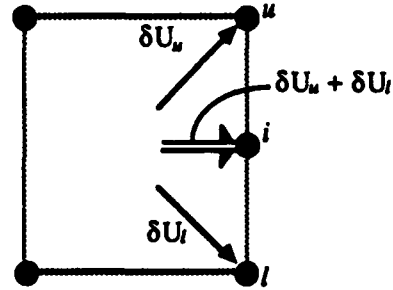


FIGURE 4.14
Distribution to mid-face node

It is worth noting that this result contrasts that presented by Dannenhoffer (7) where he suggested $k_u = k_l = 1/2$. More recently, Kallinderis (18) examined several interface treatments

showing Equation (4.15) to be not only conservative, but also a time accurate interface treatment.

Actually, the case of $k_u = k_l = 1/2$ bears special attention. If F varies linearly and F_U is constant, the cell change in a large cell like G would be exactly twice that of a small cell (E, F , etc.). Re-examining Eq.(4.13) now reveals:

$$\delta U_i)_{II} = \delta U_i)_{II} + \frac{(1+CFL)}{4} [-2\Delta U_{Small} + \Delta U_{Large}(k_u + k_l)] \quad (4.16)$$

but since ΔU_{Large} is twice ΔU_{Small} , the bracket vanishes. $k_u = k_l = 1/2$ exactly *corrects for* the grid stretching error in this special case. By re-weighting the difference stencil, it removes the inaccuracy at node i . Unfortunately, it is not so easy to counteract the stretching effects at u or l resulting in an non-uniform treatment of the interface before reaching the steady state. Notice also, that this fortuitous canceling within the bracket of Eq. (4.16) occurs only under the special conditions of $F_U = \text{Const}$ and linear variation of F .

Conservation vs. Accuracy

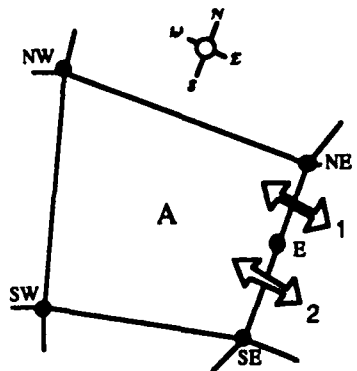
As noted earlier, the interface treatment described in the preceding section is conservative, but the stretched difference stencil leads to a first order error as noted after Eq. (4.9). It is reasonable to look for an interface treatment which is both conservative and accurate. Kallinderis examines this question at length and discovers that the second difference smoothing induces a first order mass flow error in accurate treatments (18, pp.145). Since the shock layer may be thought of as a control volume, any induced mass flow from non-conservation will create an error in shock stand-off distance. Thus we opt for conservation over accuracy to preserve shock location and shape.

4.6 Integration Scheme on Interface Cells

The cell in Figure 4.14 contains a *hanging node* on its eastern face. Failure to include information from this node when computing the flux integral around such a cell will obviously result in a conservation error across that face. Such an error is unacceptable, as emphasized in the last section.

The integration scheme of Chapter 3 (or those in Appendix A) accommodates this hanging node. With the distribution algorithm already discussed, only the calculation of cell changes requires attention.

Consider the more general cell of Figure 4.15. When computing the flux integral Equation (3.13) the flux through the east face may be split into two parts.



$$f_e = \oint F dy - G dx$$

$$= \left[\left(\frac{F_{NE} + F_E}{2} \right) (y_{NE} - y_E) - \left(\frac{G_{NE} + G_E}{2} \right) (x_{NE} - x_E) \right] + \left[\left(\frac{F_E + F_{SE}}{2} \right) (y_E - y_{SE}) - \left(\frac{G_E + G_{SE}}{2} \right) (x_E - x_{SE}) \right] \quad (4.17)$$

FIGURE 4.15
General interface cell.

Here the first bracket tracks the flux through face 1 while the second follows flux through face 2. Since all divided cells have straight faces, massaging Equation (4.17) results in the parabolic form below.

$$f_e = \left[\left(\frac{F_{NE} + 2F_E + F_{SE}}{4} \right) (y_{NE} - y_{SE}) - \left(\frac{G_{NE} + 2G_E + G_{SE}}{4} \right) (x_{NE} - x_{SE}) \right] \quad (4.18)$$

Implementation

If the mid-face node is equal to the average of its corner nodes, Equation (4.18) reduces exactly to Eq. (3.14). This property suggests a general interface treatment for interface cells. When the solver first examines an interface cell, it creates *virtual nodes* at the midpoint of each face not already containing a real node. By averaging corner values of F , G and W at these virtual nodes, cells with hanging nodes on any (or all) faces may be treated by a single integration formula - one that expects nodes on all faces. This approach avoids the expensive logic statements and repetitive subroutines required to treat all possible combinations of hanging nodes separately. Moreover, interface cells may be treated with no decision statements whatsoever by defining a pointer to locate which faces of any cell contain real midface nodes.

In 2-D cartesian coordinates, the first-order cell change for a cell with real or virtual nodes on all faces is:

$$\Delta U)_C = \Delta t W_C - \frac{\Delta t}{A_C} \left[\begin{aligned} & \left(\frac{F_{NE} + 2F_E + F_{SE}}{4} \right) (y_{NE} - y_{SE}) - \left(\frac{G_{NE} + 2G_E + G_{SE}}{4} \right) (x_{NE} - x_{SE}) \\ & \left(\frac{F_{NW} + 2F_N + F_{NE}}{4} \right) (y_{NW} - y_{NE}) - \left(\frac{G_{NW} + 2G_N + G_{NE}}{4} \right) (x_{NW} - x_{NE}) \\ & \left(\frac{F_{SW} + 2F_W + F_{NW}}{4} \right) (y_{SW} - y_{NW}) - \left(\frac{G_{SW} + 2G_W + G_{NW}}{4} \right) (x_{SW} - x_{NW}) \\ & \left(\frac{F_{SE} + 2F_S + F_{SW}}{4} \right) (y_{SE} - y_{SW}) - \left(\frac{G_{SE} + 2G_S + G_{SW}}{4} \right) (x_{SE} - x_{SW}) \end{aligned} \right] \quad (4.19)$$

Efficiency

Despite the expense of defining an additional pointer and creating virtual nodes, the result is less machine code than the decision statements and subroutines they replace. Also, since nodal placements change only during adaptation, this pointer updates only during adaptation steps - at negligible cost. This general treatment is much simpler to code, and since interface cells are only a small fraction of the total cell count, minor savings gained by more elaborate treatments appear difficult to justify.

5. Unstructured Shock Fitting

In many situations it is reasonable to take the bow shock as the upstream boundary. "Fitting" the shock in this manner forces the computational domain to be coincident with the disturbed physical domain. The shock's position is unknown *a priori*, and its final position depends upon the physics within the shock layer and the geometry. This underscores the importance of formulating the governing equations in strong conservation law form, and treating interfaces conservatively.

In practice, most blunt body flows lend themselves to bow shock fitting. Nevertheless, at some altitude the Knudsen number becomes sufficiently large to prohibit accurate modeling with a discontinuous treatment of the shock boundary. Nominal shock thickness estimates are between five and seven mean free paths thick. For example, at an altitude of 78 km in the standard atmosphere, the Knudsen number based on freestream conditions and a one meter nose is 0.0028. The shock is approximately $0.01 R_n$ thick. Taking this as a rough upper limit for the assumption of a discontinuous shock, we wish to examine other assumptions behind the current modeling. The sustained flight corridor of Figure 1.1 shows that airbreathing flight at upper altitudes requires Mach numbers large enough to invalidate the relatively simple chemical model described in the second chapter. The assumptions within the gas model break down before the shock thickness is appreciable. Thus, for the class of sustained flight

problems correctly treated by the gas model, the bow shocks are thin enough to warrant shock fitting.

Many early shock fitting approaches relied on a time dependent technique developed by Moretti (27). This approach casts the governing equations in characteristic variables to solve the compatibility equation along characteristic lines. Matching the results with those from the moving shock Rankine - Hugoniot relations determines a unique shock speed and results in a time-accurate procedure.

Such an approach suffers from two drawbacks in the context of real gas problems solved on unstructured finite volume meshes. The Riemann invariants do not remain constant through the entropy gradients downstream of a curved shock. In perfect gases, this problem alone is not limiting since one may always place nodes close enough to the shock that it "appears" locally planar. However, in chemically excited flows, the rapidly relaxing region just behind the bow shock is strongly non-isentropic along streamlines. The closer the cells lie to the shock, the steeper the chemical gradients and the more severe this situation becomes. Secondly, it is not clear that explicit forms of the characteristic variables and compatibility equation exist for general equations of state.

Blottner and Larson (3) recently proposed a shock fitting technique that avoids those problems. The next section discusses their basic technique applied to nonequilibrium flow. While much simpler in both concept and implementation, the technique is not time accurate.

Despite the fact that the flows under consideration are out of equilibrium, the frozen shock Rankine - Hugoniot relations still apply. The translational mode equilibrates much faster than chemical modes. Typically the shock builds in fewer than ten collisions, while thousands occur before the chemistry reaches equilibrium. Thus, for the present gas model, it is reasonable to treat the classical shock as a sharp, frozen discontinuity, while still permitting nonequilibrium chemistry.

5.1 Perfect Gas Shock Fitting

After first integrating the entire domain, shock boundary nodes receive suggested changes from their neighboring cells. The shock fitting scheme corrects the state vector at such points consistent with the appropriate moving shock Rankine - Hugoniot relations and moves the shock in response to the developing interior solution. The interior nodes then undergo a re-mapping between the upgraded shock location and body surface.

Beginning with the Rankine - Hugoniot shock jump relations, this section develops the shock fitting technique with an eye toward implementation. For some known freestream normal Mach number component, the normal shock equations determine the state vector U downstream of the discontinuity. However, if the shock is moving, one must first find its speed before computing U (Figure 5.1). In a reference frame moving with the shock, the shock "sees" a *relative freestream Mach number* whose normal component is M_{R_n} which results from the vector subtraction of the *absolute normal Mach number*, $M_{n_{\infty}}$, and the non-dimensional shock speed, b_n . $M_{n_{\infty}}$ is defined as the normal freestream Mach number in the body's frame of reference - with no relative shock motion. Figures 5.1 and 5.2 define these quantities pictorially.

$$M_{R_n} = M_{n_{\infty}} - b_n \quad (5.1)$$

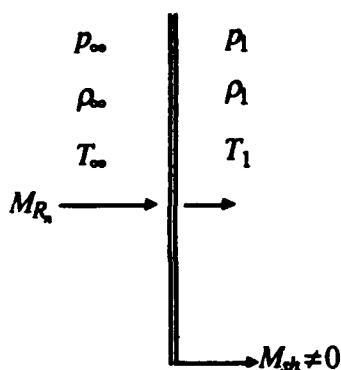


FIGURE 5.1
Definition of normal relative Mach number.

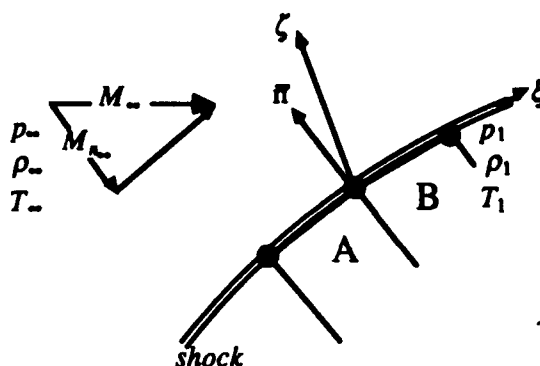


FIGURE 5.2
Definition of absolute normal Mach number.

To determine M_{Rn} we employ the solution from the most recent integration step. Presumably, this step produced changes at the shock nodes resulting from the arrival of waves which propagate throughout the domain. Over the course of convergence this information ultimately determines the shock stand-off distance.

The same information provides an indication of shock speed. For example, at the shock node 1, the ratio of the downstream temperature T_1 to the freestream temperature T_∞ could be interpreted as resulting from some shock. Such a temperature ratio indicates a "shock" of specific strength, with a specific associated Mach number. In this way, T_1/T_∞ defines a specific *relative* Mach number. However, the basis of shock strength need not be temperature ratio. Ratios of p , e , ρ , etc. also determine equally valid relative Mach numbers. It is this non-uniqueness that makes time-accurate re-formulation of this procedure unclear.

Since density is a state variable, the density ratio, ρ_1/ρ_∞ , was used to determine M_{Rn} in the present work. However, exploratory investigations using pressure or temperature ratios displayed negligible differences in convergence behavior.

The value of M_{Rn} then determines all properties "just behind" the shock through the shock jump relations and equation of state. The updated solution vector applies to a moving

shock and to the steady state as the shock speed vanishes. Rewriting (5.1) for the shock speed:

$$b_n = M_{n\infty} - M_{R_n} \quad (5.2)$$

Complete Equations

Figure 5.2 describes the situation in a 2-D or axisymmetric domain. Here, note that the outward normal, n , does not necessarily correspond with the ζ direction, indicating that this formulation includes non-orthogonal coordinates. The density ratio after the integration step determines M_{R_n} from the shock jump relations.

$$M_{R_n}^2 = 2 \left[\frac{\rho_\infty}{\rho_1} (\gamma_\infty + 1) - (\gamma_\infty - 1) \right]^{-1} \quad (5.3)$$

If the shock were stationary with respect to the body, the absolute normal Mach number $M_{n\infty}$ would be: (in a reference frame attached to the body)

$$M_{n\infty} = M_\infty \frac{\partial y}{\partial \xi} \quad (5.4)$$

The assumed density ratio and relative Mach number now completely specify conditions behind the shock. The x and y velocity components are:

$$u_1 = \frac{(p_1 - p_\infty)}{\rho_\infty M_{R_n} g_{\zeta\zeta}} \zeta_x + U_\infty \quad (5.5)$$

$$v_1 = \frac{(p_1 - p_\infty)}{\rho_\infty M_{R_n} g_{\zeta\zeta}} \zeta_y + V_\infty$$

and the local speed is $V^2 = u^2 + v^2$. Here $g_{\zeta\zeta}$ corrects for any non-orthogonality of the local ξ, ζ transformation. From vector calculus

$$g_{\zeta\zeta} = \sqrt{\zeta_x^2 + \zeta_y^2} \quad (5.6)$$

Since the shock is assumed frozen, the equation of state for a mixture of perfect gases determines the temperature downstream of the shock.

$$T_1 = \frac{p_1}{\rho_1 \mathcal{R} \sum_i \left(\frac{c_i}{m_i} \right)} \quad (5.7)$$

The energy expression from (Eq. 2.8) completes the state vector behind the shock.

Note that the state vector along the shock is consistent with a moving shock, and h_o will vary until the shock stops moving. At that time, h_o takes on its freestream value.

In a time Δt , the shock moves a distance Δx , Δy in accordance with its normal shock speed from Equation (5.2).

$$\begin{aligned} \Delta x_1 &= -\Delta t b_n \frac{\partial x}{\partial \xi} g_{\zeta\zeta} \\ \Delta y_1 &= -\Delta t b_n \frac{\partial y}{\partial \xi} g_{\zeta\zeta} \end{aligned} \quad (5.8)$$

In these equations, the node time step is simply an average of the time steps from the two neighboring cells (e.g. in Figure 5.2 $\Delta t_i = \Delta t_A + \Delta t_B$).

5.2 Equilibrium Shock Fitting

As an upper limit for finite rate chemistry, equilibrium provides a convenient basis for comparison with *very* rapid chemistry. Given this motivation, we now develop a separate method for fitting equilibrium shocks. The discussion revolves around a specific equilibrium gas model, but applies to any gas in chemical equilibrium.

For simplicity, consider the reaction $A_2 + M \rightleftharpoons 2A + M$ as described by Lighthill's ideal dissociating gas model. In equilibrium, the shock jumps are accompanied by changes in γ across the shock. For Lighthill's model,

$$\gamma = \frac{4 + \alpha}{3} \quad (5.9)$$

Here α is the degree of dissociation (36, pp.159-161). Thus the ratio of specific heats depends upon the degree of dissociation. However, simply changing γ in the perfect gas Rankine - Hugoniot relations neglects the $\alpha \Theta_d$ energy absorbed in dissociation (see for example Eq. 2.6). Obviously, the resulting shock would not preserve stagnation enthalpy, and would violate energy conservation.

Ruling out the use of closed form shock jump relations leaves the need to perform equilibrium normal shock calculations and then find the correct shock speed.

Mechanics

Referring again to Figure 5.1, the flowfield solution from the previous iteration provides a pressure jump across the shock, p_1/p_∞ . Using the equation of state with an assumed value of α_1 gives the density just downstream of the shock.

$$\rho_1 = \frac{p_1}{R_{A_2} T (1 + \alpha_1)} \quad (5.10)$$

Conservation of momentum through the discontinuity results in an expression for the relative normal velocity at 1 (36, pp. 179).

$$U_{R_n}^2 = \frac{\rho_1 (p_1 - p_\infty)}{\rho_\infty (\rho_1 - \rho_\infty)} \quad (5.11)$$

Energy conservation determines a corresponding value of enthalpy behind the shock.

$$h_1 = h_\infty + \frac{U_{R_n}^2}{2} \left[1 - \left(\frac{\rho_1}{\rho_\infty} \right)^2 \right] \quad (5.12)$$

Recalling the enthalpy expression for the ideal dissociating gas:

$$h = R_{A_2}[(4 + \alpha)T + \alpha \Theta_d]$$

Re-arranging, expresses the temperature downstream of the shock as a function of enthalpy and mass fraction.

$$T_1 = \frac{1}{(4 + \alpha_1)} \left[\frac{h_1}{R_{A_2}} - \alpha_1 \Theta_d \right] \quad (5.13)$$

and this temperature permits a better estimate of the atomic mass fraction at 1.

$$\alpha = \frac{-k + \sqrt{k^2 + 4k}}{2} \quad \text{where} \quad k \equiv \frac{\rho_d}{\rho} e^{-\Theta_d/T} \quad (5.14)$$

However, (5.13) assumed the previous value of α , and we must now compute a new temperature consistent with the mass fraction determined by (5.14). Iteration between Equations (5.13) and (5.14) determines a unique mass fraction and temperature. Then (5.10) provides a consistent value of the density ratio across the shock and (5.11) yields an improved shock speed.

This doubly iterative process initially may appear computationally expensive. However, it is applied only to shock points, and the net cost remains small. After obtaining a converged relative Mach number, the shock speed and subsequent motion follow as in the previous section.

Some Notes on Equilibrium Shock Fitting

The method described above is not elegant. One possible alternative might make use of the fact that thermodynamic equilibrium minimizes the Gibbs free energy. Setting up the minimization problem permits the use of LaGrange multipliers constrained by the existing

pressure or density jump. Certainly extending the model to include multiple coupled reactions (NO present) with many reaction paths would demand a more elaborate approach.

As a final comment, the stiff transcendental function in Equation (5.14) results in extreme sensitivity of α to small changes in T . Specifically, α tends to oscillate between 0.0 and 1.0, hampering convergence of this inner iteration. A simple fix is to reduce changes in α by approximately 70%, thus decreasing changes to T , and resulting in a more tractable convergence behavior.

5.3 Moving Unstructured Meshes

A moving inflow boundary implies that the grid must redistribute itself to properly track the shock's motion. For structured grid calculations, this merits relatively little attention. However, in the realm of the current unstructured domain, more care is required.

The grid redistribution requires knowledge of shock position and information about a particular node's history in the grid (stretching or skewing). Since all previous discussions involve current cell information only, such *global* location requests do not fit within the framework of an unstructured scheme.

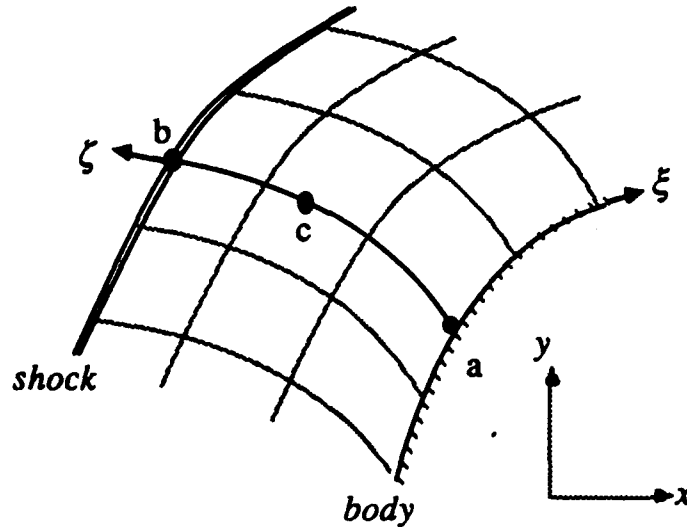


FIGURE 5.3
Reference points for moving nodes on the base (original) grid.

The *endpoint* pointer fixes all nodal locations with respect to any set of four reference nodes. The pointer's six elements store reference node numbers as well as x and y position with respect to these references. Referring to the nodes on the unadapted mesh of Figure 5.3, the pointer fills as follows.

$$\begin{aligned}
 \text{ENDPT}(1, c) &= \text{body node \# (a)} \\
 \text{ENDPT}(2, c) &= \text{body node \# (b)} \\
 \text{ENDPT}(3, c) &= \% x \text{ of total distance } \overline{ab} \text{ measured from } a \\
 \text{ENDPT}(4, c) &= \% y \text{ of total distance } \overline{ab} \text{ measured from } a \\
 \text{ENDPT}(5, c) &= \text{body node \# (a)} \\
 \text{ENDPT}(6, c) &= \text{body node \# (b)}
 \end{aligned}$$

These definitions locate original grid nodes by their position along lines of constant ξ . Since it is based upon the original grid, this pointer preserves any curvature or clustering of grid lines.

After each adaptation, every new cell must have faces matching those of its neighbors across cell interfaces. Failure to keep these faces linear results in higher order conservation errors across the interface when integrating adjacent cells. Unfortunately, referring mid-face nodes to shock and body points does not insure linear cell faces as the grid moves, and we seek an alternative solution.

Figure 5.4 examines this situation in more detail. If midface and central nodes rely on body and shock locations, there is no guarantee that linear interfaces will be preserved. To avoid this problem, the endpoint pointer positions new nodes by the corners of their supercells. For the example shown in the sketch, all new nodes should rely on the corner nodes of the original Cell A. Specifically, for new nodes created from the division of Cell A, the ENDPT pointer entries 1, 2, 5, and 6 will refer to corner node data for the original Cell A. Using these reference points, each midface node remains half way between the corners, falling exactly on the interface. Through this more general use of the pointer, the re-mapping algorithm can treat new nodes exactly as original nodes, efficiently creating a new grid without any decision statements (and minimizing computational effort). Finally, note that this pointer permits remapping grids with any number of embedded levels, while simultaneously maintaining all cell interfaces as straight lines.

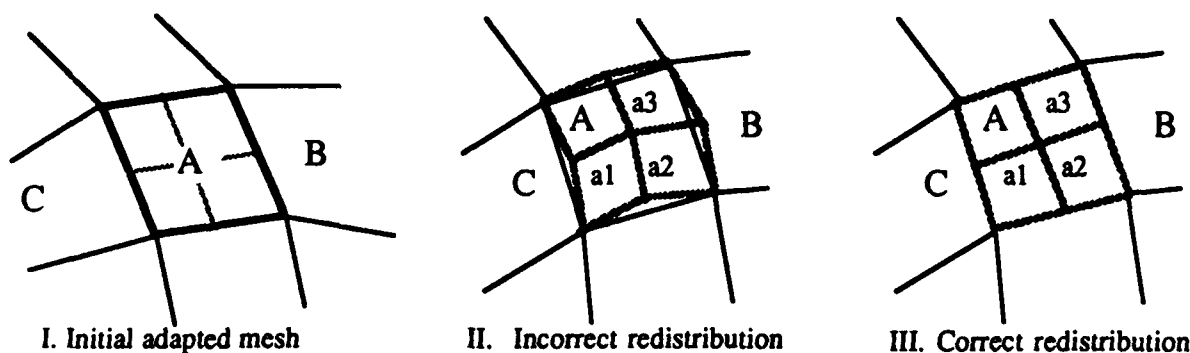


FIGURE 5.4
Preservation of linear interfaces in an unstructured domain with multiple levels of adaptive embedding.

5.4 Behavior of Shock Fit Solutions

As an initial condition, all points within the domain (Fig 3.14, including shock points) might contain freestream values. In this case, no shock discontinuity exists, and the initial conditions exactly satisfy the governing equations at all points not on the body. With

freestream values, all shock points span a density ratio $\rho_{sh}/\rho_\infty = 1.0$ and the shock degenerates to an acoustic wave. Confirming this, Equation (5.3) predicts a relative normal Mach number of unity, and (5.5) through (5.6) predict the same for the velocity ratio, temperature ratio and pressure ratio at all shock points and the "shock" moves inward at a non-dimensional speed b_n of $M_\infty - 1$.

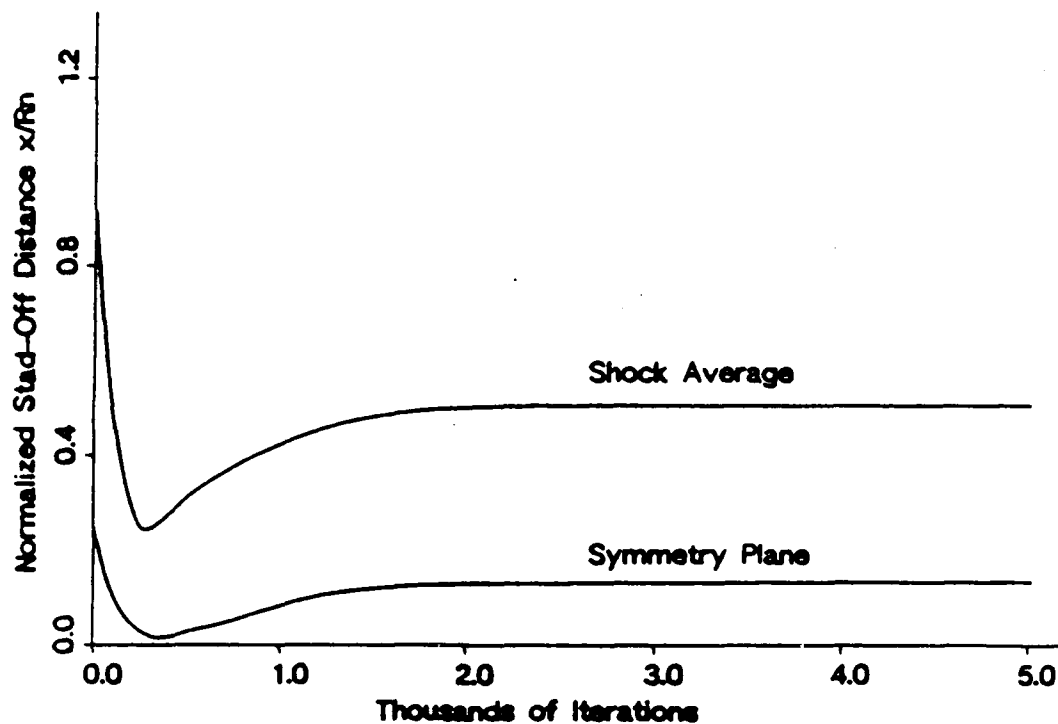


FIGURE 5.5

A typical history of stand-off distance with iteration, converged from a uniform freestream initial condition. (Mach 5 frozen flow over a axisymmetric nose.)

During the first time step, the explicit solver transmits knowledge of the body to adjacent cells one removed from this boundary. Meanwhile, the shock continues progressing towards the body at a speed $M_\infty - 1$. On a grid with M lines between the shock and body, the shock will not respond to the body's presence for M time steps. This behavior is a direct result of the explicit algorithm, and results in a time lag between the shock and the developing solution. Moreover, it creates a feedback loop wherein the shock's position and shape determine properties within the domain, but the shock cannot respond immediately to these changing

properties. In this respect, the problem resembles an elliptic calculation (albeit one with an internal time lag).

Figure 5.5 shows a typical history of shock motion recorded while converging a Mach 5 solution from freestream conditions. Initially, the shock resides some distance from the body and moves toward it as described above. Then, as pressure waves cross the layer, the Rankine - Hugoniot jumps build, slowing the shock before reversing its motion altogether. The shock backs away from the body and eventually comes to rest at some final stand-off distance determined by the interior solution.

Although this example of shock adjustment was computed from a special (freestream) initial condition, the shock's behavior results more generally from wave propagation in the explicit shock fit domain. In practice, the shock adjusts its position in a similar manner to all disturbances (changes in freestream conditions, chemistry, etc.).

Since adaptation selectively adds cells to the domain, it changes the wave propagation speed through various regions of the domain (in physical space). As a result, adapting during the initial gross shock motion may disrupt the shock's shape enough to destabilize the solution. Simply delaying until the stand-off distance stabilizes avoids this shortcoming.

III PRESENTATION AND DISCUSSION OF RESULTS

A DEC Microvax 3200, nominally rated at 3 Million Instructions Per Second (MIPS), provided processing support for all test cases in this work.

6. Physical Phenomena in High Temperature Flows Over Simple Geometries

The gas model and adaptive integration scheme discussed in Parts I and II led to the development of a series of adaptive hypersonic CFD codes. These codes permit computation of inviscid and viscous, chemically reacting flow over 2-D and axisymmetric bodies. The additional development of a 2-D identical equilibrium Euler solver provided a datum for flows demonstrating very small departure from equilibrium.

After a brief validation study, focus turns to the question of using adaptation to resolve physical behavior within the reacting shock layer. Both inviscid and viscous results support a fundamental discussion of chemical length scale behavior within the shock layer. Finally, as we consider flows with higher Mach numbers, interest broadens to coupled and uncoupled multiple reacting mixtures, examining both the formation and impact of *NO* within a gas cap, and the degree of coupling between reactions. These insights form a basis for then evaluating the effectiveness of adaptive grid embedding in hypersonic shock layers in Chapter 7.

6.1 Basic Examples and Algorithm Verification

Before looking at the detailed physics and flow phenomena within the shock layer, validation studies were completed to lend credibility to both the basic algorithm and gas model. This section outlines three such studies, designed to verify different aspects of the solution

algorithm. First is a classic perfect gas test case, which demonstrates both the accuracy and conservation of the Lax-Wendroff algorithm and unstructured shock fitting procedure. A more rigorous test examines the adaptation methodology and gas model behavior in severe reacting flows. A final example evaluates the effectiveness of the present method in tracking multiple reaction paths and coupled reactions in a multi-reaction mixture.

Perfect Gas Test Cases

Figure 6.1 displays the traditional variation of stand-off distance with Mach number for a 2-D cylinder exposed to a crossflow and an axisymmetric hemispherical cylinder test case. Reference 22 provided the comparison curves, and the data show numerical experiments at Mach 3, 5, 7.5 and 10 in a $\gamma = 1.4$ perfect gas.

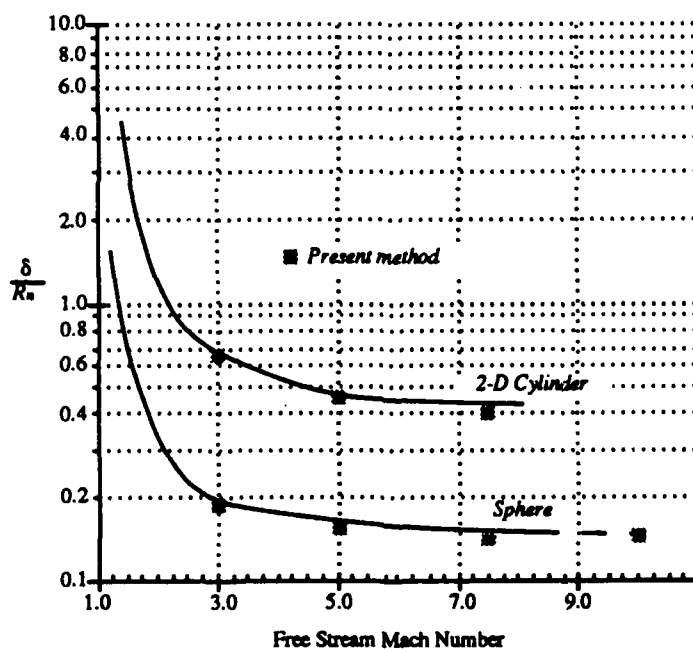


FIGURE 6.1
Comparison of shock Stand-off with Reference 22.

These data appear to deviate slightly from the reference curves at high Mach numbers. This discrepancy arises as a direct result of the half excited vibrational state in the present modeling. The normal shock relations predict a density jump across the shock of

$$\frac{\rho_{sh}}{\rho_{\infty}} = \frac{(\gamma + 1)M_{\infty}^2}{(\gamma - 1)M_{\infty}^2 + 2} \quad (6.1)$$

This ratio asymptotically approaches 6 at large Mach number for perfect air with $\gamma = 1.4$. Since the flow behind the shock is subsonic in the stagnation region, the density ratio will not increase much as the flow comes to rest at the stagnation point, and density throughout the region remains relatively constant. For the present gas model with its half-excited vibrational state, kinetic theory predicts a frozen ratio of specific heats of $4/3$ in the absence of dissociation, which leads to a limiting density ratio of 7. With approximately the same mass flux entering a shock layer, the shock in $4/3$ test cases should be roughly 16% closer to the body in the limit of infinite freestream Mach number. At finite Mach numbers, however, Equation (6.1) predicts slightly less pronounced effects due to γ . Close examination of the figure reveals that at higher Mach numbers, the calculated stand-off distance approaches this proper infinite Mach number limit. For example, at Mach 10, the axisymmetric code predicts a shock location 13% closer to the body than the extrapolated $\gamma = 1.4$ result.

A second classical result predicts the shape and position of the sonic line within the shock layer (13). Figure 6.2 displays the sonic lines for 2-D and axisymmetric calculations. Both pictures depict Mach 5 flow of the same $\gamma = 4/3$ perfect gas.

The sonic line in the 2-D flow shown on the left clearly demonstrates the high curvature associated with sonic line behavior above Mach 2 in 2-D supersonic blunt body flows, and displays the expected acute angle with the body's surface. In the axisymmetric case, the sonic line takes on the steeply raked profile characteristic of 3-D blunt body flows. The third dimension provides an additional direction for the flow to expand, and this, combined with the thinner shock layer, tends to flatten the profile. As is typical of freestream Mach numbers greater than 3, the angle between the body and sonic line is obtuse.

While primarily qualitative evidence, the behavior of the sonic line does demonstrate the Lax-Wendroff scheme's ability to model the physics between the shock and body - even in the stagnation region. The predicted shock stand-off distances lend credence to both the shock fitting implementation and the schemes mass conservation properties.

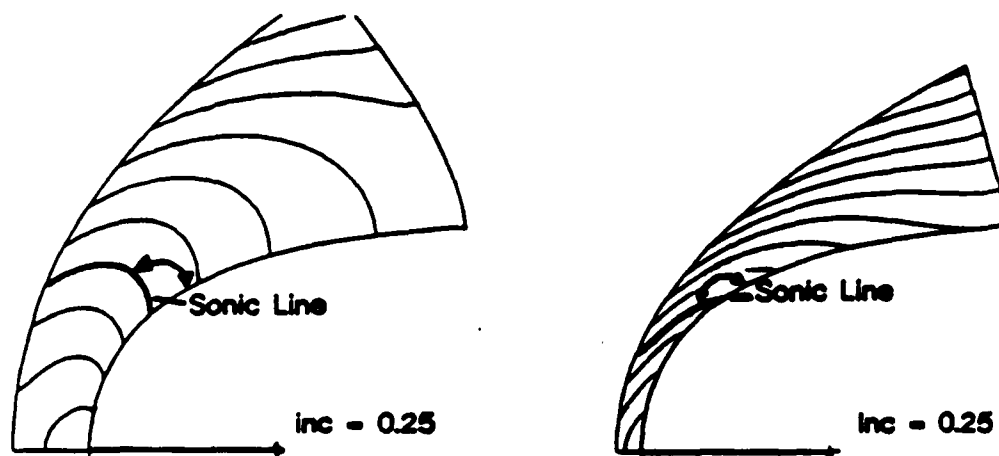


FIGURE 6.2 Two-Dimensional
Computed Mach contours of Mach 5 frozen flow over 2-D and axisymmetric circularly blunted
bodies showing location of the sonic line.

Dissociating Nitrogen

While effective from the standpoint of understanding and completeness, these comparisons tend to be primarily qualitative. Essentially, the above results demonstrate that the shock fit, Lax-Wendroff technique may be applied to supersonic flows, but do not rigorously verify the technique's accuracy, nor do such perfect gas computations demonstrate anything about the real gas model. Therefore, we now compare the current method with both experimental and computational results published by M. N. Macrossan (25).

The case provides a very stringent test of the scheme's ability to model high temperature flows. Table 6.1 details the freestream conditions for both the experiment and computation. In both situations, hot nitrogen flows at approximately Mach 5 past a 15° blunted wedge. The computational conditions were chosen to match momentum flux through the shock and

stagnation enthalpy with those for the experiment. Notice that test conditions are "nominal" and Macrossan estimates a possible 2-7% measurement uncertainty (25).

Several attributes make this an excellent test case. First, the flow over much of the blunt wedge is in a state of *small departure from equilibrium*. The chemical length scale behind the shock is much smaller than the physical dimensions of the body. Using properties behind a frozen normal shock for the freestream conditions, the chemical relaxation length is slightly over $0.003 R_n$. In terms of the Damköhler number defined at the end of the first chapter, Ψ is greater than 36,000. Clearly, we expect very rapid chemical relaxation near the shock. Moreover, the large dissociation energy of nitrogen will strongly couple these chemical effects to other flow parameters through the shock layer. This very strong coupling, combined with the very rapid dissociation provides a severe test of the gas model since over 40% of the stagnation enthalpy is absorbed by dissociation within the first 5% of the shock layer.

TABLE 6.1
Conditions for comparison to dissociating nitrogen test case (from Reference 25).

	Real shock tunnel nominal conditions	Computation with equilibrium freestream
u_∞ (m/s)	6.36×10^3	6.31×10^3
ρ_∞ (kg/m ³)	4.41×10^{-2}	4.45×10^{-2}
T_∞ (K)	4415	5570
α_∞ (dimensionless)	0.094 (frozen)	0.064
M_∞	4.55	4.09
R_n (mm)	5.0	4.91

In addition to the stiffness arising from the disparate time scales involved, this case demonstrates the behavior of the gas model in flows with small regions where temperatures exceed 9,000 K. Normal shock calculations predict temperature ratios of about 4 across the shock. Since the freestream temperature is approximately 5,000 K, the temperature immediately behind the shock is in excess of that allowed with the present model. However, the rapid chemical relaxation in fact quickly absorbs much of this energy and drops the

temperature radically. Most of the flow remains within the range of applicability of the half-excited assumption.

Finally, capturing the relaxation near the bow shock required three levels of embedding and placed interface cells in the stagnation region. This demonstrates the ability of the adaptation to resolve flow features, while preserving conservation across interfaces. Since the shock layer may be thought of as a control volume, any error in conservation will create an error in stand-off distance.

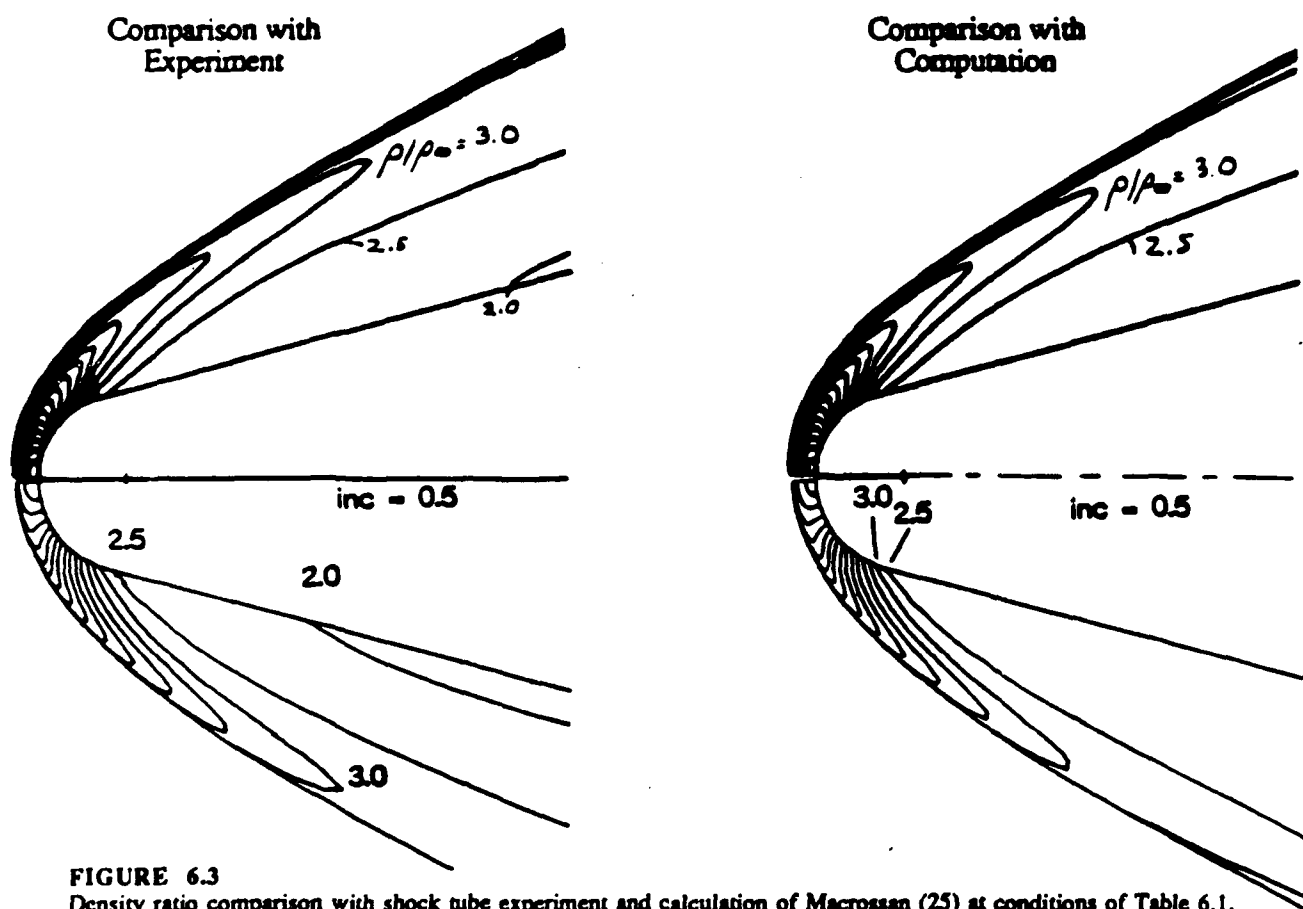


FIGURE 6.3
Density ratio comparison with shock tube experiment and calculation of Macrossan (25) at conditions of Table 6.1.
Current method shown in lower half.

Figure 6.3 compares density contours computed with the present model with those from both experiment and computations performed by Macrossan. Both agree quite closely. The figure on the left contains experimental results above and results from the adaptive computation at nominal shock tunnel conditions below. The comparison on the right displays Macrossan's

solution for the "equivalent equilibrium freestream" above a result from the current method. In Table 6.1 it is interesting to note that reference (25) intended these results to demonstrate that the "equivalent" conditions gave identical results as the experiment, and considered the flowfield at the right virtually identical to that at the left.

While the comparison with the calculation is in rather good agreement, the comparison with experiment differs slightly. The density in the flow varies from roughly 10 to 2 and the present solution shifts the 2.5 and 3.0 contours by approximately $0.25\rho_\infty$. This points to a discrepancy of approximately 2.5%. However, it's worth remembering that the freestream conditions held an uncertainty of approximately 5%, and therefore the comparison is within experimental error.

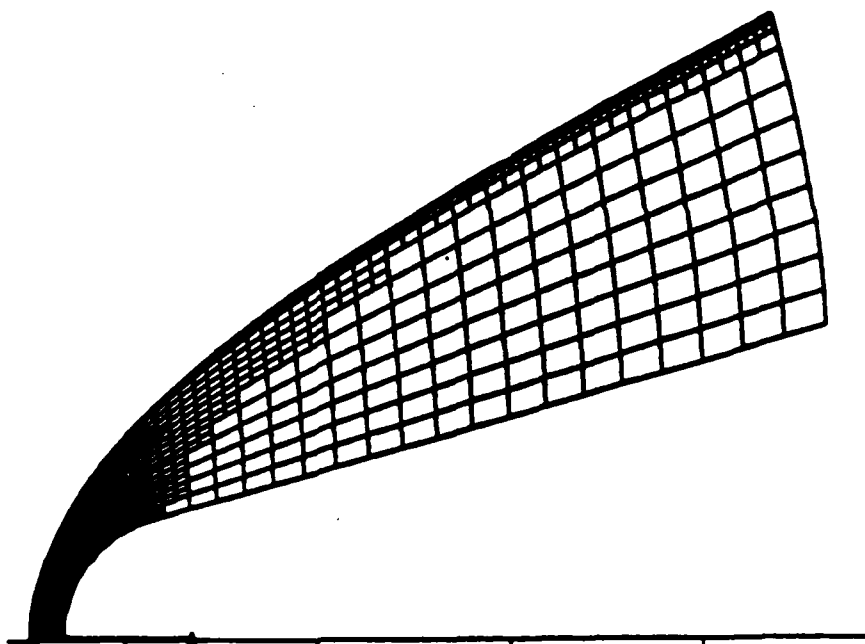


FIGURE 6.4
Adaptive computational grid with 1640 nodes for dissociating nitrogen flow over a circularly blunted 15° wedge at "equivalent" conditions (Table 6.1).

As evidence of the adaptive scheme's ability to detect and resolve flow features, consider Figure 6.4. Here, the final adapted grid for the "equivalent" conditions (Table 6.1) case clearly shows the relaxation zone and expansion fan in the flowfield. With three levels of adaptive refinement, the final grid contains 1640 nodes or slightly more than half the 3000 nodes used by

the DSMC calculation of the reference. The RMS momentum residual was converged two orders of magnitude between adaptations. The adaptation threshold, T_{adapt} was set at 0.35 based upon examination of the first adaptation map and held at this level for the remaining two adaptations.

The source did not estimate the Reynolds number or other viscous parameters in the hot nitrogen test gas. A rough estimate is that Reynolds number is on the order of 10^5 . The interferograms presented in Reference 25 seem to confirm such a high value since the boundary layer remains quite thin.

Reaction Coupling and Multiple Reaction Paths

We now focus on the behavior of the mixture model and thermodynamics as presented in Chapter 2. Comparison of the current gas model is made with two other models described by Candler (5) and an experiment of a sphere fired in air at 5280m/s performed by Lobb (24). Candler's gas models include both a single- and six-temperature models. The latter includes translational temperature, four vibrational temperatures (N_2 , O_2 , NO , NO^+), and an electron temperature. The reference has demonstrated that the six-temperature model predicts the sphere's stand-off distance and shock shape to within experimental accuracy, and therefore comparison is made directly to the six-temperature model.

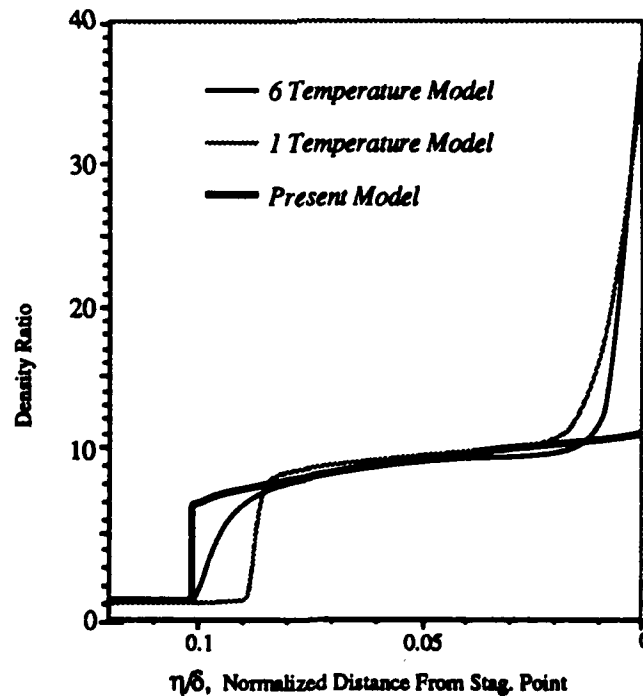
To begin, examine the stand-off distance implied by the present and Ref. 5 density ratio distributions along the stagnation streamline in Figure 6.5. Table 6.2 details assumed freestream conditions.

TABLE 6.2

Conditions for spherical test case of Reference (5) for multiple reaction comparison.

u_{∞} (m/s)	T_{∞} (K)	p_{∞} (Pa)	R_N (mm)	M_{∞}	Re	Ψ
5280	293	664	6.35	15.3	14600	59

In figure 6.5, the gas flows from left to right and the stagnation point is at $\eta/\delta = 0.0$. The present computations were inviscid and, as expected, the shock stand-off distance differs by about 5% due to the thickness of the boundary layer ($\sim 10\%$) at this low Reynolds number. Note that the shock fitting in the present method results in a discontinuous shock (as would be expected at these conditions). The error in stand-off distance arises directly from the cool thermal boundary layer of the viscous calculations. There, nearly constant pressure and lower temperature force density to increase rapidly, bringing the shock closer to the body. In the inviscid portion of the flowfield, the present model does agree within plotting accuracy for the more elaborate models.

**FIGURE 6.5**

Stagnation streamline profiles of density ratio of current method and computations of Candler (5) at conditions in Table 6.2.

Figures 6.6a and 6.6b show further details along the stagnation streamline. The temperature profiles display especially interesting behavior. Since both Ref. 5 models use shock capturing, neither resolves the temperature peak across the shock. Those results for the six-temperature model imply that vibration remains unexcited across the translational shock, supporting the hypothesis of a frozen shock, and that significant vibrational nonequilibrium exists throughout much of the shock layer. If frozen, the temperature peak for $\gamma = 1.4$ should be approximately 14,000 K. The present $\gamma = 4/3$ model has a peak temperature of 11,500 K just downstream of the shock. The one-temperature model (5) allows vibration to absorb energy through the captured shock, and results in a 10,000 K peak behind the shock. As chemical reactions proceed, the curves decay. Both single temperature models decay rather quickly as dissociating O_2 soaks up translational energy. The multitemperature model decay is less rapid since its dissociation rate is linked to both vibrational and translational temperature.

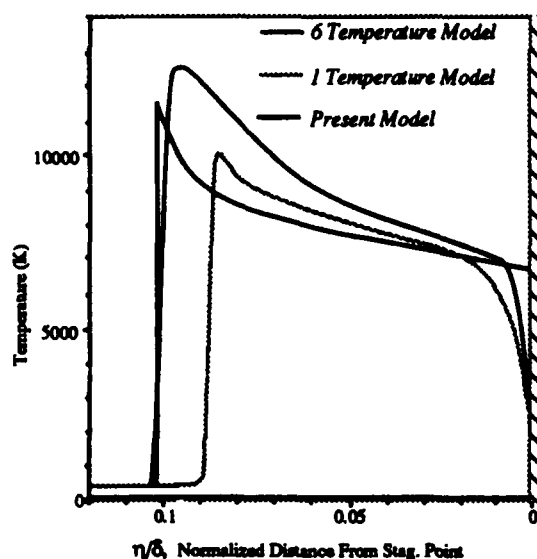


FIGURE 6.6a

Stagnation streamline profiles of temperature and species mass fraction of current method and computations of Candler (5) at conditions in Table 6.2.

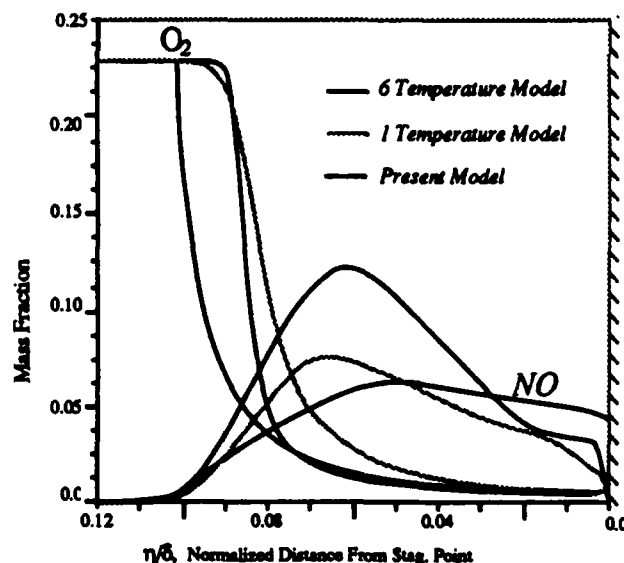


FIGURE 6.6b

This effect also explains the delay (of nearly 0.1δ) experienced before the onset of O_2 dissociation for the six-temperature model (Fig. 6.6b). Although the "shock" stands at $0.1 R_n$, O_2 hesitates until $0.09 R_n$ before dissociation commences. Candler ascribes this behavior to

nonequilibrium within the vibrational modes. Otherwise, the figure demonstrates expected behavior of O_2 and NO throughout the shock layer. Nevertheless, the precise levels of NO disagree amongst the models and the inviscid axisymmetric code used in this comparison naturally tracks none of the behavior in the wall boundary layer.

To summarize, although the current modeling differs in prediction of the absolute species concentration levels, it demonstrates the technique's ability to model reaction coupling, with very reasonable prediction of the gas dynamic variables.

Note that the temperature scale in Figure 6.6a reads in Kelvin. The majority of this shock layer is above, or near, the 9,000 K limit indicated by the derivation in Chapter 2. Despite this, the predicted level of NO molecules remains comparable to those from the other models.

6.2 Effects of Length Scale Behavior

The temperature relaxation seen in Figure 6.6 characterizes nonequilibrium shock layer calculations. The ratio of the chemical relaxation length to a relevant physical reference length, λ/L_{ref} , is a most important parameter in the description of nonequilibrium situations. Such parameters characterize the relative importance of the chemical modeling and determine the distance required for the temperature to decay, or, equivalently, for the density to increase. As a direct result, the shock layer thickness depends strongly upon the degree of nonequilibrium.

General Length and Time Scale Behavior in Inviscid Hypersonic Flows

Virtually throughout the shock layer the flow is out of equilibrium. However, as the velocity approaches zero at the stagnation point the associated convective time scale increases without limit. Since the chemical time scale remains finite, local equilibrium is achieved at the stagnation point in the steady state. At all points in the field the Law of Mass Action

determines a *local equilibrium concentration* , c_e , which "drives" the actual concentration c . Thus, the local concentration must reach the local equilibrium concentration at the stagnation point.

In terms of a simple Landau-Teller type model for the chemical source term \dot{W} ,

$$\dot{W} = \frac{c_e - c}{\tau_{chem}} \quad (6.2)$$

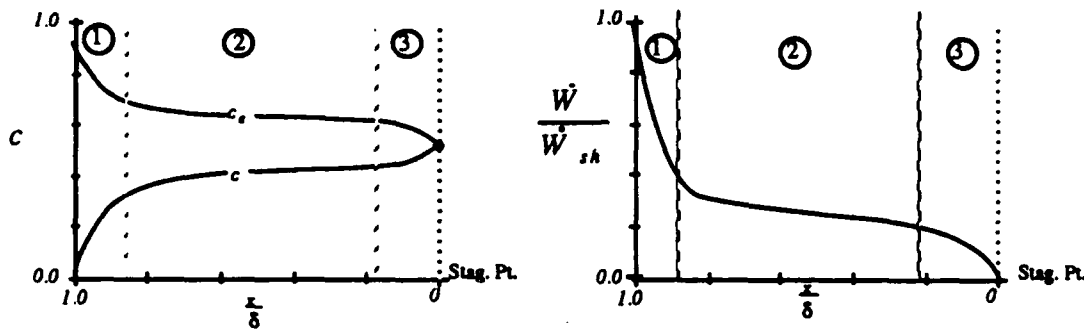


FIGURE 6.7
Schematic of generalized concentration and source term behavior along the stagnation streamline in inviscid flow.

In Equation (6.2) the degree of nonequilibrium governs the magnitude of the source term. Figure 6.7 contains a schematic of the stagnation streamline process in terms of the c and W behavior.

The stagnation point is at the right of both plots ($x/\delta = 0.0$). Since the shock itself is frozen, initially a large difference can exist between c and c_e . In region 1, the flow is far out of equilibrium and τ_{chem} is very small, making \dot{W} large. Thus, the concentration adjusts rapidly as dissociation soaks up internal energy. As this process lowers the temperature, the exponent in the forward reaction term (Eq. 2.33) decreases rapidly, changing \dot{W} in region 2 by several orders of magnitude. As τ_{chem} increases, \dot{W} decreases at approximately the same rate, (Eq. 6.2), and the progress of c toward its goal of c_e is slowed.

The rising density in the flow approaching the stagnation point increases the number of particle collisions, thus elevating the importance of the backward rate term in the source term

expression. The competition between backward and forward terms as they equalize drives \dot{W} to zero, and c approaches c_e .

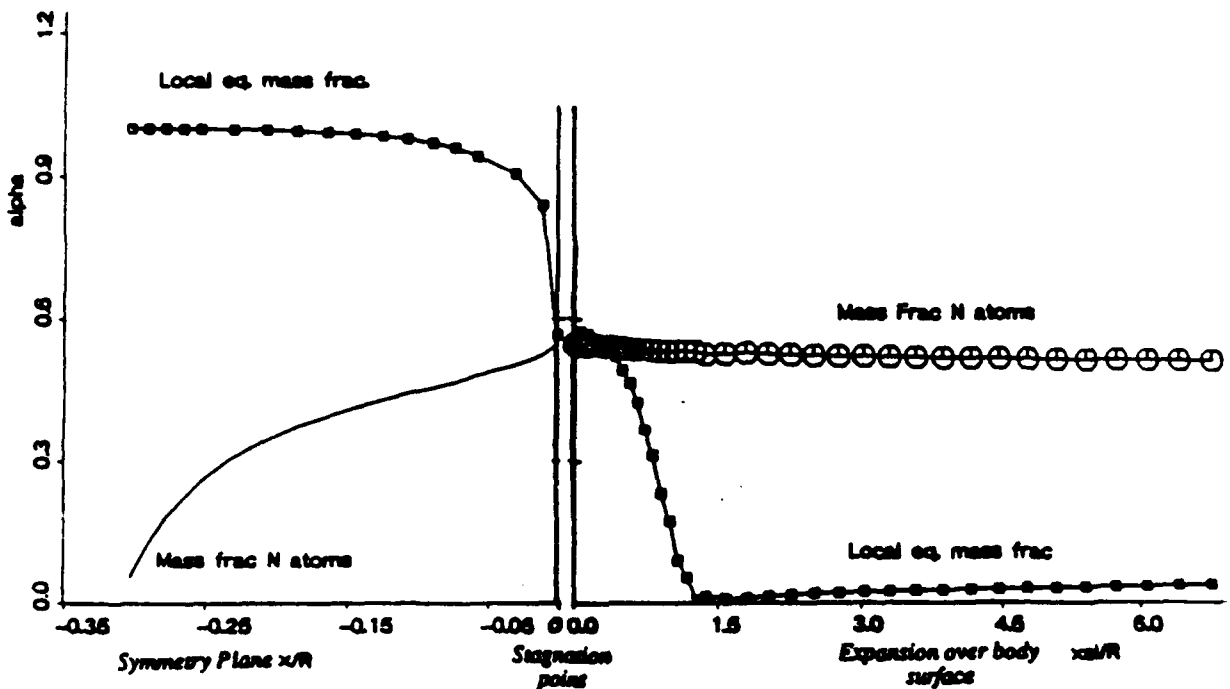


FIGURE 6.8

Stagnation streamline profiles of atom mass fraction and local equilibrium mass fraction for the blunted wedge detailed in Table 6.1 with chemical rate retarded two orders of magnitude.

Figure 6.8 contains a computed result for a blunted wedge. The behavior along the stagnation streamline and its continuation along the body's surface is shown. Conditions for this case match the comparison with computation detailed in Table 6.1, but here the chemical rate was retarded by two orders of magnitude to emphasize nonequilibrium behavior.

The figure illustrates aspects discussed after Fig. 6.7, and in particular, the final approach to equilibrium just before the flow stagnates at $x/R_n = 0$. The species equations do not solve the Law of Mass Action directly, but rather, imply a steady state solution when the source terms vanish at the stagnation point. Since c_e at the stagnation point comes from a direct solution of the Law of Mass Action, it is an independent check of the overall validity of the solution to the governing equations. A slight discrepancy in stagnation point concentration

results from the presence of numerical dissipation and disappears in the limit of either infinite resolution or zero smoothing.

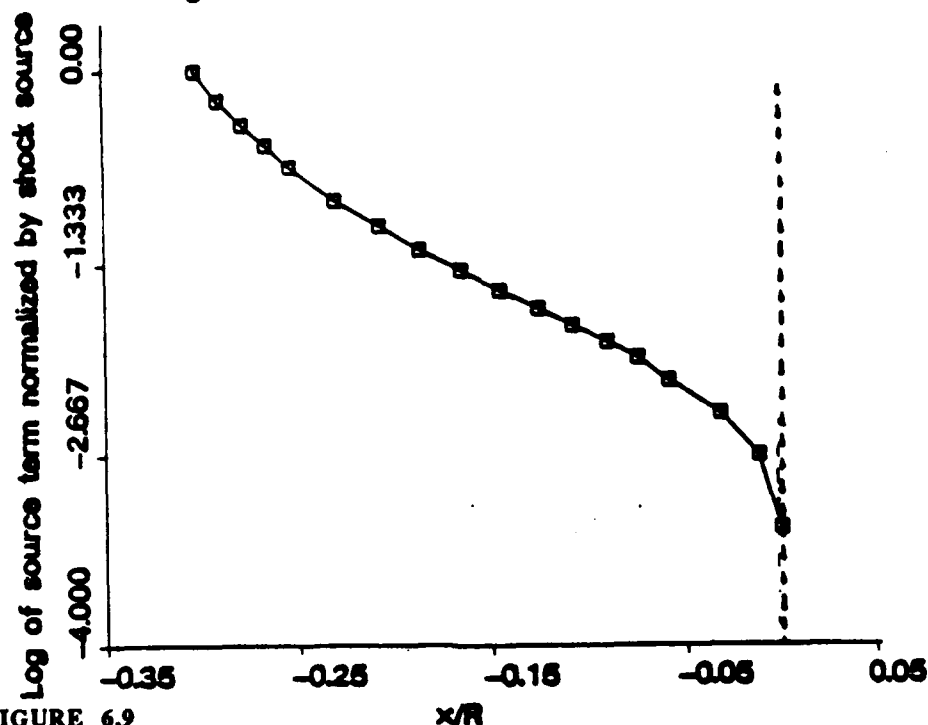


FIGURE 6.9
Symmetry plane profile of the logarithm of the source term normalized by that just behind the frozen shock for the blunted wedge detailed in Table 6.1 with chemical rate retarded two orders of magnitude.

As the flow expands around the nose, the density drops rapidly, reducing the collision rate and effectively freezing out the chemistry. In this region, \dot{W} remains small in part because contributions from both the forward and backward terms remain relatively small.

Consistent with the source term remaining small compared with its post shock value, the chemical time scale remains quite large. The concentration tends toward its local equilibrium value very slowly and would achieve it only far downstream.

Effects of Dissociation Energy

As the symmetry plane flow dissociates downstream of the normal shock, the growth of the dissociation energy, $\alpha\theta_D$, portion of the internal energy implies a relatively decreasing T . The appearance of θ_D within the exponential factor of the source's forward reaction suggests

that for some net reaction rate and associated chemical length scale, the Θ_D role is crucial to the extent of chemical length scale changes throughout the shock layer. For large Θ_D the $\alpha\Theta_D$ contribution to the internal energy expression may dictate a large temperature change for a small change in concentration. The source term will then "feel" this temperature change after being selectively amplified through the exponential in the forward rate term. This mechanism produces radical changes in chemical time scale, Eq. (6.2). Moreover, since only a *small* change in c produced these changes, c may remain far out of equilibrium.

Examine, for example, Figure 6.9 which shows the normalized source term along the symmetry plane on a logarithmic scale for the same case as Figure 6.8. Despite the fact that over the first five points downstream of the shock the concentration change is only about 20% (Fig 6.8), the source term changes by an order of magnitude. That is, τ_{chem} changes by approximately an order of magnitude. This implies a much longer relaxation length, and although the flow remains far from equilibrium, the progress of c toward c_e slows radically.

Of course, there always exists some overall chemical rate or Damköhler number large enough to eliminate such effects, but calculations along the sustained flight corridor suggest that this phenomenon remains important - especially in the case of dissociating nitrogen at low levels of dissociation. Dissociating N_2 absorbs nearly twice the energy of dissociating O_2 , resulting in much stronger coupling between chemical and gas dynamical variables.

As c slows in its progress toward *equilibrium* the temperature changes more slowly, decreasing the rate at which \dot{W} changes and preventing the rapid adjustment of c toward c_e . Finally, as the convective time scale rises in the stagnation region, the finite chemical time scale becomes small by comparison, producing a small "boundary layer" region of rapid adjustment as the concentration equilibrates with c_e . This effect often appears as the "tail" shown in region 3 of the schematic in Figure 6.7, and again displayed in the computation of 6.8. Since it is so

intimately related with length scale behavior, the effect is seen most clearly in flows with large Θ_D parameters.

Effects of Reaction Rate on Length Scale Behavior

The dissociation rate governs the rate of change of the chemical relaxation length throughout the gas, and the non-dimensional reaction rate parameter sets the magnitude of this scale. The previous discussion can be generalized to include a wide class of nonequilibrium problems ranging from nearly frozen to nearly equilibrium.

The sketch in Figure 6.10 shows example distributions of concentration and corresponding local equilibrium concentration for blunt body flows with Damköhler numbers from $\Psi \rightarrow 0$ (frozen) to $\Psi \rightarrow \infty$ (equilibrium). If the flow is very nearly frozen, ㉑, the shock layer experiences little to no dissociation upstream of the stagnation point, where it must eventually adjust to equilibrium. Curves ㉒ and ㉓ exemplify typical profiles found in flows for Ψ of approximately 0.1 and 10 respectively. Numerical calculations at these conditions are shown later. Finally, ㉔ traces the concentration behavior of flows very nearly in equilibrium. Here the infinitesimal chemical length scale permits very rapid convergence of c and c_e and these remain equilibrated until the flow reaches the stagnation point. If sufficiently near to identical equilibrium, these distributions will remain indistinguishable throughout the expansion. Since the stagnation region is normalized by the stand-off distance δ , this sketch does not show how the shock layer thickness increases for more nearly frozen cases. Over the body surface, the exact local equilibrium concentration will depend on the precise values of other flow variables. However, these profiles will all display the same qualitative behavior, and the sketch presents only one curve downstream of the stagnation point.

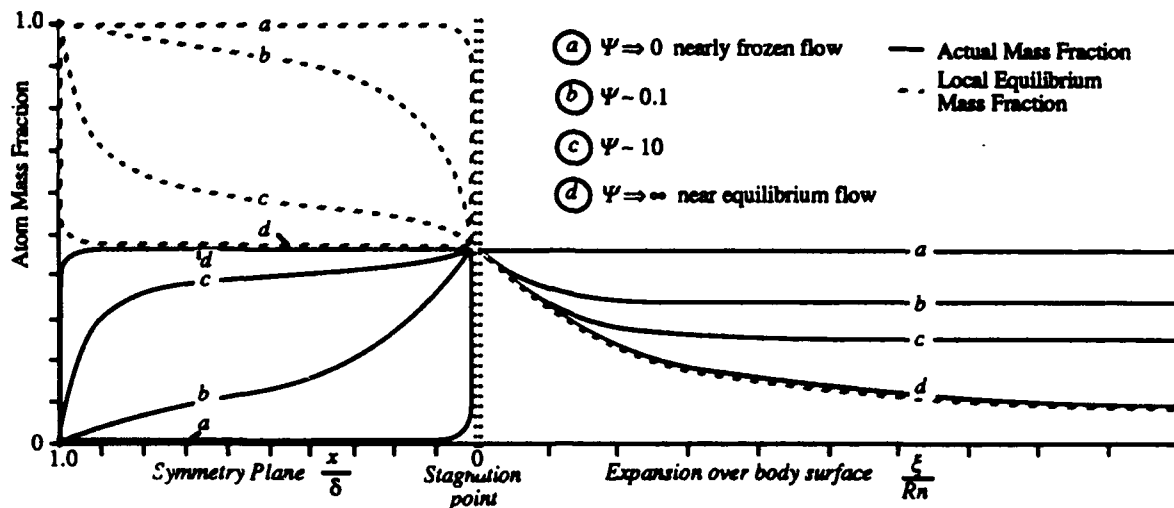


FIGURE 6.10
Mass fraction profiles and local equilibrium mass fractions for reacting flows ranging from near frozen to near equilibrium.

Small Departures from Equilibrium

Figure 6.11 shows the behavior of the wedge example presented earlier (Table 6.1 and Figure 6.3) in comparison to the experiment in Reference 25. Despite the near equilibrium nature of the flow along the symmetry plane, the length scale changes enough by the stagnation point to freeze out over the expansion and wedge surface. Notice that the upward climb of c_e toward c results from an increase in temperature as N atoms slowly recombine and result in a slow drop in c . Capturing the initial transient in a simulation with this severe a discrepancy between chemical and convective length scales requires very high resolution near the shock. The example illustrates the need for extreme caution before awarding identical equilibrium procedures to flows with high dissociation energies. Here we see that even in extremely high Damköhler number flows, the chemical length scale may change enough to freeze out appreciably.

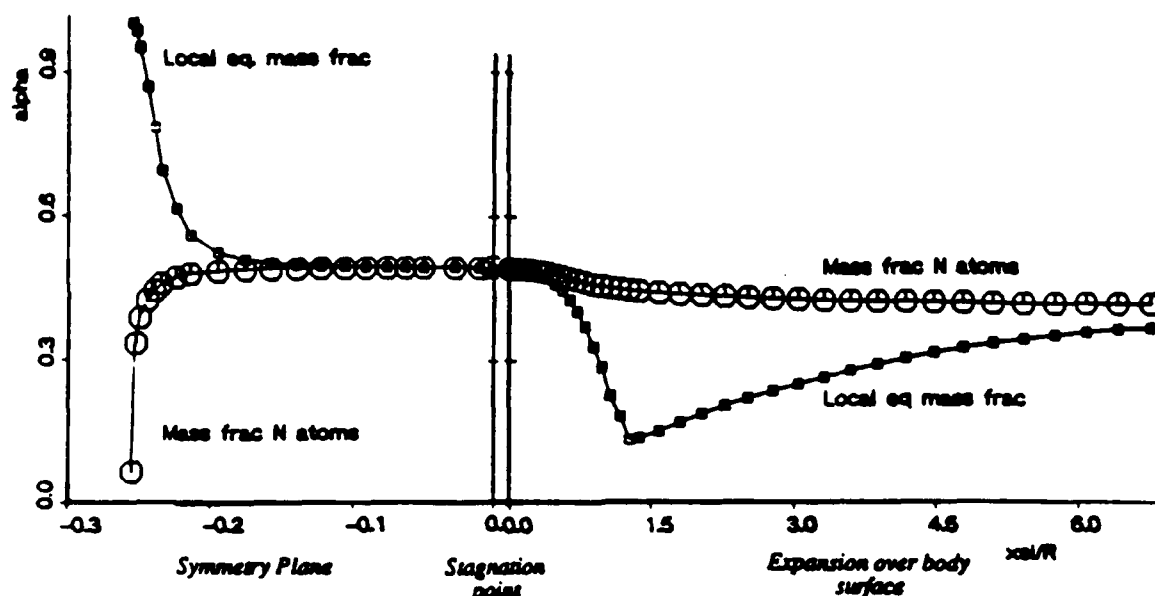


FIGURE 6.11
Stagnation streamline mass fraction and local equilibrium for circularly blunted 15° wedge.
(See also Table 6.1 and Figure 6.3).

Removal of Stagnation Singularity – Viscous Cases

Curve (a) in 6.10 demonstrates near-singular behavior as the frozen concentration through the shock layer rapidly advances toward equilibrium at the stagnation point. Inviscid calculations demonstrate this behavior since the surface streamtube remains quite hot. Realistic viscous computations and real flows, however, maintain a relatively cool thermal boundary layer immediately adjacent to the surface which removes this singularity. As atoms re-combine in the cool layer just removed from the surface, the actual concentration and local equilibrium tend toward zero dissociation. Of course, wall catalytic effects modify this behavior at elevated wall temperatures. The present examples maintain a wall temperature of 1,500 K, cold enough to keep catalytic effects miniscule.

Figure 6.12 details this behavior for two cases which correspond to (c) and (d) in Figure 6.10. In the figure on the left, $\Psi = 10$, while at the right $\Psi = 0.1$. Both cases correspond to Mach 12 flight in the standard atmosphere at 60 km altitude, and the viscous examples use $Re = 6500$, $Pr = 0.72$, and $Sc = 0.5$.

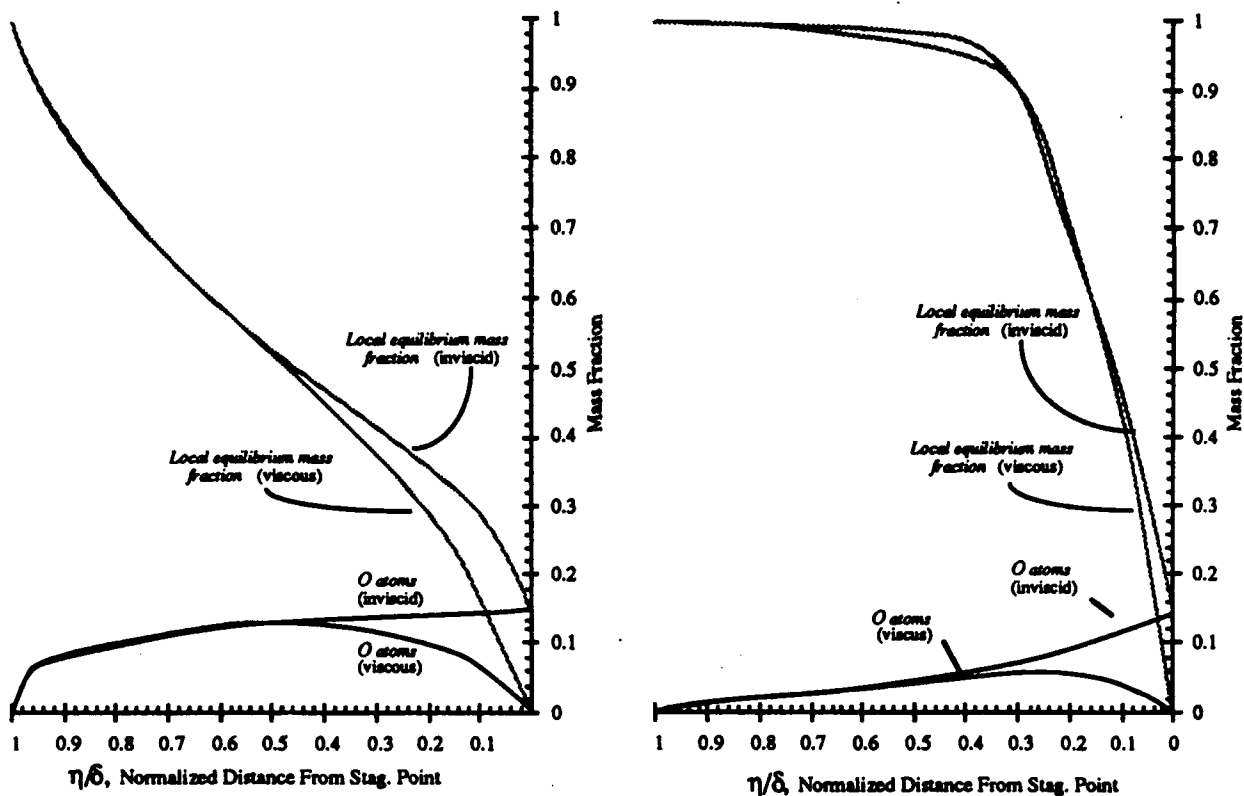


FIGURE 6.12

Mass fraction and local equilibrium mass fraction profiles along the symmetry plane for viscous and inviscid flows at 60 km altitude in STD atmosphere. $\Psi = 10$ (left), $\Psi = 0.1$ (right), $Re = 6500$, $Pr = 0.72$, $Sc = 0.5$.

It is interesting to note that the local equilibrium concentration does not lead the actual concentration to zero in the stagnation region for the viscous examples. Behavior in this region stems from heat conduction and other viscous effects. The viscous terms on the right side of the governing equations (Eq. 1.9) act as additional sources and the simple source term model in Equation (6.1) neglects these complex terms altogether. In fact, non-zero behavior stands as evidence that these terms contribute in this region. Moreover, the fact that the viscous profiles trace the inviscid curves almost precisely through the inviscid portion of the field suggests that mass diffusion, heat transfer, and shear terms remain comparatively small through this portion of the field.

For purposes of comparison, the horizontal scales in Fig. 6.12 were normalized by stand-off distance. This normalization masks the fact that the thick boundary layer in the viscous cases actually displaced the shock by $\sim 7\%$.

6.3 Coupled Reacting Systems

When multiple reactions occur in a gas mixture, the problem of a disparate chemical and convective length scale becomes one of many disparate length scales. The degree of coupling between reactions in such a system depends largely on two factors. First, the relative amounts of energy absorbed or produced by a reaction contribute directly to the overall internal energy of the system and directly affect thermodynamic properties. For example, as one reaction proceeds, it may absorb so much internal energy that some other reactions freeze out. Secondly, the relative scales of the processes affect reaction coupling. If one reaction proceeds much more rapidly than another, the fast reaction may reach its equilibrium concentration long before the other reaction has begun to affect the internal energy of the gas.

Formation of NO within the Shock Layer

In reacting *air* systems, such coupling effects are very clearly demonstrated upon examination of the formation of NO throughout the shock layer. As an example, re-consider the axisymmetric multi-reaction test case presented in Section 6.1 (Table 6.2, Figs. 6.4 and 6.5). Since the shock layer is in vibrational nonequilibrium, the detailed concentration levels of mixture components are incorrect by the standard of more accurate chemical modeling. Nevertheless, the species behavior in this comparison agrees reasonably well.

Figure 6.13 provides profiles of N , O , NO , and O_2 along the stagnation streamline. At conditions just behind the shock the characteristic relaxation length for molecular oxygen dissociation is about $0.01R_n$, while that for nitrogen is approximately $0.5R_n$. This 50-fold disparity is a measure of the degree of coupling between the two dominant reactions.

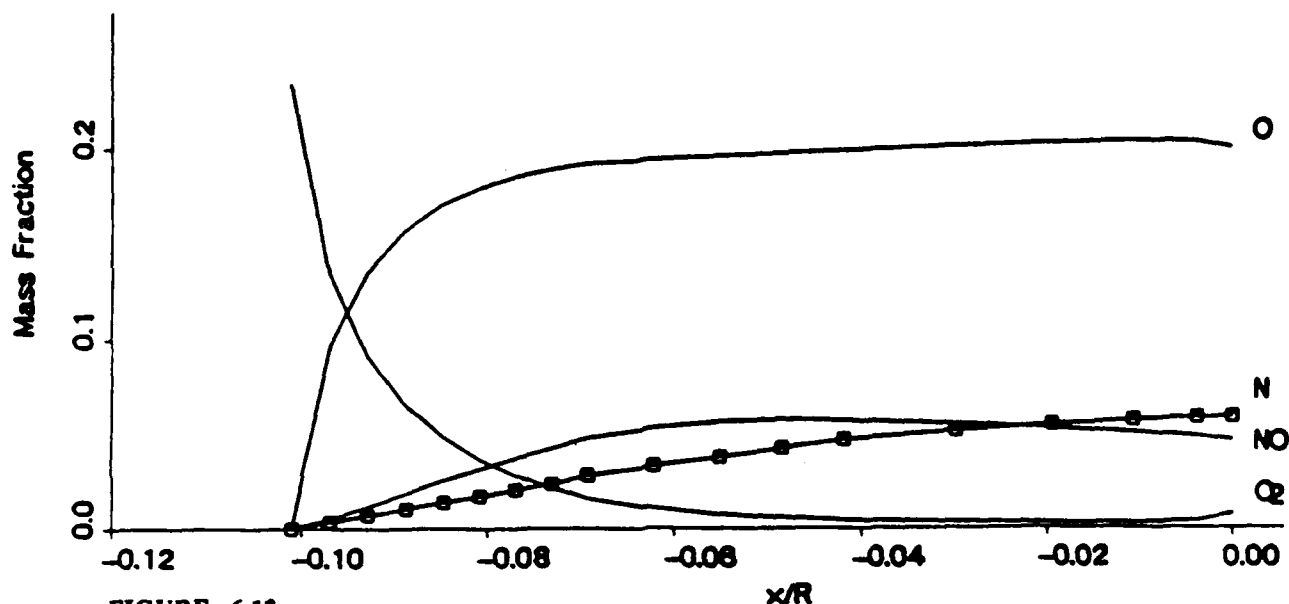


FIGURE 6.13

Symmetry plane profiles of species mass fraction for O_2 , O , NO , and N for the case detailed in Table 6.2 (also see Figs. 6.5 & 6.6).

The earlier plot of equilibrium constants in Figure 1.3 provided an indication of the relative importance of the forward and backward terms in the reaction rate expressions for the five reactions considered here. Of course, in view of the actual chemical nonequilibrium, Fig. 1.3 only provides an approximate guide to the source term's behavior. As the flow in Fig. 6.13 crosses the Mach 15 normal shock, oxygen rapidly dissociates, creating an abundance of free oxygen atoms. These atoms, in turn, activate the exchange reactions which proceed at rates slightly faster than that of O production. However, the competition between these reactions, mentioned in the closing paragraphs of Chapter 1, slows the net production of NO to about $1/10$ th that of O_2 dissociation. At these post-shock temperatures, the first exchange reaction ($O + N_2 \rightleftharpoons N + NO$) proceeds faster than the NO , robbing the exchange reaction ($NO + O \rightleftharpoons N + O_2$). It is this mechanism which is responsible for the initial production of NO behind the shock.

As the temperature decreases to $\sim 8,000$ K inside the shock layer, this competition results in almost exact cancellation of the NO produced and destroyed by the shuffle reactions. Thus the only mechanism left for altering NO concentration is the NO dissociation reaction. At

these temperatures, the forward rate term dominates, breaking up NO molecules at a rate slightly faster than that of nitrogen dissociation. This effect results in the decline of NO concentration approaching the stagnation point.

The remainder of the shock layer is shown in Figure 6.14 for mass fraction contours of NO at the left and isotherms on the right.

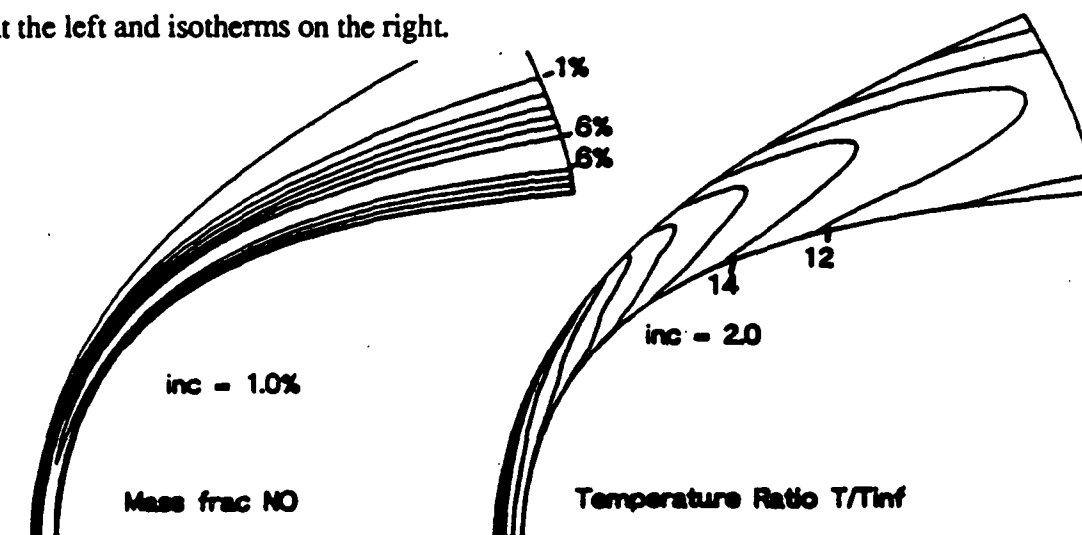


FIGURE 6.14
Contours of NO mass fraction, and temperature ratio computed for the case detailed in Table 6.2 (also see Figs. 6.5 & 6.6).

The temperature field holds two important functions in this discussion. First, for any point in the field, it determines values of the equilibrium constants for the reactions, giving an indication of what local equilibrium condition the species concentrations seek. Secondly, the temperature provides an indication of the overall magnitude of the source terms, and therefore the relevant chemical length scale at any point in the field.

As the flow expands out of the hot stagnation region, the temperature decreases rapidly, slowing the progress of all reactions toward their respective equilibrium conditions. Since nitrogen dissociation has the slowest chemical rate, it is the first to freeze out. Immediately afterward, the nitric oxide dissociation reaction follows suit. With the dissociative reaction turned off, the exchange reactions exclusively determine the concentration of NO in the shock layer, and since their individual rates are so high, these reactions continue to be active, even in

the rapidly freezing flow over the body's shoulder. The imbalance of these reactions continues to drive the concentration of NO upward through most of the expansion fan. This interesting point also was documented by Park (30), and is a direct result of the fact that the first exchange reaction ($O + N_2 \rightleftharpoons N + NO$) still produces more NO than the other consumes. However, as the temperature continues to drop, this situation reverses itself, resulting not only in a decrease in NO , but also O_2 formation (by the same reaction). As oxygen molecules continue to deplete the supply of free oxygen atoms, NO does not have the opportunity to reform. Of course, all of these processes take place over much expanded lengths, since on reaching the shoulder of the body the expanding, cooling flow has changed the chemical length and time scales by several orders of magnitude.

7. Effectiveness of Adaptive Grid Embedding in Hypersonic Flows

The test cases and investigation demonstrate the feasibility of applying the adaptive methodology to hypersonic reacting flows. In evaluating the effectiveness of this procedure, several aspects require consideration. A comparison of such mechanical points as computation time and memory savings afforded by the present technique are of interest, as are the resolution requirements of some of the physical phenomena captured in embedded regions of the flow field and possible improvements in the implementation of the technique itself.

7.1 Enhancement of Computational Efficiency

Since the purpose of the final grid is to resolve all length scales in the domain, the computational savings associated with any flow field depend heavily on the number of length scales involved. Figure 7.1 contains a highly adapted grid resulting from a Mach 16, 2-D simulation at conditions 45 km aloft in the standard atmosphere. The conditions were modified to enhance oxygen dissociation by artificially freezing the nitrogen and nitric oxide dissociation reactions ($\Phi_{N_2} = \Phi_{NO} \equiv 0$). The body size is such that the characteristic length for oxygen dissociation just downstream of the normal shock is only $0.001 R_N$ and virtually all of the molecules dissociate within 1% of the nose radius.

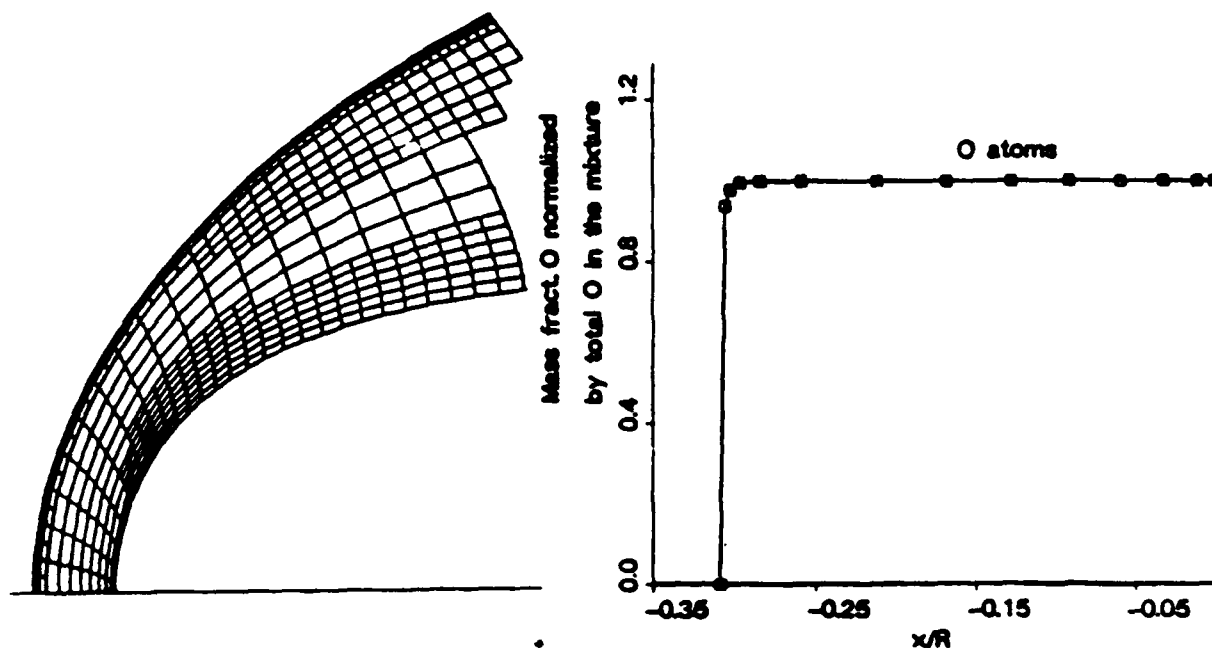


FIGURE 7.1
Adapted grid with four levels of embedding and 1550 nodes for conditions described in text.

Although somewhat contrived, this case provides a good demonstration of the capabilities of the embedded mesh procedure. Moreover, examining the time savings after each level of embedding provides a realistic estimate of the savings for a wide range of chemical rates.

Table 7.1 lists the computation times required for the original coarse grid, final adapted grid, and four globally embedded grids. Notice that at the two highest levels of global mesh refinement, estimated simulation times became sufficiently long that actual tests were precluded.

The final adaptive grid resolved the chemical relaxation with four levels of embedding, and the computation cost proved to be 8.6 times that of the coarse grid baseline case. Resolving the rapid decay on a globally fine mesh would require the same four embeddings, but at a computational cost exceeding 250 times the baseline computation.

TABLE 7.1

Computing time comparisons for adaptive and globally refined meshes for conditions of Figure 7.1.

	Mesh Dimensions	# of nodes	Normalized Computer Time
Original Coarse Grid	10 x 20	200	1.0
Adapted (4-level)	Unstructured	1550	8.6
Entire mesh (1 level embedded)	19 x 39	741	4.7
Entire mesh (2 levels embedded)	37 x 77	2849	17.9
Entire mesh (3 levels embedded)	74 x 153	11322	70.8*
Entire mesh (4 levels embedded)	143 x 305	43617	274.7*

*Estimated due to computing resource limitations

Such comparisons, however, are somewhat optimistic. Obviously, a globally fine grid would provide exceptional detail throughout the field, while the adaptive solution only provides resolution comparable to the scale of the flow features in particular regions. Moreover, given an initial solution on a coarse grid to identify flow features, one could conceivably apply more traditional grid control on a structured mesh providing adequate resolution of the relaxation layer with far fewer than the 44,000 nodes required by the globally refined mesh. The net time for computing a solution with such a procedure, however, is not clear. The final grid would not place nodes as accurately as the adaptive grid, and would certainly contain more nodes. The time required to set up such a grid is difficult to estimate quantitatively. Finally, since such a comparison is so intimately related to the chemical relaxation length, it would be all but meaningless as an indication of typical adaptive savings.

As a better measure of the savings associated with adaptation, consider the examples put forth earlier. Reference 25 computed the blunt wedge case on 3000 nodes to provide the resolution shown in Figure 6.3. However, that figure makes clear that the current adaptive technique provides superior resolution with just over half the computational nodes. The coarse base grid for this case contained 300 nodes and was chosen to provide adequate resolution of frozen flow features. The adaptive solution required 5.7 times the computation effort of the coarse grid solution to converge (5 orders of magnitude in RMS momentum residual).

The axisymmetric sphere results, discussed extensively in Section 6.3 (Figs. 6.12, 6.13), present further evidence of the cost associated with adaptive hypersonic solutions. The final grid for this case contained 1300 nodes, and required three levels of embedding and 5.3 times the computing time of the original 200 node mesh.

These results typify the experience gained over the course of this investigation. Shock fit, reacting hypersonic flow fields over simple geometries usually require 5 - 6 times the computational effort of a coarse base grid solution. In this context, a "coarse grid" is one which clearly shows frozen flow features, but whose resolution is only about half of that required for engineering computations. The coarse base grids referred to in the preceding two paragraphs exemplify these qualities. As the example in Figure 7.1 suggests, flows with larger disparity between chemical and body length scales typically require more computational time, while those more nearly frozen require less. Remember that frozen calculations to engineering precision take about 4 times more effort to compute than the coarse base grid referred to by this comparison (see the "entire mesh [1 level embedded]" entry in Table 7.1). Thus, the time required for an adaptive blunt body reacting flow field is approximately 1.5 times that needed for a frozen solution (using globally refined meshes) of comparable accuracy.

This is an extremely important point, with respect to the effectiveness of the adaptive method. The example shown in Figure 7.2 makes this point even clearer. At the left, the figure shows temperature ratio contours for inviscid Mach 12 frozen flow over an axisymmetric body. The grid required 800 nodes to adequately resolve the frozen, inviscid features, and since frozen, contains only one length scale.

The right of Figure 7.2 shows an adapted case computed in uncoupled (*NO* absent) reacting air at the same Mach number. At 30 km altitude in the standard atmosphere, a nose radius of 0.0318 m produces a characteristic chemical relaxation length of approximately $0.01 R_n$ behind the normal shock. This second length scale greatly increases the resolution

requirements of the numerical procedure. Nevertheless, two levels of adaptive embedding produced results with resolution comparable to that of the frozen case. The final adapted grid contains 1341 nodes and resolves both the chemical and body length scales. Here the adaptive, nonequilibrium solution required a 1.6 times greater computation time than a frozen simulation over the same geometry - despite the multiple length scales in the real gas case.

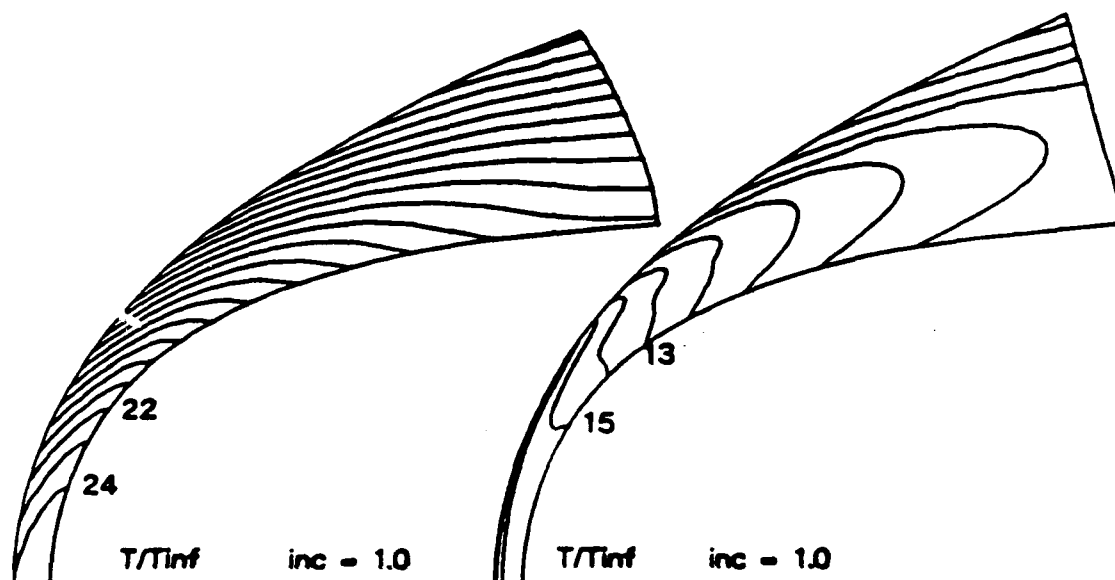


FIGURE 7.2
Contours of temperature ratio for inviscid Mach 12 flow for frozen flow (left), and reacting flow (right).

7.2 Adaptive Resolution of Physical Phenomena

Most algorithms capture shocks in the interior of a computational domain. This process usually results in a smearing out of the physical disturbances over several nodes. Consider, for example, the shock captured solutions of Reference 5 presented in the first section of Chapter 6 (Figs. 6.5, 6.6). There, shock capturing has rounded off the density and temperature jumps across the bow shock. Obviously, an increase in grid resolution near the discontinuity would result in sharper shock jumps, but without *a priori* knowledge of shock positions, this would be expected to be an expensive process.

Shock Triggered Nonequilibrium

Imagine a flow field with a captured shock in a hypersonic flow. Since the calculation may need to be performed at several angles of attack, and since chemical effects will alter shock shape, exact shock positions may not be found prior to computations. However, at hypersonic stagnation enthalpies, any shocks may trigger chemical reactions. Since these reactions determine the downstream gas composition, the relaxation layer requires adequate resolution.

Now, re-examine the shock captured density and temperature profiles in Figures 6.5 and 6.6a. The relaxation zone is an order of magnitude wider than the shock smearing, but for arbitrary shock conditions, this will not always be the case. Consider a scramjet engine inlet, in which each captured, reflected shock will increase the static temperature, decreasing the relaxation length until the relaxation zone may reside entirely within the captured shock. Such a situation would obviously be detrimental to accurate predictions of downstream concentrations and flow properties. References 33 and 34 contain an examination of adaptive solutions through such geometries and demonstrate the adaptive scheme's ability to separate the chemical relaxation from the translational shock.

A second example of such shock-induced nonequilibrium effects occurs in trans-atmospheric or re-entry flight. In this regime, the translational temperature behind the bow shock will be high enough to incite ionization before dissociation and vibration are able to decrease this extreme temperature. Accurate prediction of the electron density in the gas cap therefore depends wholly upon the temperature spike resolved after the translational shock but before nonequilibrium thermo-chemical processes erode this temperature. Again, the multiple length scales of these processes ideally suit such problems to adaptive computations.

7.3 Recommendations for Improving the Adaptive Technique

The examples and test cases in Chapter 6 demonstrate the adaptive scheme's ability to locate and resolve flow features. In the current implementation, the codes' suggested adaptation patterns almost always enclose the detected feature, placing cell interfaces in relatively benign portions of the flow outside the critical area. This section suggests enhancements to the basic adaptation methodology based on experience with the existing codes.

Directional Embedding

Figure 7.3 displays two examples of *directional embedding*. Even in complex hypersonic flow fields, flow features often align with the body and coarse grid orientation. Directional embedding takes advantage of this alignment to increase solution resolution while still avoiding the creation of unnecessary cells and nodes. For example, upon examination of the adapted grids presented in earlier chapters, it becomes clear that many of the features discussed are largely one dimensional. Both the chemical relaxation zone and boundary layer remain primarily grid aligned and would benefit from such directional adaptation. Kallinderis (17) investigated this subject in some detail and claims a reduction in computational effort of approximately two (over an adaptive solution without directional embedding) as a result of the fewer cells and nodes created with this method of cell division.

Incorporation of directional embedding into the current algorithm requires relatively few changes. The feature detection algorithm would then store differences in both directions for each cell. Then the algorithm for cell creation and pointer updating must reflect the unidirectional nature of the embedding.

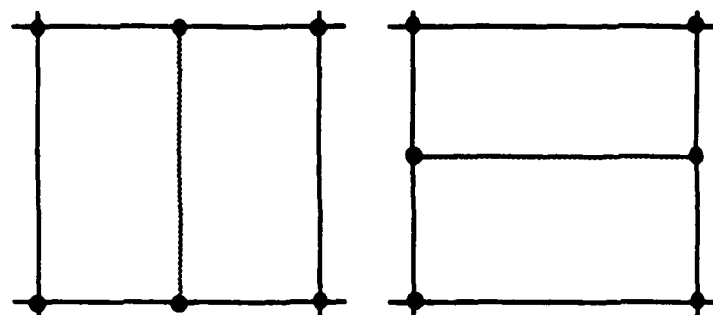


FIGURE 7.3
Cell subdivisions for directional embedding.

Adaption Parameters

Figure 7.4 shows a typical adapted grid for a 2-D reacting viscous calculation ($Re \equiv 6500$). This grid shows embedded regions primarily near the shock and body, capturing both the relaxation layer and boundary layer respectively.

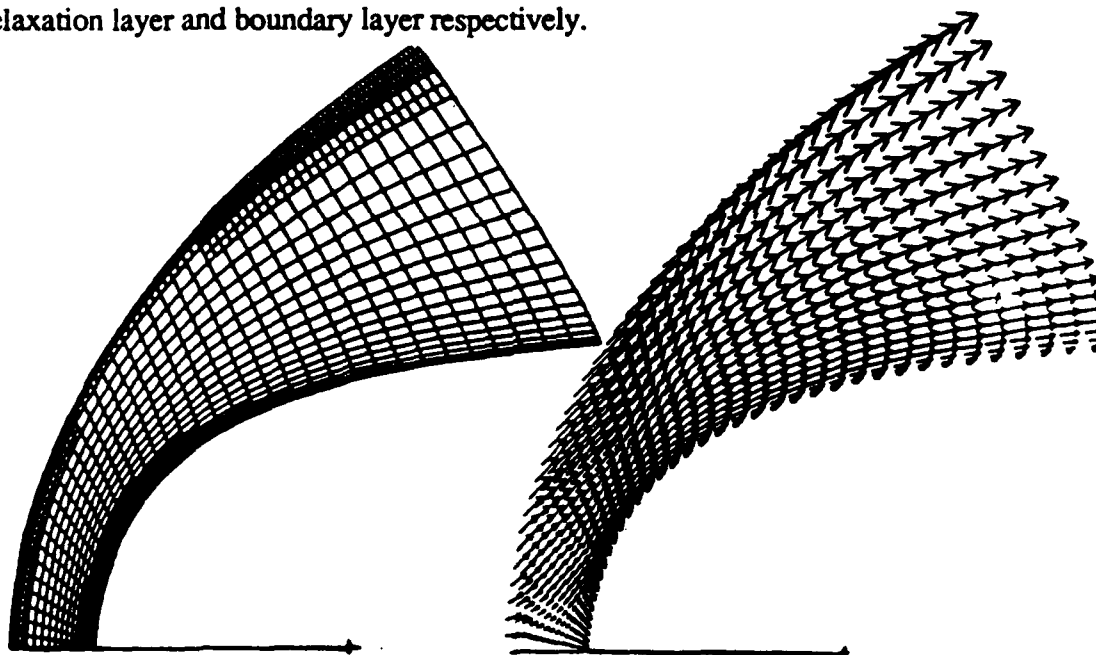


FIGURE 7.4
Adapted grid for a 2-D reacting viscous calculation and total velocity vectors for same calculation.

The current use of density and concentration differences as adaptive parameters stems from expectations of inviscid flow field features. In viscous hypersonic problems however, the thermal gradients near the wall give rise to density gradients via the equation of state. Thus, density differences retain their utility in detecting such boundary layer behavior. However it is the *thermal* boundary layer that these differences indicate (see velocity field in

Fig. 7.4), and clearly, density differences are not appropriate for general shear layers. Reference 17 has made use of both velocity gradients or shear stresses as logical adaptive parameters to identify such a feature.

Summary and Conclusions

The application of adaptive grid embedding to hypersonic flows was motivated by the scales associated with nonequilibrium, high temperature gases that must be modeled for such fields. The adaptive technique permitted numerical simulation of nonequilibrium chemically reacting flows with only 1.5 to 2 times the computational effort of comparably resolved frozen flows. Example calculations were completed for two dimensional, inviscid, flows and extensions to both axisymmetric and viscous flow. In all cases the algorithms provided a means of computing and analyzing complex, reacting, hypervelocity flows over simple geometries such as blunted wedges and cones.

The primary contributions of this work relate to both the development of the numerical algorithm and some details of physical phenomena that adaptive gridding makes clearer.

Numerics and Algorithm Development

This work extended the explicit Lax-Wendroff technique developed by Ni (29) to hypersonic calculations on an unstructured grid. The axisymmetric computational results are believed to demonstrate the first extension of Ni's two-dimensional algorithm to circular cylindrical coordinates.

In addition to enhancements of the integration scheme, the nonequilibrium shock-fit domain necessitated several major modifications of the original adaptive method (6). For example, shock fitting required re-mapping of the unstructured computational grid at each time

step. The simple, effective technique presented in Section 5.3 accomplishes this task on unstructured domains with any number of embedded levels while preserving conservation across mesh interfaces. A lesser contribution to the adaptive methodology was the introduction of a feature detection algorithm capable of triggering mesh refinement dependent upon an arbitrary number of nonequilibrium and flow variables.

Gas Dynamics

A mixture gas model was developed based on the assumption of a half-excited vibrational state for diatomic molecules. This model included N_2 , O_2 , NO , N , and O , and its development required the identification of a *characteristic density for dissociation* of NO molecules. Section 2.2 detailed the formulation of this parameter. Figure 2.2 supports the hypothesis of $\rho_{DNO} = \text{const.}$ required by the dissociative reaction model.

Both the two-dimensional and axisymmetric flow solvers were validated through perfect gas, dissociating gas and multiple reaction comparisons and an investigation of hypersonic flow over blunted cones and wedges for the spectrum of reactions varying from near frozen to near equilibrium. Examination of chemical and convective time and length scales in the domain, provided insight into the character of inviscid and viscous reacting flows under widely varying conditions of nonequilibrium.

Of special note is the interplay between dissociative and exchange reactions in nonequilibrium, high temperature air and the role of the chemical length scale in reaction coupling. For example, increases in the concentration of NO off the symmetry plane are linked directly to the effects of length scale and reaction coupling. Finally, some viscous investigations demonstrated that these same concepts retained their importance in viscous hypersonic flows. However, in regions dominated by diffusion processes, the local equilibrium concentration must share its "driver" role.

Conclusions

Unstructured, adaptive, embedded gridding has been applied to hypersonic, blunt body, nonequilibrium, CFD problems. The high temperature gas mixture was described by Lighthill's dissociating gas model which was extended to include five species and multiply coupled reaction paths in both viscous and inviscid flows. The Lax-Wendroff numerical algorithm was extended to include shock fitting and adaptation on general, unstructured, moving (adjusting) grids.

Comparisons with experiment and computation provided validation for both the explicit real-gas algorithm and unstructured shock fitting procedure for perfect gas, dissociating gas, and multiple reaction cases. The dissociating gas model demonstrated good agreement with shock tunnel experiment and computational results of Reference 19, and reasonable prediction of gas dynamic variables in flows with coupled reactions.

A detailed study of basic nonequilibrium flow phenomena has been completed for freestream Mach numbers from 5 to 15 over blunted cones and wedges. These flows demonstrated degrees of nonequilibrium ranging from nearly frozen to near equilibrium. Adaptation proved useful in examining behavior along the stagnation streamline, especially in cases displaying a small departure from equilibrium. Here, adaptation was shown to be particularly useful in capturing the steep chemical gradients which appear within the shock layer.

Grid adaptation appears to be a cost-effective way of computing high resolution solutions to hypersonic, finite rate, real-gas problems. The computational effort required for an adaptively refined nonequilibrium solution was shown to be only 1.5 to 2 times that required for an equivalently resolved frozen flow solution for the same configuration. This compares favor-

ably with the 40-50 times that may be required for a solution on a globally refined mesh capable of resolving the chemical relaxation.

References

1. Anderson, J. D., Jr.: *Hypersonic and High Temperature Gas Dynamics*, McGraw-Hill Book Co., New York, 1989.
2. Anderson, D. A., J. C. Tannehill, and R. H. Pletcher: *Computational Fluid Mechanics and Heat Transfer*, Hemisphere Publishing Co./McGraw-Hill Book Co., 1984.
3. Blottner, F. G., and D. E. Larson: "Navier-Stokes Code NS3D for Blunt Bodies, Part I: Analysis, Results, and Verification," SAND88-0504/1, March 1988.
4. Candler, G. and R. McCormack: "The Computation of Hypersonic Ionized Flows in Chemically and Thermal Nonequilibrium," AIAA Paper 88-0511, 26th Aerospace Sciences Meeting, Reno, Nevada, January 1988.
5. Candler, G.: "On the Computation of Shock Shapes in Nonequilibrium Hypersonic Flows," AIAA-89-0312, 27th Aerospace Sciences Meeting, Reno, Nevada, January 1989.
6. Dannenhoffer, J. F. III, and J. R. Baron: "Adaptation Procedures for Steady State Solution of Hyperbolic Equations," AIAA Paper 84-0005, Jan. 1984.
7. Dannenhoffer, J. F. III: "Grid Adaptation for Complex Two-Dimensional Transonic Flows," PhD thesis, Massachusetts Institute of Technology, August 1987.
8. Dunn, M. G. and J. A. Lordi: "Facility Requirements for Hypersonic Propulsion System Testing," AIAA Paper 89-0184, 27th Aerospace Society Meeting, January 1989.
9. Eiseman, P.R.: "Adaptive Grid Generation," *Computer Methods in Applied Mechanics and Engineering*, 64:321-376, 1987.
10. Fay, J. A., and F. R. Riddell: "Theory of Stagnation Point Heat Transfer in Dissociated Air," *J. Aerospace Sciences*, Vol. 25, No. 2, pp. 73-85, 1958.
11. Freeman, N. C.: "Nonequilibrium Flow of an Ideal Dissociating Gas," *J. of Fluid Mechanics*, Vol. 4, pp 407-425, 1958.
12. Gnoffo, P. A., and R. S. McCandless: "Three-Dimensional AOTV Flowfield in Chemical Nonequilibrium," AIAA Paper 86-0230, January 1986.
13. Hayes, W. D., and R. F. Probstein: *Hypersonic Flow Theory; Volume I: Inviscid Flows*, Academic Press, 1966.
14. Hilsenrath, J., and M. Klein: "Tables of Thermodynamic Properties of Air in Chemical Equilibrium Including Second Virial Corrections from 1500 to 15,000K," Arnold Engineering Development Center Report No. AEDC-TR-65-68, 1965.

15. Howe, J. T., and J. R. Viegas: "Solution of the Ionized Radiating Shock Layer, Including Reabsorption and Foreign Species Effects and Stagnation Region Heat Transfer," NASA TR R-159, 1963.
16. Kallinderis, Y.G., and J.R. Baron: "Adaptation Methods for a New Navier-Stokes Algorithm," AIAA Journal, Vol 27, No.1, pp 37-43, 1989.
17. Kallinderis, Y.G., and J.R. Baron: "Adaptation Methods for a New Navier-Stokes Algorithm," AIAA Paper 87-1167-CP, June 1987.
18. Kallinderis, Y.G.: "Adaptation Methods for Viscous Flows," PhD. thesis Massachusetts Institute of Technology, 1988.
19. Kewley, D. J., and H. G. Hornung: "Free-Piston Shock-Tube Study of Nitrogen Dissociation," Chem. Phy. Let. 25, p 531.
20. Koppenwallner, G.: "Fundamentals of Hypersonics: Aerodynamics and Heat Transfer," Short Course Notes entitled *Hypersonic Aerothermodynamics*, Von Karman Institute for Fluid Dynamics, Rhose Saint Genese, Belgium, February 1984.
21. Lee, J. H.: "Basic Governing Equations for the Flight Regimes of Aeroassisted Orbital Transfer Vehicles," *Thermal Design of Aeroassisted Orbital Transfer Vehicles*, Ed. H. F. Nelson, Vol. 96, pp3-53, 1985.
22. Liepman, H. W., and A. Roshko: *Elements of Gas Dynamics*, Wiley, New York, 1957.
23. Lighthill, M.L.: "Dynamics of Dissociating Gas, Part I: Equilibrium Flow," Journal of Fluid Mechanics, Vol.2, Pt. 1, 1957.
24. Lobb, R. K.: "Experimental Measurement of Shock Detachment Distance on Spheres Fired in Air at Hypersonic Velocities" in the *High Temperature Aspects of Hypersonic Flow*, Ed. W. C. Nelson, Pergammon Press, MacMillan Co., New York, 1964.
25. Macrossan, M.N.: "Hypervelocity Flow of Dissociating Nitrogen Downstream of a Blunt Nose," submitted to the Journal of Fluid Mechanics, circa April 1989.
26. Macrossan, M. N. and R. J. Stalker: "After-body Flow of a Dissociating Gas Down Stream of a Blunt Nose," AIAA Paper 87-407, Reno, Nevada, 1987.
27. Moretti, G., and M. Abbott: "A Time-Dependent Computational Method for Blunt-Body Flows," AIAA Journal, Vol.4, No.12, 1966.
28. Moss, J. N., and G. A. Bird: "Direct Simulation of Transitional Flow for Hypersonic Reentry Conditions," AIAA Paper No. 84-0223, January 1984.
29. Ni, R. H.: "A Multiple Grid Scheme for Solving the Euler Equations," AIAA Journal 20(11):1565-1571, November 1982.
30. Park C., J. V. Rakich, and H. E. Bailey: "Computation of Nonequilibrium, Supersonic Three-Dimensional Inviscid Flow over Blunt-Nosed Bodies," AIAA Journal, Vol.21, No.6, June 1983.

31. Park, C.: *Non-Equilibrium Hypersonic Flows*, Unpublished Manuscript, NASA Ames, Moffett Field CA, 1987.
32. Park, C.: "On Convergence of Chemically Reacting Flows," AIAA Paper 85-0247, AIAA 23rd Aerospace Sciences Meeting, Reno, Nevada, January 1985.
33. Pervaiz, M. M.: "Spatio-Temporal Adaptive Algorithm for Reacting Flows," PhD thesis, Massachusetts Institute of Technology, May 1988.
34. Shapiro, R. A.: "An Adaptive Finite Element Solution Algorithm for the Euler Equations," PhD thesis, Massachusetts Institute of Technology, May 1988.
35. Thompson, J. F.: "A Survey of Dynamically-Adaptive Grids in the Numerical Solution of Partial Differential Equations," AIAA Paper 84-1606, American Institute of Aeronautics and Astronautics, June 1984.
36. Vincenti, W. G., and C. H. Kruger, Jr.: *Introduction to Physical Gas Dynamics*, Wiley, New York, 1965.

APPENDIX A

Integration Formulae

A.1 Non-Orthogonal Two-Dimensional Coordinates

Cell Change (refer to Fig 3.3)

$$\Delta U_C = \Delta W_C - \frac{\Delta x}{A_C} \left[\begin{aligned} &+ \left(\frac{F_i + F_l}{2} \right) (y_i - y_l) - \left(\frac{G_i + G_l}{2} \right) (x_i - x_l) \\ &+ \left(\frac{F_j + F_i}{2} \right) (y_j - y_i) - \left(\frac{G_j + G_i}{2} \right) (x_j - x_i) \\ &+ \left(\frac{F_k + F_j}{2} \right) (y_k - y_j) - \left(\frac{G_k + G_j}{2} \right) (x_k - x_j) \\ &+ \left(\frac{F_l + F_k}{2} \right) (y_l - y_k) - \left(\frac{G_l + G_k}{2} \right) (x_l - x_k) \end{aligned} \right] \quad (A.1)$$

$$A_C = \frac{1}{2} [(x_k - x_i)(y_j - y_l) - (x_j - x_l)(y_k - y_i)] \quad (A.2)$$

Distribution Formulae (refer to Fig. 3.4)

$$\begin{aligned} \delta U_C)_i &= \frac{1}{4} \left[\Delta U_C - \Delta f_C - \Delta g_C + \frac{\Delta x}{2} \Delta W_C \right] \\ \delta U_C)_j &= \frac{1}{4} \left[\Delta U_C + \Delta f_C - \Delta g_C + \frac{\Delta x}{2} \Delta W_C \right] \\ \delta U_C)_k &= \frac{1}{4} \left[\Delta U_C + \Delta f_C + \Delta g_C + \frac{\Delta x}{2} \Delta W_C \right] \\ \delta U_C)_l &= \frac{1}{4} \left[\Delta U_C - \Delta f_C + \Delta g_C + \frac{\Delta x}{2} \Delta W_C \right] \end{aligned} \quad (A.3)$$

where

$$\begin{aligned}\Delta f_C &= \frac{\Delta t}{A_C} (\Delta F_C \Delta y^l - \Delta G_C \Delta x^l) \\ \Delta g_C &= \frac{\Delta t}{A_C} (\Delta G_C \Delta x^m - \Delta F_C \Delta y^m)\end{aligned}\tag{A.4}$$

and

$$\begin{aligned}\Delta x^l &= \frac{1}{2}(x_l + x_k - x_i + x_j) \\ \Delta y^l &= \frac{1}{2}(y_l + y_k - y_i + y_j) \\ \Delta x^m &= \frac{1}{2}(x_k + x_j - x_l + x_i) \\ \Delta y^m &= \frac{1}{2}(y_k + y_j - y_l + y_i)\end{aligned}\tag{A.5}$$

Time Step

$$\Delta t = (CFL) \min \left(\frac{A_C}{|u \Delta y^l - v \Delta x^l + a \Delta l|}, \frac{A_C}{|u \Delta y^m - v \Delta x^m + a \Delta m|} \right)\tag{A.6}$$

In A.6, $0 \leq CFL \leq 1$.

Additionally,

$$\Delta l = \sqrt{(\Delta x^l)^2 + (\Delta y^l)^2}, \quad \Delta m = \sqrt{(\Delta x^m)^2 + (\Delta y^m)^2}\tag{A.7}$$

A.2 Non-Orthogonal Axisymmetric Coordinates

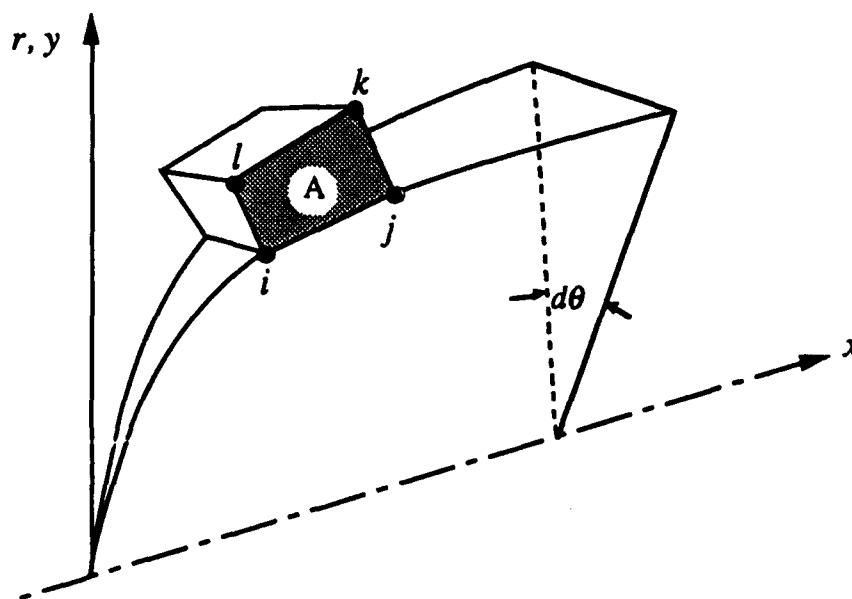


FIGURE A.1
A general cell in circular cylindrical coordinates.

Referring to the above sketch of a general cell in an axisymmetric domain, the inviscid governing equations in circular cylindrical coordinates become:

$$\frac{\partial U}{\partial t} + \frac{\partial F}{\partial x} + \frac{1}{r} \frac{\partial(rG)}{\partial r} = W \quad (\text{A.8})$$

where

$$U = \begin{bmatrix} \rho \\ \rho u \\ \rho v \\ e \\ \rho_i \\ \vdots \\ \rho_s \end{bmatrix}, \quad F = \begin{bmatrix} \rho u \\ \rho u^2 + p \\ \rho uv \\ u(e + p) \\ \rho_i u \\ \vdots \\ \rho_s u \end{bmatrix}, \quad G = \begin{bmatrix} \rho v \\ \rho uv \\ \rho v^2 + p \\ v(e + p) \\ \rho_i v \\ \vdots \\ \rho_s v \end{bmatrix}, \quad W = \begin{bmatrix} 0 \\ 0 \\ \frac{p}{r} \\ 0 \\ \dot{W}_i \\ \vdots \\ \dot{W}_s \end{bmatrix}$$

Cell Change

$$\Delta U_C = \Delta t W_C - \frac{\Delta t}{\bar{r} A_C} \left\{ \begin{aligned} &+ \frac{r_i + r_l}{2} \left[\left(\frac{F_i + F_l}{2} \right) (r_i - r_l) - \left(\frac{G_i + G_l}{2} \right) (x_i - x_l) \right] \\ &+ \frac{r_j + r_i}{2} \left[\left(\frac{F_j + F_i}{2} \right) (r_j - r_i) - \left(\frac{G_j + G_i}{2} \right) (x_j - x_i) \right] \\ &+ \frac{r_k + r_j}{2} \left[\left(\frac{F_k + F_j}{2} \right) (r_k - r_j) - \left(\frac{G_k + G_j}{2} \right) (x_k - x_j) \right] \\ &+ \frac{r_l + r_k}{2} \left[\left(\frac{F_l + F_k}{2} \right) (r_l - r_k) - \left(\frac{G_l + G_k}{2} \right) (x_l - x_k) \right] \end{aligned} \right\} \quad (A.9)$$

where,

$$\bar{r} = \frac{1}{4}(r_i + r_j + r_k + r_l) \quad (A.10)$$

Distribution Formulae

$$\begin{aligned} \delta U_C)_i &= \frac{1}{4} \left[\Delta U_C - \Delta f_{C_i} - \Delta g_{C_i} + \frac{\Delta t}{2} \Delta W_C \right] \\ \delta U_C)_j &= \frac{1}{4} \left[\Delta U_C + \Delta f_{C_j} - \Delta g_{C_j} + \frac{\Delta t}{2} \Delta W_C \right] \\ \delta U_C)_k &= \frac{1}{4} \left[\Delta U_C + \Delta f_{C_k} + \Delta g_{C_k} + \frac{\Delta t}{2} \Delta W_C \right] \\ \delta U_C)_l &= \frac{1}{4} \left[\Delta U_C - \Delta f_{C_l} + \Delta g_{C_l} + \frac{\Delta t}{2} \Delta W_C \right] \end{aligned} \quad (A.11)$$

with

$$\begin{aligned} \Delta f_{C_n} &= \frac{\Delta t}{A_C} \left(\Delta F_C \Delta y^l - \frac{\bar{r}}{r_n} \Delta G_C \Delta x^l \right), \text{ and } n = \{i, j, k, l\} \\ \Delta g_{C_n} &= \frac{\Delta t}{A_C} \left(\frac{\bar{r}}{r_n} \Delta G_C \Delta x^m - \Delta F_C \Delta y^m \right) \end{aligned} \quad (A.12)$$

Along the axis of symmetry, the governing equations become

$$\frac{\partial U}{\partial t} + \frac{\partial F}{\partial x} + 2 \frac{\partial (G)}{\partial r} = W \quad (A.13)$$

The cell change for cells along this axis has no contribution from the face on the axis, and this equation leads to $\Delta g_{C_n} = 0$ when n lies along axis of symmetry. These two changes completely account for the singularity in the coordinate system at $r = 0$.

A.3 Viscous Formulation in Two-Dimensions

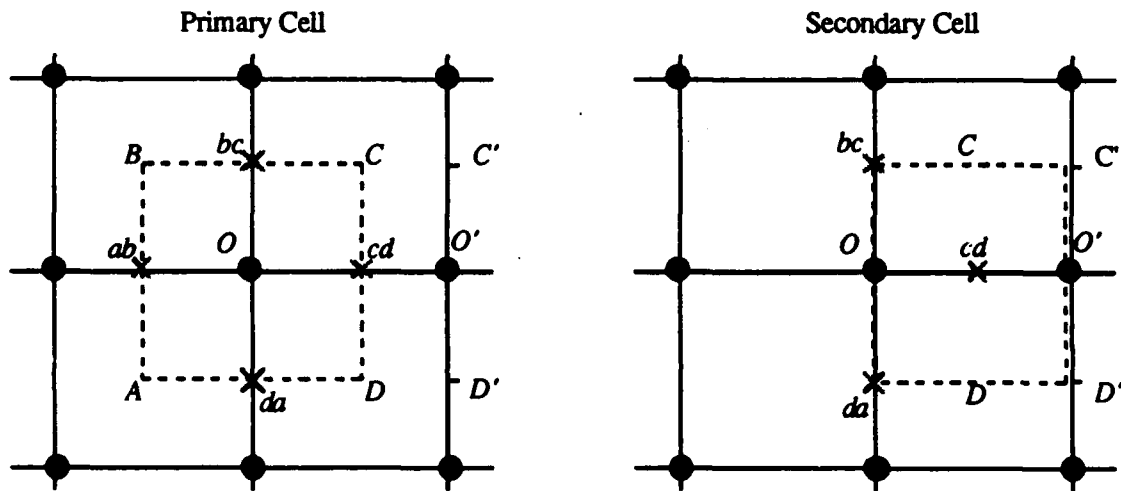


FIGURE A.2
Primary and Secondary cells for viscous integration.

After first distributing the inviscid changes to each node (via Eq.A.3), the algorithm computes nodal changes from the viscous terms R and S in the governing equations (Eq.1.9). The formulation of these changes is naturally more complex, since these dissipative terms rely upon second derivatives. As with the inviscid changes, contributions from all cells surrounding a node complete the difference stencil for these terms. The Lax-Wendroff scheme relies upon the second order changes of the inviscid integration for stability. Fortunately this requirement does not extend to the viscous terms and no Jacobians of R or S need be computed (18). However, this omission reduces the time accuracy of the scheme to first order.

Following the notation in Figure A.2 the viscous change to any node in the computational mesh is

$$\Delta U_{visc} = \frac{\Delta t}{A} \begin{pmatrix} +[+R_D^w \Delta y_B^w + R_A^e \Delta y_A^m] - [+S_D^w \Delta x_B^w + S_A^e \Delta x_A^m] \\ +[+R_C^s \Delta y_C^l + R_D^n \Delta y_B^l] - [+S_C^s \Delta x_C^l + S_D^n \Delta x_B^l] \\ +[-R_B^e \Delta y_B^m - R_C^w \Delta y_C^m] - [-S_B^e \Delta x_B^m - S_C^w \Delta x_C^m] \\ +[-R_A^n \Delta y_A^l - R_B^s \Delta y_B^l] - [-S_A^n \Delta x_A^l - S_B^s \Delta x_B^l] \end{pmatrix} \quad (A.14)$$

In (I.14), the superscripts on R and S refer to cell faces and the area, A, is the area of the primary cell in Figure A.2.

In the integration scheme, however, we sweep through the cells and determine contributions to each node. Thus Equation A.14 needs to be re-expressed in terms of contributions from any cell to its four corner nodes.

Viscous distribution formulae

$$\begin{aligned} (\Delta U_{visc})_{sw} &= \frac{\Delta t}{A} [(+R^s \Delta y^l - R^w \Delta y^m) - (+S^s \Delta x^l - S^w \Delta x^m)] \\ (\Delta U_{visc})_{nw} &= \frac{\Delta t}{A} [(+R^n \Delta y^l + R^w \Delta y^m) - (+S^n \Delta x^l + S^w \Delta x^m)] \\ (\Delta U_{visc})_{ne} &= \frac{\Delta t}{A} [(-R^n \Delta y^l + R^e \Delta y^m) - (-S^n \Delta x^l + S^e \Delta x^m)] \\ (\Delta U_{visc})_{se} &= \frac{\Delta t}{A} [(-R^s \Delta y^l - R^e \Delta y^m) - (-S^s \Delta x^l - S^e \Delta x^m)] \end{aligned} \quad (A.15)$$

The terms in the R and S vectors in this equation contain first derivative terms like $(u_x)_{cd}$ which must be split into contributions from the cells involved.

$$\left(\frac{\partial u}{\partial x} \right)_{cd} = \begin{pmatrix} +\frac{1}{A_C} [U_O(y_C - y_O) + U_C(y_{bc} - y_C) + U_O(y_O - y_{bc})] \\ +\frac{1}{A_D} [U_O(y_O - y_D) + U_O(y_{da} - y_O) + U_D(y_D - y_{da})] \end{pmatrix} \quad (A.16)$$

This formulation stresses the contributions from each cell C and D in the composition of the first derivatives.

Reference 18 contains a thorough explanation of the viscous integration scheme for non-reacting flow in general two dimensional coordinates.

THIS PAGE INTENTIONALLY LEFT BLANK

APPENDIX B

Jacobian Matrices

B.1 Perfect Gas

In a calorically perfect gas with ratio of specific heats γ

$$h_o = \frac{\gamma}{\gamma-1} \frac{P}{\rho} + \frac{1}{2}(u^2 + v^2) \quad (\text{B.1})$$

relates the stagnation enthalpy to the local gas properties.

In this case the derivatives of pressure with respect to elements of the state vector are simple and expressions for ΔF and ΔG are

$$\begin{aligned} \Delta F = \left(\frac{\partial F}{\partial U} \right) \Delta U &= \begin{bmatrix} (\Delta \rho u) \\ u(\Delta \rho u) + u(\rho \Delta u) + \Delta P \\ v(\Delta \rho u) + u(\rho \Delta v) \\ h_o(\Delta \rho u) + u(\rho \Delta h_o) \end{bmatrix} \\ \Delta G = \left(\frac{\partial G}{\partial U} \right) \Delta U &= \begin{bmatrix} (\Delta \rho v) \\ u(\Delta \rho v) + v(\rho \Delta u) \\ v(\Delta \rho v) + v(\rho \Delta v) + \Delta P \\ h_o(\Delta \rho v) + v(\rho \Delta h_o) \end{bmatrix} \end{aligned} \quad (\text{B.2})$$

where

$$\begin{aligned} (\rho \Delta u) &= (\Delta \rho u) - u(\Delta \rho) \\ (\rho \Delta v) &= (\Delta \rho v) - v(\Delta \rho) \end{aligned} \quad (\text{B.3})$$

and

$$(\Delta P) = (\gamma-1) \left\{ (\Delta e) - \frac{1}{2} \begin{bmatrix} +u(\Delta \rho u) + v(\Delta \rho v) \\ +u(\rho \Delta u) + v(\rho \Delta v) \end{bmatrix} \right\} \quad (\text{B.4})$$

$$(\rho \Delta h_o) = (\Delta e) + (\Delta P) - h_o(\Delta \rho)$$

B.2 Nonequilibrium Mixture Gas Model

For the nonequilibrium mixture gas model developed by Chapter 2 the pressure at any point in the field is

$$p = (\gamma_F - 1) \left[U_4 - \Re \bar{\Theta} - \frac{U_2^2 + U_3^2}{2U_1} \right] \quad (\text{B.5})$$

Where U_n represents the n^{th} element of the state vector and γ_F and $\bar{\Theta}$ are defined by

$$\gamma_F \equiv \frac{\left(\frac{dh}{dt} \right)_c}{\left(\frac{de}{dt} \right)_c} = \frac{\frac{5}{2} \left(\frac{c_1}{m_1} + \frac{c_2}{m_2} \right) + 4 \left(\frac{c_3}{m_3} + \frac{c_4}{m_4} + \frac{c_5}{m_5} \right)}{3 \left(\frac{c_1}{2m_1} + \frac{c_2}{2m_2} + \frac{c_3}{m_3} + \frac{c_4}{m_4} + \frac{c_5}{m_5} \right)}$$

$$\text{and } \bar{\Theta} \equiv \begin{bmatrix} + \frac{\Theta_{D1}}{m_4} (U_1 - U_1 c_{frac1} m_1 + U_7 \frac{m_1}{m_3} + U_5) \\ + \frac{\Theta_{D2}}{m_5} (U_1 - U_1 c_{frac2} m_2 + U_7 \frac{m_2}{m_3} + U_6) \\ + \frac{\Theta_{D3}}{m_3} (U_1 - U_7) \end{bmatrix} \quad (\text{B.6})$$

with

$$c_{frac1} \equiv \frac{f_1}{f_1 m_1 + f_2 m_2}$$

$$c_{frac2} \equiv \frac{f_2}{f_1 m_1 + f_2 m_2} \quad (\text{B.7})$$

and for air $f_1 = 0.79$ and $f_2 = 0.21$.

Derivatives of Pressure

$$\frac{\partial P}{\partial U_1} = (\gamma - 1) \left[-\mathfrak{R} \frac{\partial \bar{\Theta}}{\partial U_1} + \frac{u^2 + v^2}{2} \right]$$

$$\frac{\partial P}{\partial U_2} = -u(\gamma - 1)$$

$$\frac{\partial P}{\partial U_3} = -v(\gamma - 1)$$

$$\frac{\partial P}{\partial U_4} = (\gamma - 1)$$

$$\frac{\partial P}{\partial U_5} = - \left[(\gamma - 1) \mathfrak{R} \frac{\Theta_{D_1}}{m_4} + \frac{p}{m_1 \sum_s \frac{c_i}{m_i}} \right]$$

$$\frac{\partial P}{\partial U_6} = - \left[(\gamma - 1) \mathfrak{R} \frac{\Theta_{D_2}}{m_5} + \frac{p}{m_2 \sum_s \frac{c_i}{m_i}} \right]$$

$$\frac{\partial P}{\partial U_6} = (\gamma - 1) \left[\frac{\mathfrak{R}}{m_3} \left(\Theta_{D_3} - \frac{\Theta_{D_2}}{2} - \frac{\Theta_{D_1}}{2} \right) \right]$$

(B.8)

Where

$$\begin{aligned}
 \frac{\partial \bar{\Theta}}{\partial U_1} &= (1 - c_{frac1} m_1) \frac{\Theta_{D1}}{m_4} + (1 - c_{frac2} m_2) \frac{\Theta_{D2}}{m_5} + \frac{\Theta_{D3}}{m_3} \\
 \frac{\partial \bar{\Theta}}{\partial U_5} &= \frac{\Theta_{D1}}{m_4} \\
 \frac{\partial \bar{\Theta}}{\partial U_6} &= \frac{\Theta_{D2}}{m_5} \\
 \frac{\partial \bar{\Theta}}{\partial U_7} &= \frac{1}{2} \left(\frac{\Theta_{D1}}{m_3} + \frac{\Theta_{D2}}{m_3} \right) - \frac{\Theta_{D3}}{m_3}
 \end{aligned} \tag{B.9}$$

Jacobian Matrices

$$\frac{\partial \mathbf{F}}{\partial \mathbf{U}} = \begin{bmatrix} 0 & 1 & 0 & 0 & 0 & 0 & 0 \\ \frac{\partial p}{\partial U_1} - \frac{U_2^2}{U_1^2} & 2 \frac{U_2}{U_1} + \frac{\partial p}{\partial U_2} & \frac{\partial p}{\partial U_3} & \frac{\partial p}{\partial U_4} & \frac{\partial p}{\partial U_5} & \frac{\partial p}{\partial U_6} & \frac{\partial p}{\partial U_7} \\ -\frac{U_2 U_3}{U_1^2} & \frac{U_3}{U_1} & \frac{U_2}{U_1} & 0 & 0 & 0 & 0 \\ U_2 \frac{\partial h_o}{\partial U_1} & U_2 \frac{\partial h_o}{\partial U_2} + h_o & U_2 \frac{\partial h_o}{\partial U_3} & U_2 \frac{\partial h_o}{\partial U_4} & U_2 \frac{\partial h_o}{\partial U_5} & U_2 \frac{\partial h_o}{\partial U_6} & U_2 \frac{\partial h_o}{\partial U_7} \\ -\frac{U_5 U_2}{U_1^2} & \frac{U_5}{U_1} & 0 & 0 & \frac{U_2}{U_1} & 0 & 0 \\ -\frac{U_6 U_2}{U_1^2} & \frac{U_6}{U_1} & 0 & 0 & 0 & \frac{U_2}{U_1} & 0 \\ -\frac{U_7 U_2}{U_1^2} & \frac{U_7}{U_1} & 0 & 0 & 0 & 0 & \frac{U_2}{U_1} \end{bmatrix} \tag{B.10}$$

$$\frac{\partial G}{\partial U} = \begin{bmatrix} 0 & 0 & 1 & 0 & 0 & 0 & 0 \\ -\frac{U_2 U_3}{U_1^2} & \frac{U_3}{U_1} & \frac{U_2}{U_1} & 0 & 0 & 0 & 0 \\ \frac{\partial p}{\partial U_1} - \frac{U_3^2}{U_1^2} & \frac{\partial p}{\partial U_2} & 2\frac{U_3}{U_1} + \frac{\partial p}{\partial U_3} & \frac{\partial p}{\partial U_4} & \frac{\partial p}{\partial U_5} & \frac{\partial p}{\partial U_6} & \frac{\partial p}{\partial U_7} \\ U_3 \frac{\partial h_o}{\partial U_1} & U_3 \frac{\partial h_o}{\partial U_2} & U_3 \frac{\partial h_o}{\partial U_3} + h_o & U_3 \frac{\partial h_o}{\partial U_4} & U_3 \frac{\partial h_o}{\partial U_5} & U_3 \frac{\partial h_o}{\partial U_6} & U_3 \frac{\partial h_o}{\partial U_7} \\ -\frac{U_5 U_3}{U_1^2} & \frac{U_5}{U_1} & 0 & 0 & \frac{U_3}{U_1} & 0 & 0 \\ -\frac{U_6 U_3}{U_1^2} & \frac{U_6}{U_1} & 0 & 0 & 0 & \frac{U_3}{U_1} & 0 \\ -\frac{U_7 U_3}{U_1^2} & \frac{U_7}{U_1} & 0 & 0 & 0 & 0 & \frac{U_3}{U_1} \end{bmatrix}$$

(B.11)

Since W_U is not required for either stability or spacial accuracy this matrix is not computed.

This reduces the scheme's time accuracy to first order (34).